# REPORT DOCUMENTATION PAGE

Form Approved OMB NO. 0704-0188



| 1. REPORT DATE (DD-MM-YYYY) | 2. REPORT TYPE | 3. DATES COVERED (From - To) |
|---|---|---|
| 06-07-2016 | Final Report | 15-Sep-2010 - 14-Mar-2013 |

**4. TITLE AND SUBTITLE**
Final Report: The Effect of Secondary Phases and Birefringence on Visible Light Transmission in Translucent a'-Sialon Ceramics

**5a. CONTRACT NUMBER**
W911NF-10-1-0478

**5b. GRANT NUMBER**

**5c. PROGRAM ELEMENT NUMBER**
9D10AS

**6. AUTHORS**
Gary Messing, Carl Morandi

**5d. PROJECT NUMBER**

**5e. TASK NUMBER**

**5f. WORK UNIT NUMBER**

**7. PERFORMING ORGANIZATION NAMES AND ADDRESSES**
Pennsylvania State University
Office of Sponsored Programs
110 Technology Center Building
University Park, PA 16802 -7000

**8. PERFORMING ORGANIZATION REPORT NUMBER**

**9. SPONSORING/MONITORING AGENCY NAME(S) AND ADDRESS (ES)**
U.S. Army Research Office
P.O. Box 12211
Research Triangle Park, NC 27709-2211

**10. SPONSOR/MONITOR'S ACRONYM(S)**
ARO

**11. SPONSOR/MONITOR'S REPORT NUMBER(S)**
56795-MS.1

**12. DISTRIBUTION AVAILIBILITY STATEMENT**
Approved for Public Release; Distribution Unlimited

**13. SUPPLEMENTARY NOTES**
The views, opinions and/or findings contained in this report are those of the author(s) and should not contrued as an official Department of the Army position, policy or decision, unless so designated by other documentation.

**14. ABSTRACT**
Transparent ?'-SiAlON ceramics have the potential to replace modern transparent ceramic ballistic windows such as AlON, spinel, and sapphire due to their superior hardness and lower density. Residual AlN-polytypoid and amorphous glass were observed as secondary phases in initial studies but through systematic compostion studies we decreased the AlN-polytypoid concentration. UV-visible spectroscopy demonstrated that neither the amorphous glassy grain boundary phase nor AlN-polytypoids are the dominant light scattering sites in ?'-SiAlON ceramics. The effects of birefringent scattering on the light transmission were explored by analyzing the effect of grain size in

**15. SUBJECT TERMS**
Transparent SiAION Armor

| 16. SECURITY CLASSIFICATION OF: | | | 17. LIMITATION OF ABSTRACT | 15. NUMBER OF PAGES | 19a. NAME OF RESPONSIBLE PERSON |
|---|---|---|---|---|---|
| a. REPORT | b. ABSTRACT | c. THIS PAGE | | | Gary Messing |
| UU | UU | UU | UU | | 19b. TELEPHONE NUMBER 814-865-2262 |

## Report Title

Final Report: The Effect of Secondary Phases and Birefringence on Visible Light Transmission in Translucent a'-Sialon Ceramics


## ABSTRACT

Transparent ?'-SiAlON ceramics have the potential to replace modern transparent ceramic ballistic windows such as AlON, spinel, and sapphire due to their superior hardness and lower density. Residual AlN-polytypoid and amorphous glass were observed as secondary phases in initial studies but through systematic compostion studies we decreased the AlN-polytypoid concentration. UV-visible spectroscopy demonstrated that neither the amorphous glassy grain boundary phase nor AlN-polytypoids are the dominant light scattering sites in ?'-SiAlON ceramics.

The effects of birefringent scattering on the light transmission were explored by analyzing the effect of grain size in ?'-SiAlON ceramics. Seeding with 17.13 wt% excess ?-Si3N4 powder of ?400 nm particle size resulted in an aluminum nitride deficient ?'-SiAlON grain size of 0.77 ?m. The excess Si3N4 sample shows better textual contrast than the AlN deficient samples, but UV-visible spectroscopy analyses show that the seeded samples have lower total transmission in comparison to the AlN deficient samples due to greater absorption processes from free Si. It was concluded that birefringence and absoprtion processes by free Si are the dominant sources of visible light transmission loss in ?'-SiAlON and that more work is needed is resolve these issues.


---

## Enter List of papers submitted or published that acknowledge ARO support from the start of the project to the date of this printing. List the papers, including journal references, in the following categories:

### (a) Papers published in peer-reviewed journals (N/A for none)

Received Paper

**TOTAL:**

**Number of Papers published in peer-reviewed journals:**

---

### (b) Papers published in non-peer-reviewed journals (N/A for none)

Received Paper

**TOTAL:**

**Number of Papers published in non peer-reviewed journals:**

---

### (c) Presentations

**Number of Presentations:** 0.00

## Non Peer-Reviewed Conference Proceeding publications (other than abstracts):

Received Paper

**TOTAL:**

**Number of Non Peer-Reviewed Conference Proceeding publications (other than abstracts):**

## Peer-Reviewed Conference Proceeding publications (other than abstracts):

Received Paper

**TOTAL:**

**Number of Peer-Reviewed Conference Proceeding publications (other than abstracts):**

## (d) Manuscripts

Received Paper

**TOTAL:**

**Number of Manuscripts:**

## Books

Received Book

**TOTAL:**

| Received | Book Chapter |
|---|---|

**TOTAL:**

## Patents Submitted

## Patents Awarded

## Awards

### Graduate Students

| NAME | PERCENT_SUPPORTED |
|---|---|
| **FTE Equivalent:** | |
| **Total Number:** | |

### Names of Post Doctorates

| NAME | PERCENT_SUPPORTED |
|---|---|
| Ismail Ozgur Ozer | 0.50 |
| **FTE Equivalent:** | **0.50** |
| **Total Number:** | **1** |

### Names of Faculty Supported

| NAME | PERCENT_SUPPORTED | National Academy Member |
|---|---|---|
| Gary Messing | 0.05 | |
| **FTE Equivalent:** | **0.05** | |
| **Total Number:** | **1** | |

### Names of Under Graduate students supported

| NAME | PERCENT_SUPPORTED |
|---|---|
| **FTE Equivalent:** | |
| **Total Number:** | |

## Student Metrics

This section only applies to graduating undergraduates supported by this agreement in this reporting period

The number of undergraduates funded by this agreement who graduated during this period: ..... 0.00

The number of undergraduates funded by this agreement who graduated during this period with a degree in science, mathematics, engineering, or technology fields:..... 0.00

The number of undergraduates funded by your agreement who graduated during this period and will continue to pursue a graduate or Ph.D. degree in science, mathematics, engineering, or technology fields:..... 0.00

Number of graduating undergraduates who achieved a 3.5 GPA to 4.0 (4.0 max scale):..... 0.00

Number of graduating undergraduates funded by a DoD funded Center of Excellence grant for Education, Research and Engineering:..... 0.00

The number of undergraduates funded by your agreement who graduated during this period and intend to work for the Department of Defense ..... 0.00

The number of undergraduates funded by your agreement who graduated during this period and will receive scholarships or fellowships for further studies in science, mathematics, engineering or technology fields: ..... 0.00

## Names of Personnel receiving masters degrees

| NAME |
|---|
| Carl S. Morandi |
| **Total Number:** 1 |

## Names of personnel receiving PHDs

| NAME |
|---|
| **Total Number:** |

## Names of other research staff

| NAME | PERCENT_SUPPORTED |
|---|---|
| Elizabeth R. Kupp | 0.50 |
| **FTE Equivalent:** | **0.50** |
| **Total Number:** | **1** |

## Sub Contractors (DD882)

## Inventions (DD882)

## Scientific Progress

## Technology Transfer

N/A

The Pennsylvania State University

The Graduate School

Department of Materials Science and Engineering

# THE EFFECT OF SECONDARY PHASES AND BIREFRINGENCE ON VISIBLE LIGHT TRANSMISSION IN TRANSLUCENT α'-SIALON CERAMICS

FINAL REPORT

for

GRANT NO: W911NF-10-1-0478

Dr. Gary Messing, Principal Investigator

Carl S. Morandi

## ABSTRACT

α'-SiAlON ceramics have the potential to replace modern transparent ceramic ballistic windows such as AlON, spinel, and sapphire due to their superior hardness and lower density. However, very limited research has been done to understand the processing-microscructure-property relationships that govern the optical properties of α'-SiAlON ceramics. In order to understand these relationships, this thesis explores the factors that control the formation of AlN-polytypoids and the dominant sources of visible light transmission loss in α'-SiAlON ceramics.

A preliminary study was performed to produce transparent α'-SiAlON with equivalent or superior forward light transmission of α'-SiAlONs reported in the published literature. The resulting samples were analyzed using backscatter electron microscopy and energy dispersive spectroscopy. Residual AlN-polytypoid and amorphous glass were observed as secondary phases.

Due to the lack of knowledge about the refractive indices for AlN-polytypoids, the effects of the AlN-polytypoids on visible light transmission in α'-SiAlON were explored by attempting to remove the phase from the microstructure. Based on a review of the literature, it is proposed that AlN-polytypoid formation occurs via heterogeneous nucleation on large AlN-particles. Various compositions were made to reduce the AlN-polytypoid concentration based on the α'-SiAlON formation reaction sequence and the heterogeneous nucleation hypothesis. Utilizing backscatter electron microscopy, the amount of AlN-polytypoids was determined for each composition. The results show that large AlN particles nucleate AlN-polytypoid phases. When utilizing excess liquid phase, the AlN-polytypoid concentration is dependent on the relative composition of the liquid phase. When the samples are AlN deficient, there is a significant decrease in the AlN-polytypoid concentration due to the increased driving force for AlN particle dissolution and the presence of fewer AlN particles.

The optical properties of the compositionally shifted α'-SiAlON ceramics were compared utilizing a backlit background and viewing the textual contrast with the sample 10 cm above the background. UV-visbile spectroscopy was utilized to quantify the optical properties on the

ceramics. A correlation was not found between the visible light transmission of the various compositions and the AlN-polytypoid concentration. Stronger absorptions and other potential scattering sources were observed in samples with excessive residual amorphous glass phase. A trend was found between the residual amorphous glass phase concentration and the light transmission, but only at high (>2-3 vol%) concentrations. It was concluded that neither the amorphous glassy grain boundary phase nor AlN-polytypoids were acting as the dominant light scattering source in this study's α'-SiAlON ceramics. Absorption by free Si is believed to account for some of the transmission losses based on the absorbance peaks around 300 nm to 320 nm in all samples.

The effects of birefringent scattering on the light transmission were explored by analyzing the grain size of the various α'-SiAlON ceramics. A general trend among all samples could not be found due to either the small differences in grain size or the presence of other scattering/absorption sites. The aluminum nitride deficient samples showed the largest changes in grain size and improvement in the transmission. Based on these samples, an attempt was made to reduce the grain size further by seeding the microstructure of α'-SiAlON with excess α-$Si_3N_4$ from the commercial powder. The minimum α-$Si_3N_4$ nuclei size in the samples was determined to be ≈400 nm. The addition of 17.13 wt% excess α-$Si_3N_4$ powder with respect to the sample weight was predicted to reduce the grain size to 0.7 μm. The resulting seeded sample had a grain size of 0.77 μm. It was concluded that the larger particles in the initial α-$Si_3N_4$ powder limited the reduction of the average grain size. Additionally, x-ray diffraction found that J' phase formed as an intermediate phase during sintering which may have further reduced the potential number of excess α-$Si_3N_4$ nuclei. Qualitatively, the excess $Si_3N_4$ sample shows better textual contrast than the AlN deficient samples when looking at backlit text, but the UV-visible spectroscopy analysis shows less total transmission in the seeded sample with respect to the AlN deficient samples, which was attributed to greater absorption processes from free Si. The improvement in the total transmission in the aluminum nitride deficient and seeded samples with respect to the other samples was attributed to a reduction in the grain size. It was concluded that birefringence and absoprtion processes by free Si were the dominant sources of visible light transmission loss in the samples.

## TABLE OF CONTENTS

# List of Figures

## LIST OF TABLES

# Acknowledgements

This thesis was a collaborative work from several former members of Dr. Messing's group. First, I would like to thank Dr. Messing for his guidance in my research studies and helping further my development as a scientist. I would like to thank Giulio Parcianello for the initial studies he performed in this thesis. Additionally, I would like to thank Julie Anderson for helping me when I started to work on the α'-SiAlON research.

I am greatly indebted to past members of Dr. Messing's group (Yunfei Chang, Stephen F. Potelerala and Ozgur Ozer) for all of the discussions and advice they gave me over my research. Additionally, Ozgur Ozer helped with many of the aspects of the research discussed in this thesis. This thesis would not have been possible without his support.

# Chapter 1

## Introduction

### 1.1 Motivation

Silicon aluminum oxynitride (SiAlON) ceramics are industrially important materials because they can be processed at lower temperatures and have better creep and oxidation resistance than $Si_3N_4$.[1; 2] β'-SiAlON and α'/β' SiAlON composite ceramics are used for molten metal handling and chemical processing, cutting tools, bearings, and wear parts due to the excellent mechanical and chemical properties. Recent research suggests that SiAlON ceramics may be also used for optical applications such as transparent ballistic windows.[3-6]

Ballistic windows require high hardness to shatter high velocity projectiles and low denisty to reduce vehicle weight. α'-SiAlON is a candidate for replacing modern ceramic transparent armors like AlON and spinel due to its higher hardness (>19 to 22 GPa) and lower theoretical density (3.3 to 3.7 g/cm$^3$ depending on the stabilizing cation).[7; 8] Karunaratne *et. al.* first reported transmission in the optical spectrum in α'-SiAlON.[4] Figure 1.1 shows the optical transmission of their Yb-α'-SiAlON. Karunaratne *et. al.* produced translucent Yb-α'-SiAlON by pressureless sintered under a high purity nitrogen atmosphere. In contrast to a sample hot pressed under a vacuum in a graphite die, the sample was translucent, while the hot pressed sample resembled typical grey-black SiAlON ceramics. They said that the difference in optical properties was due to a change in valence of $Yb^{3+}$ to $Yb^{2+}$. Though no direct evidence of their

hypothesis was shown, their work demonstrates that careful control of processing conditions is required to obtain optically translucent α'-SiAlON ceramics.

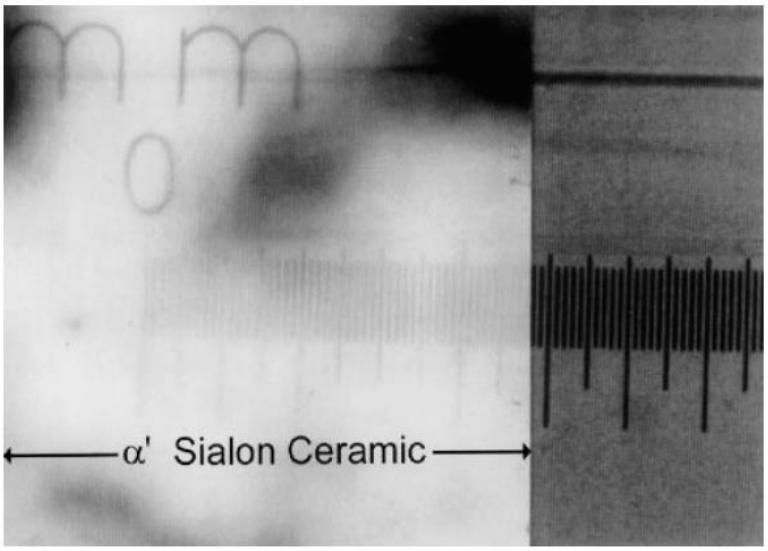


**Figure 1.1 – Karunaratne *et. al.'s* 100 µm thick Yb-α'-SiAlON sample. The sample was placed directly on top of a mm scale with backlighting and the writing can be seen behind it.[4]**

Figure 1.2 illustrates the most transparent α'-SiAlON ceramics produced to date.[9] Chen *et. al.* investigated the transmission and absorption characteristics of α'-SiAlON ceramics stabilized with various rare earths.[9; 10] The 0.3 mm thick ceramics shown in Figure 1.2 appear to have a high transmission in the visible spectrum, with the maximum forward transmission of the samples ranging from about 40% to 65% at 700 nm.[9] Chen *et. al.* also produced 1.06 mm thick Gd-α'-SiAlON with a similar forward transmission of ≈50% at 700 nm.[9; 10] Chen *et. al.* claim that careful processing, the removal of amorphous phase, and reduction of carbon contamination are the primary reasons for the increased transmission.[9; 10] However, they show no direct evidence of their hypotheses and do not consider other possible relationships between processing and transmission loss such as any effects of $Si_3N_4$ decomposition on α'-SiAlON formation, free silicon formation, and impurity silicide formation. Most studies reporting translucent α'-SiAlON

provide possible explanations for transmission loss, but there are few in depth analyzes to explain the sources of transmission loss. Thus, α'-SiAlON ceramics are promising candidates for armor ceramics, but further work is needed to identify the source of optical transmission loss in the visible spectrum.

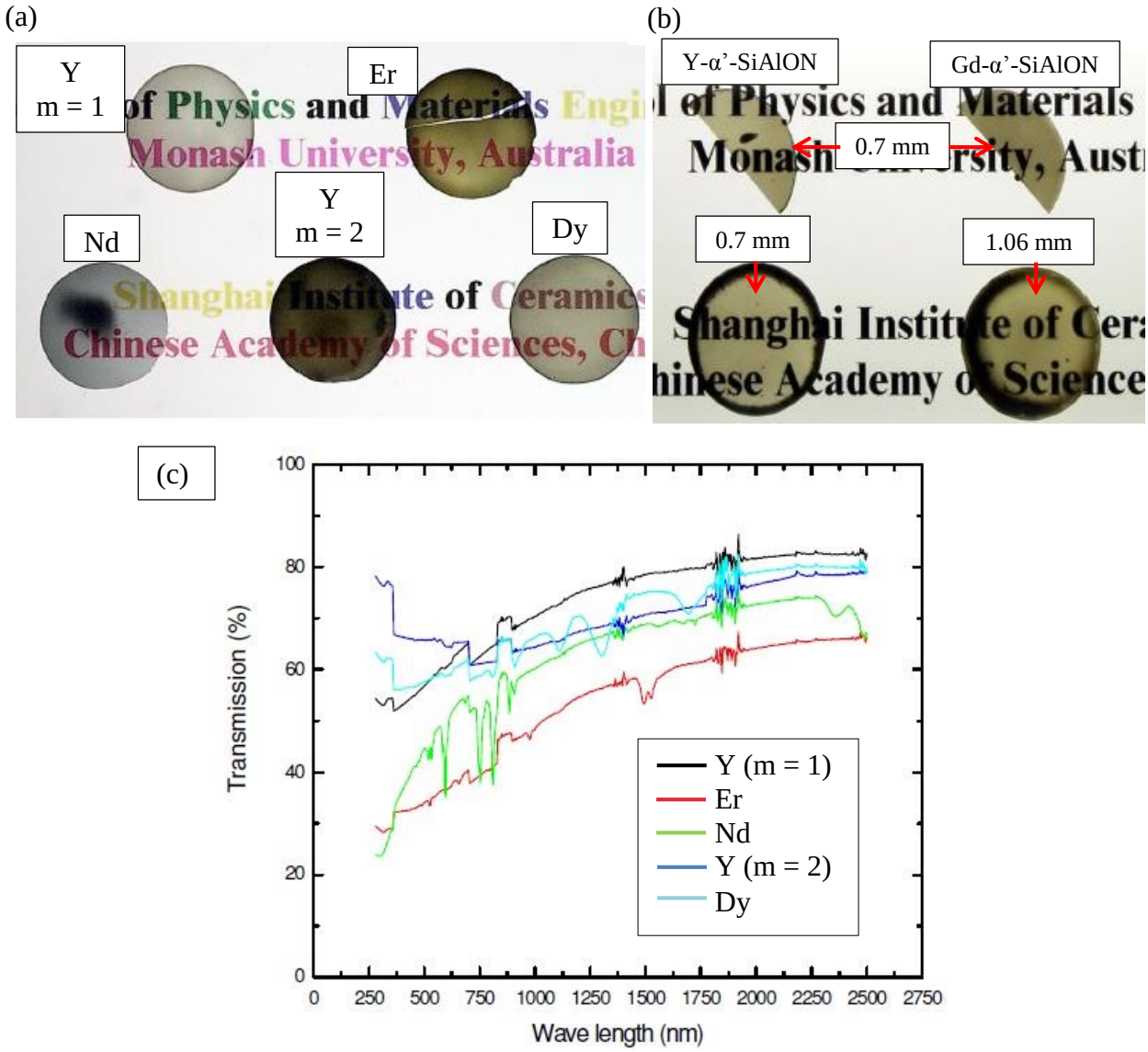


**Figure 1.2 – (a) and (b) The pictures illustrate the best reported transparent samples RE-α'-SiAlON samples reported in the literature. (a) All sample thicknesses are approximately 0.3 mm. The specific stabilizing cation for each sample is labeled in the Figure. (b) High forward transmission in thicker Y-α'-SiAlON and Gd-α'-SiAlON samples. (c) Optical transmission spectrum of each sample in (a).[9]**

In transparent materials, there are three sources of transmission loss: surface reflection, absorption and scattering. Surface reflection is a fundamental loss due to the change in refractive index between air and the material. Liu *et. al*. estimated the theoretical transmission of α'-SiAlON to be 76.5%.[11] Characteristic absorptions in α'-SiAlON are dependent on the rare earth (RE) cation utilized for stabilization. The optical spectra in Figure 1.2(b) show distinct absorption peaks for Nd-α'-SiAlON in the optical spectrum. Shen *et. al.* also demonstrated that Er, Nd, Yb, and Sm α'-SiAlON samples have characteristic absorptions in the visible wavelength range.[12] $Y^{3+}$ has been shown to stabilize α'-SiAlON while avoiding characteristic absorptions in the visible spectrum.[12] Therefore, absorption in Y-α'-SiAlON ceramics could be due to impurities, electronic defects, secondary phases, or a diffuse band edge within the material.

Considering the factors above, light scattering defects in α'-SiAlON ceramics may be responsible for the lower than theoretical optical transmission. Figure 1.3 illustrates the the optical transmission in a representative Y-α'-SiAlON sample made during a preliminary study. As the sample is raised above a backlit background, text clarity diminishes, indicating light scattering. Figure 1.3(c) shows that the forward transmission of the sample is ≈63.2% at 700 nm, which is equivalent or superior to the reports in the literature.

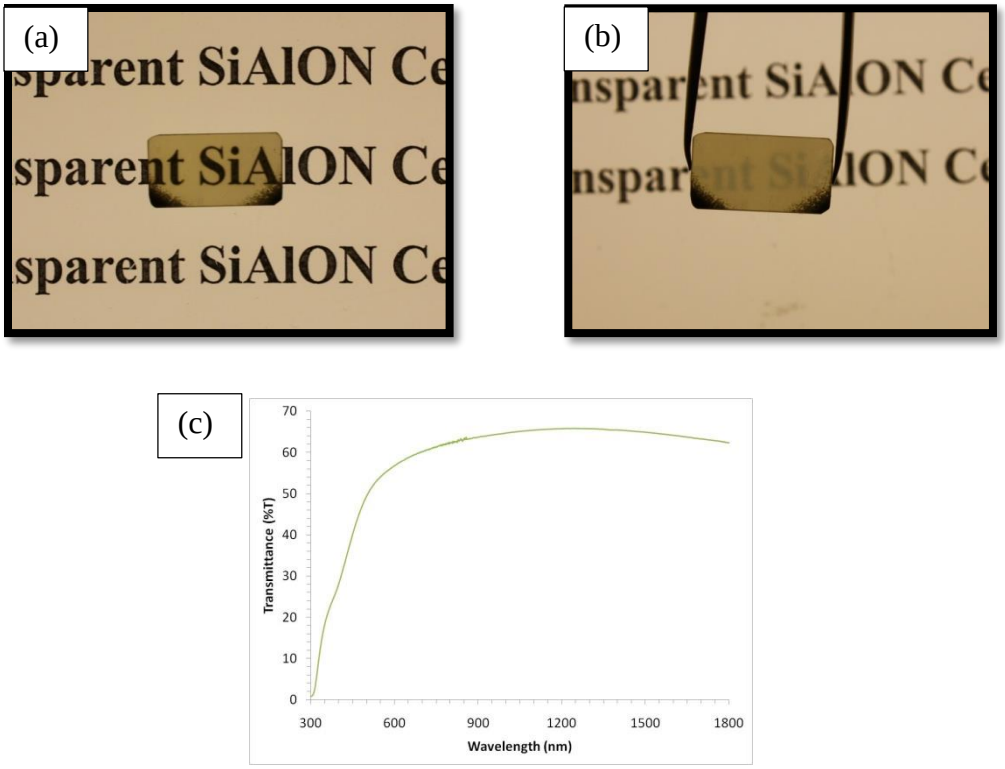


**Figure 1.3 – 0.67 mm thick Y-α'-SiAlON placed directly on top of the background (a) and 5 cm above the background (b). (c) Forward transmission data of the sample in (a). The sample was made via hot pressing as described in chapter 3. Sample provided courtesy of Giulio Parcianello.**

The three primary scattering sources in transparent ceramics are porosity, birefringence, and secondary phases, as illustrated in Figure 1.4. Transparent ceramic research shows that porosity is the most significant scattering source.[13-15] However, multiple reports show SEM and / or TEM micrographs of α'-SiAlON with very little or no residual porosity after sintering, suggesting that residual porosity may not be the primary issue for producing transparent α'-SiAlON.[8; 16-20]

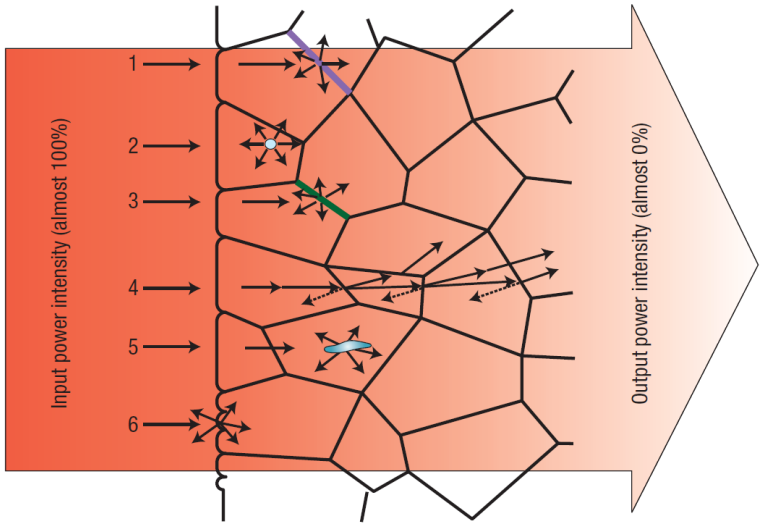


**Figure 1.4 – Schematic of potential light scattering sources in a nominally transparent polycrystalline material. (1) Grain Boundaries, (2) Porosity, (3) Secondary Phases, (4) Birefringence, (5) Secondary Phase Inclusions, and (6) Diffuse Surface Scattering.[21]**

A review of the "transparent" α'-SiAlON literature shows most α'-SiAlON ceramics contain secondary phases such as amorphous grain boundary phases, nitrogen melilite ($R_2Si_{3-x}Al_xO_{3+x}N_{4-x}$, M'), garnet ($R_3Al_5O_{12}$), AlN-polytypoid, and β-SiAlON.[8; 18; 19] Secondary phases can scatter light due to a refractive index difference with α'-SiAlON. Based on the similar crystal structure and composition between α-$Si_3N_4$ and α'-SiAlON and the refractive index estimation of 2.08 by Xu and Chang, I believe the refractive index of α'-SiAlON is similar to amorphous-$Si_3N_4$ (≈2 in the visible spectrum).[22-24] Amorphous RE-SiAlON glasses have a refractive index that varies from ≈1.74 to ≈1.85 depending on the RE cation and nitrogen concentration.[25] The refractive index is not known for most crystalline secondary phases. However, the refractive index difference between α'-SiAlON and each secondary phase is not likely to be the same due to their varying compositions and crystal structures. Thus, these secondary phases may contribute to significant transmission loss.

α'-SiAlON is optically birefringent due to its trigonal (P31c) crystal structure. Apetz and Bruggen demonstrated that the real inline transmission of a polycrystalline birefringent material can be modeled based on equation 1.1:[13]

$$RIT = T_{th}\exp(\frac{-3\pi^2\Delta n^2 rd}{n^2\lambda^2}) \quad \text{(eq. 1.1)}$$

where $T_{th}$ is the theoretical transmission, Δn is the difference in refractive index, n is the average refractive index, 2r is the grain size, λ is wavelength of the radiation in a vacuum, and d is the sample thickness.[13] Using the above model, Lui *et. al.* estimated the refractive index and the refractive index anisotropy of α'-SiAlON were between 2.05-2.17 and 0.0045-0.0136, respectively.[11] They concluded that the primary scattering source in translucent α'-SiAlON is birefringence.[11]

Based on a preliminary analysis of the published literature, it is proposed that secondary phases and birefringence are the most likely causes of transmission loss in α'-SiAlON ceramics. Therefore, the effects of processing parameters on the formation of phase pure α'-SiAlON ceramics will be investigated using particle size analysis, sintering studies and microstructural analysis. The areas addressed with regards to the role of processing on the microstructure are:

- The effect of the particle size distribution of AlN and $Si_3N_4$ on the formation of AlN-polytypoids and α'-SiAlON, respectively
- The effect of AlN polytypoid content, amorphous glass content, and α'-SiAlON grain size on the transmission of light through α'-SiAlON

## 1.2 Organization of the Thesis

Chapter 2 reviews the literature covering the fabrication and processing of transparent ceramics to establish the extrinsic features affecting transparency in polycrystalline ceramics. Discussions on transparent ceramics, on processing SiAlON ceramics and on the reaction sequences during α'-SiAlON processing are included.

Chapter 3 is divided into 3 sections covering AlN-polytypoid formation and removal, the effects of the secondary phases on visible light transmission, and the effects of birefringent scattering on the visible light transmission in Y-α'-SiAlON:

The first section presents a study on the formation and removal of AlN polytypoids in Y-α'-SiAlON ceramics. A preliminary study established the conditions for obtaining a literature equivalent translucent Y-α'-SiAlON ceramic. AlN-polytypoids are determined to be the secondary phase that forms in the translucent α'-SiAlON. A link between the AlN particle size distribution and AlN polytypoid phase formation is proposed. Various powder compositions were fabricated to explore the dissolution of the larger AlN particles during α'-SiAlON processing. The studies show that AlN polytypoid formation in α'-SiAlON ceramics is not limited by thermodynamics, but it is a kinetic phenomenon dictated by a heterogeneous nucleation and growth mechanism.

The second section discusses the relationship between the secondary phases in the various composition shifted α'-SiAlON samples and the visible light transmission. Optical property comparisons were made by examining the quality of backlit text through a sample placed 10 cm above the backlit background and using UV-visible spectroscopy. A correlation was not found between the AlN-polytypoid concentration and the light transmission. The

transmission was found to decrease with increasing glass content, but the AlN deficient samples suggest that the glass may not act as a dominant light scattering source until its concentration is greater than 2 to 3 volume %. Thus, neither the AlN-polytypoid nor the residual amorphous glass phases act as the dominant scattering mechanism. Light absorbance spectra show absorbance peaks which are attributed to Si absorption. Free Si absorption is identified as a potential significant source of visible light transmission loss.

The third section discusses the effects of birefringence on visible light transmission through α'-SiAlON ceramics. Theory predicts improved optical transmission with decreasing grain size. Based on the results of the AlN deficient samples, an attempt was made to intentionally seed the microstructure with excess $Si_3N_4$ to reduce the α'-SiAlON grain size. The seeded sample had a grain size of 0.77 μm and improved transmission relative to samples with larger grain sizes except the aluminum nitride deficient samples, due to an increase in absorption. It is concluded that birefringence and free Si absorption are dominant sources of light transmission losses in the samples. Finally, the effects of nucleation frequency in α'-SiAlON ceramics and the factors that control the final grain size are discussed.

Chapter 4 suggests future studies from which a better understanding of α'-SiAlON and other SiAlON ceramic processing may lead to improved optical property performance.

## 1.3 References


[1]D. P. Thompson, "Innovation in SiAlON Ceramics," *Key Eng. Mater.,* **352,** 137-46 (2007).

[2]K. H. Jack, "Review: Sialons and Related Nitrogen Ceramics," *J. Mater. sci.,* **11,** 1135-58 (1976).

[3]I.-W. Chen and A. Rosenflanz, "A Tough SiAlON Ceramic Based on α-$Si_3N_4$ with a Whisker-like Microstructure," *Letters to Nature,* **389,** 701-04 (1997).

[4]B. S. B. Karunaratne, R. K. Lumby and M. H. Lewis, "Rare-Earth-Doped α'-Sialon Ceramics with Novel Optical Properties," *J. Mater. Res.,* **11,** [11] 2790-94 (1996).

[5]J. W. H. v. Krevel, H. T. Hintzen and R. Metselaar, "On the $Ce^{3+}$ Luminescence in the Melilite-Type Oxide Nitride Compound $Y_2Si_{3-x}Al_{x+3}N_{4-x}$," *Mat. Res. Bull.,* **35,** 747-54 (2000).

[6]J. W. H. v. Krevel, J. W. T. v. Rutten, H. Mandal, H. T. Hintzen, and R. Metselaar, "Luminescence Properties of Terbium-, Cerium-, or Eruopium-Doped α-SiAlON Materials," *J. Solid State Chem.,* **165,** [19-23] (2002).

[7]I.-W. Chen, R. Shuba and M. Y. Zenotchkine, "Development of Tough Alpha-SiAlON," *Key Eng. Mater.,* **237,** 65-78 (2003).

[8]M. I. Jones, H. Hyuga, K. Hirao, and Y. Yamauchi, "Highly Transparent Lu-α-SiAlON," *J. Am. Ceram. Soc.,* **87,** [4] 714-16 (2004).

[9]W. W. Chen, Y. B. cheng, P. I. Wang, and D. S. Yan, "Novel Optical Ceramics: α-Sialons," *Key Eng. Mater.,* **264-268,** 905-08 (2004).

[10]W.-W. Chen, X.-L. Su, P.-L. Wang, and D.-S. Yan, "Optical Properties of Gd-α-Sialon Ceramics: Effect of Carbon Contamination," *J. Am. Ceram. Soc.,* **88,** [8] 2304-06 (2005).

[11]L. Liu, F. Ye, S. Zhang, B. Peng, W. Luo, Z. Zhang, and Y. Zhou, "Light Transmittance in α-SiAlON Ceramics: Effects of Composition, Microstructure, and Refractive Index Anisotropy," *J. Euro. Ceram. Soc.,* **32,** 2487-94 (2012).

[12]Z. Shen, M. Nygren and U. Halenius, "Absorption Spectra of Rare-Earth-Doped α-SiAlON Ceramics," *J. Mater. Sci. Lett.,* **16,** 263-66 (1997).

[13]R. Apetz and M. P. B. v. Bruggen, "Transparent Alumina: A Light-Scattering Model," *J. Am. Ceram. Soc.,* **86,** [3480-486] (2003).

[14]G. J. Peelen and R. Metselaar, "Light Scattering by Pores in Polycrystalline Materials-Transmission Properties of Alumina," *J. Appl. Phys.,* **45,** [1] 216-20 (1974).

[15]A. Ikesue and K. Yoshida, "Scattering in Polycrystalline Nd:YAG Lasers," *J. Am. Ceram. Soc.,* **81,** [8] 2194-96 (1998).

[16]Y. Xiong, Z. Fu, H. Wang, W. Wang, J. Zhang, and Q. Zhang, "Translucent Mg-α-Sialon Ceramics Prepared by Spark Plasma Sintering," *J. Am. Ceram. Soc.,* **90,** [5] 1647-49 (2007).

[17]R. Shuba and I.-W. Chen, "Refractory α-SiAlON Containing $La_2O_3$," *J. Am. Ceram. Soc.,* **89,** [9] 2860-68 (2006).

[18]Y. Xiong, Z. Y. Fu, H. Wang, Y. C. Wang, J. Y. Zhang, and Q. J. Zhang, "Microstructure and Properties of Translucent Mg-SiAlON Ceramics Prepared by Spark Plasma Sintering," *Mater. Sci. Eng., A,* **488,** 475-81 (2008).

[19]J. Xue, Q. Liu and L. Gui, "Lower-Temperature Hot-Pressed Dy-α-Sialon Ceramics with a LiF Additive," *J. Am. Ceram. Soc.,* **90,** [5] 1623-25 (2007).

[20]H. Mandal, "New Developments in α-SiAlON Ceramics," *J. Euro. Ceram. Soc.*, **19,** 2349-57 (1999).
[21]A. Ikesue and Y. L. Aung, "Ceramic Laser Materials," *Nature Photonics,* **2,** 721-27 (2008).
[22]T. Baak, "Silicon Oxynitride; a Material for GRIN Optics," *Appl. Optics,* **21,** [6] 1069-72 (1982).
[23]J. T. Boyd and C. S. Kuo, "Composite Prism-Grating Coupler for Coupling Light into High Refractive Index Thin-Film Waveguides," *Appl. Optics,* **15,** [7] 1682-83 (1976).
[24]Y.-N. Xu and W. Y. Ching, "Electronic Structure and Optical Properties of α and β Phases of Silicon Nitride, Silicon Oxynitride, and with Comparison to Silicon Dioxide," *Phys. Rev. B,* **51,** [24] 17379-89 (1995).
[25]D. N. Coon and T. E. Doyle, "Refractive Indices of Glasses in the Y-Al-Si-O-N System," *J. Non.-Cryst. Solids,* **108,** [180-186] (1989).

# Chapter 2

## Literature Review

### 2.1 Transparent Ceramics

Light transmission through a material decreases as a result of surface reflection, absorption and light scattering. Consider light interacting with an ideal transparent material. Surface reflection of the light occurs due to a change in the density of electrons (i.e. refractive index) and polarization of the electrons.[1] Thus, surface reflection defines the theoretical limit for light transmission through a transparent medium. Table 2.1 compares the theoretical transmission limit of technologically important, optically transparent ceramics with α'-SiAlON.[2] Due to its higher refractive index, α'-SiAlON has a lower theoretical transmission limit than the common oxides.

| Material | Refractive Index at 400 nm | Theoretical Transmission at 400 nm (%) | Common Usage |
|---|---|---|---|
| $Y_3Al_5O_{12}$ (YAG)[3] | 1.86 | 82.7 | Laser Gain Media |
| $MgAl_2O_4$ (Spinel)[3] | 1.74 | 85.9 | Transparent Armor |
| $Al_2O_3$ (Sapphire)*[3] | 1.778-1.786 | 84.6 | Lighting Envelope / Missile and Radar Domes |
| $Al_{23}O_{39}N_5$ (γ-AlON)[3] | 1.81 | 84.1 | Transparent Armor |
| Crown Glass (K4A)[4] | ≈1.52 | 91.7 | Windows and Lenses |
| Fused Silica[5] | ≈1.47 | 92.9 | Lighting Envelope / UV photography lenses / High Temperature Tubes and Glass |
| *a*-$Si_3N_4$[6] | ≈2.07 | 77.1 | Oxygen Barrier / Passivation / Dielectric Layer in Semiconductor Devices and Antireflection Coatings |
| α'-SiAlON** | ≈2.05-2.17 | ≈76.5 | Cutting tools / Nonferrous Molten Metal Handling / Bearings |

**Table 2.1 – Theoretical transmission of common transparent ceramics. The theoretical transmission was calculated using the formula $\boldsymbol{T(\%) = 100[1 - \left(\frac{n-1}{n+1}\right)^2]^2}$. [1; 7]**
***Both the ordinary and extraordinary refractive indices are indicated based on a birefringence of 0.008 for $Al_2O_3$.**
****Refractive index of α'-SiAlON is reported as an average instead of at specific wavelengths.[2]**

Absorption processes also determine the fundamental limits of transmission in materials. A material's band gap is the most important factor when considering its optical properties. Optical property information for α'-SiAlON is limited, but Li *et. al*. reported experimental optical gaps (equivalent to the band gap in many materials) of 5.44 eV and 5.25 eV for Ca-α'-SiAlON and Lu-α'-SiAlON, respectively, using diffuse reflectance spectroscopy.[8] These values are consistent with the optical gap for α-$Si_3N_4$ calculated by Xu and Ching.[9] The electronic band

structures of α'-SiAlON and α-$Si_3N_4$ are likely to be similar as well because of the similarities in the optical gaps and the crystal structures. Xu and Ching calculated the electronic band gap of α-$Si_3N_4$ to be 4.63 eV, which is well above the ≈3.1 eV band gap limit required for visible light transmission.[9] Thus, a single crystal α'-SiAlON should be completely transparent when exposed to visible light.

Cations (typically rare earths (RE), Ca, Li, or Mg) utilized for stabilization of α'-SiAlON can introduce characteristic absorptions, or color centers, in α'-SiAlON's electronic structure. Figure 2.1 shows the absorption spectra of α'-SiAlON samples fabricated by Shen *et. al*.[10] When utilizing Er, Nd, Sm, and Yb as stabilizing cations, there is at least one characteristic absorption peak. Yb-α'-SiAlON shows the strongest absorption at ≈425 nm which is attributed to the $4f^{13}$ to $5d^1$ transition of $Yb^{2+}$ ions. However, Dy, Y, and Tb have either very weak absorption peaks or none at all. Additionally, all samples show an absorption edge of 280-340 nm. Thus, characteristic absorptions in the visible spectrum could be avoided by utilizing the correct stabilizing cation, but no one, to the author's knowledge, has demonstrated clear α'-SiAlON except in extremely thin samples (≈100μm thickness). Plausible reasons for this may be due to electronic defects such as electron/hole trapping in vacancies, Si/silicide formation, or impurity ions/phases in the microstructure (such as iron/iron silicide).[11-13] Also, due to the limited knowledge of the electronic structure of α'-SiAlON, it is possible that the band gap is much closer to 3.1 eV or that the band edge is very diffuse.

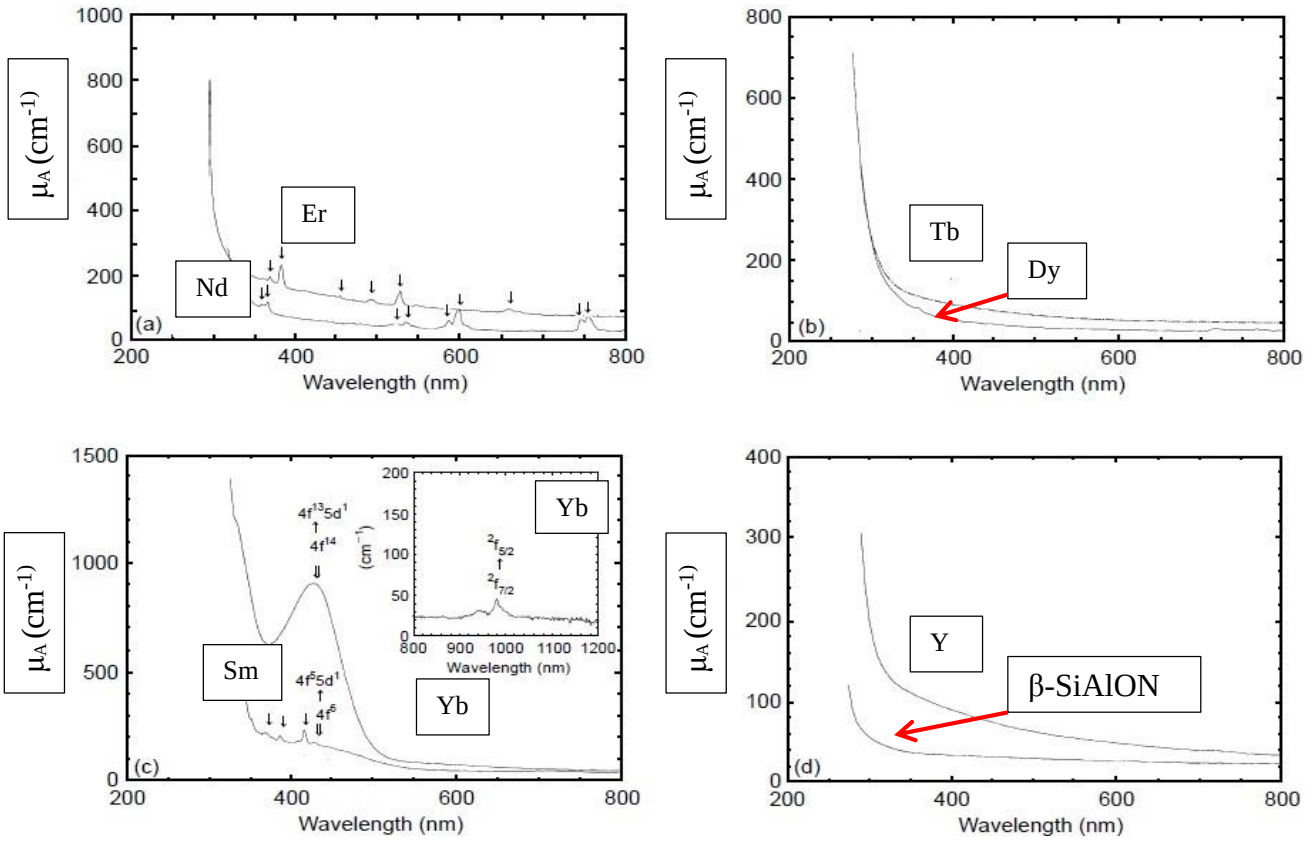


**Figure 2.1 - α'-SiAlON UV-visible absorption spectra utilizing (a) Nd and Er, (b) Tb and Dy, (c) Yb and Sm, and (d) Y as stabilizing cations. The spectra of pure β-SiAlON (z=3.5) is shown in (d) for comparison. The (↓) identify specific absorption peaks in the Er, Nd, Sm, and Yb samples.[10]**

Even if only stabilizing cations which do not show characteristic absorptions in α'-SiAlON are used, α'-SiAlON ceramics in the literature show much less transmission than the proposed theoretical transmission of 76.5%. Jones *et. al* reported the highest forward transmission of ≈70% 700 nm for a 0.5 mm thick Lu-α'-SiAlON.[14] A scattering source(s) is likely responsible for the remaining additional transmission loss.

Scattering of light occurs wherever there is a significant change in the refractive index as light travels through the material. Typical scattering defects seen in transparent media include porosity, surface scattering, grain boundaries, secondary phases at grain boundaries, grain-to-

grain birefringence and secondary phase inclusions.[15; 16] Figure 2.2 shows a schematic of the various scattering sources.[16]

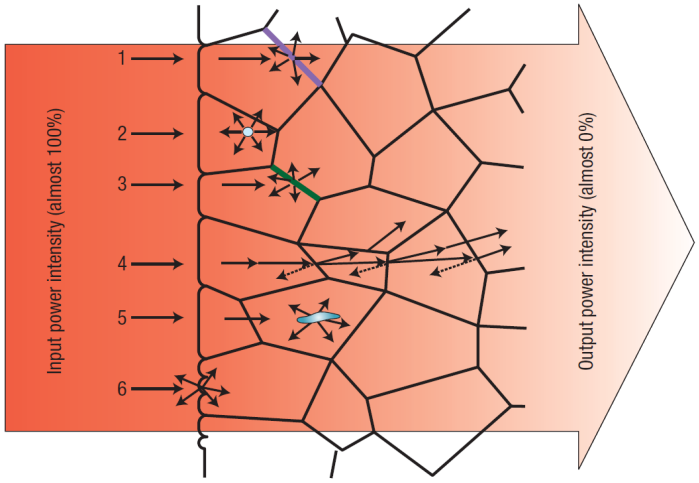


**Figure 2.2 – Schematic of potential light scattering sources in a nominally transparent polycrystalline materials. The labels are (1) Grain Boundaries, (2) Porosity, (3) Secondary Phases, (4) Birefringence, (5) Secondary Phase Inclusions, and (6) Diffuse Surface Scattering.[16]**

Pores exhibit the largest possible difference in refractive index from a host material. Thus, removing pores is required to obtain a transparent material. Ikesue and Furusato demonstrated that a polycrystalline Nd:YAG $\geq$ 99.985% of $\rho_{th}$ is needed to have equivalent optical properties to that of single crystal Nd:YAG.[17] This system is ideal for modeling transparency in polycrystalline materials because it is optically isotropic and can be made with few other scattering sources. Thus, all nominally transparent material must achieve at least this density to remove porosity as a significant scattering source. Multiple reports of "transparent" or translucent α'-SiAlON show little or no porosity in their SEM or TEM images. Instead, most or all potential pores are filled with an amorphous phase due to α'-SiAlON's processing, suggesting that the materials were at or above the density limit proposed by Ikesue and Furusato. Thus, porosity is not believed to be the primary issue limiting α'-SiAlON transmission.

The formation of a liquid phase during sintering and the incomplete formation of α'-SiAlON almost always results in a residual amorphous glass phase which can scatter light. If the amorphous phase's refractive index is close to the refractive index of α'-SiAlON, then it would not scatter light significantly. Coon *et. al*. determined that both the Y and N concentration significantly affect the refractive index in Y-Si-Al-O-N system glasses due to an increase in density and polarizability, respectively. Their glasses had a minimum and maximum refractive index of ≈1.74 and ≈1.85, respectively.[18] Redington *et. al*. and Drew *et. al*. measured the refractive index of several RE-SiAlON glasses which showed only a small difference in refractive index ($\Delta n \leq 0.05$) for equivalent compositions, except for Mg-SiAlON glass which had a refractive index between ≈1.58 and ≈1.6.[19; 20] Thus, no matter which stabilizing cation is used, there is at least a $\Delta n \approx 0.2$ between α'-SiAlON and the amorphous phase based on the refractive indices reported for α'-SiAlON.

Besides the amorphous phase, reports show other crystalline phases such as nitrogen melilite (M', $R_2Si_3$-$xAl_xO_{3+x}N_{4-x}$), garnet ($R_3Al_5O_{12}$), AlN-polytypoids, and β-SiAlON coexist with "transparent" α'-SiAlON.[14; 21-23] As discussed in section 2.2.3 and chapter 3, these secondary phases may form during various reactions in α'-SiAlON formation. The refractive indices of the secondary phases are unknown because of a lack of single crystals. However, several conclusions can be made based on current knowledge. The secondary phases, with the exception of β-SiAlON, have very different overall compositions from α'-SiAlON. As seen in the SiAlON glasses, the high polarizability of nitrogen can significantly affect the refractive index. The crystals with the highest nitrogen content are $Si_3N_4$, α'-SiAlON, β'-SiAlON, AlN and AlN-polytypoids. The other secondary phases will likely have a large difference in refractive index from α'-SiAlON because they contain much less nitrogen. Additionally, many

secondary phase crystals will scatter light because they are birefringent due to their non-cubic nature. Finally, if the AlN-polytypoids are considered to have similar refractive indices as AlN (2.20 and 2.25 at 400 nm), then these phases should also scatter light due to the difference with the reported α'-SiAlON refractive index.[2; 24] β'-SiAlON may not have a significantly different refractive index from α'-SiAlON due to their close overall compositions and crystal structures, but it often grows into long and large crystals which can scatter light due to birefringence.

Porosity, secondary phases, grain boundaries and surface roughness are all factors that are controlled by processing. Absolute removal of the scattering sources may not be necessary in order to achieve theoretical transmission. In fine grain materials (<20 μm), a potential scattering source will scatter light if it is ≥10-50% (depending on the refractive index difference) the size of the specific wavelength of light.[25] Apetz and Bruggen calculated that at 0.1% porosity in $Al_2O_3$, pores begin to scatter visible light at ≈5 nm. Grain boundaries usually do not participate in light scattering because their thickness is much less than the wavelength of light.[26] Thick grain boundaries may scatter and reflect light if there is a change in the refractive index compared to the interior crystal. However, for a small Δn (<0.01) the reflectivity can be ignored except for thick (>10000 grains for each light ray) materials.[25] Secondary phases with large Δn (≥0.005) must be ≤200nm to not scatter light.[25]

Unlike the other scattering sources, birefringence is not controlled by processing, but rather by the inherent crystal structure of the material. Cubic materials are optically isotropic; thus light scattering does not occur from grain to grain due to birefringence. All non-cubic materials are optically anisotropic, having two separate indices of refraction within the same crystal. Apetz and Bruggen demonstrated that the geometric light scattering model developed by Dalisa and Seymour does not apply to fine grain materials (the exact condition is $G\Delta n >$

$2\pi\lambda_m$ where $\lambda_m$ is the wave length in the medium, G is the average grain size and $\Delta n$ is the difference in refractive indices).[25; 27] Instead, they showed Raleigh-Gans-Debye scattering dominates due to the birefringence of the material.[25] This finding explained why a cubic polycrystalline material such as Yttralox (90% $Y_2O_3$ – 10% $ThO_2$) could have a real in-line transmission (RIT) of $> 70\%$, but high density coarse grain (>10 μm) $Al_2O_3$ shows much lower RIT values.[28; 29] Similar to other scattering sources, if the grain size is reduced to less than the wavelength range of interest, then birefringent scattering does not occur.[25] Krell *et. al.* and Apetz and Bruggen demonstrated this possibility when they obtained a real inline transmission (RIT) of $> 60\%$ in $Al_2O_3$ at 645 nm by decreasing the average grain size from 600 nm and 300 nm.[25; 30] The RIT is dependent of grain size, $\Delta n$, and material thickness and it can be calculated using the equation:[25]

$$RIT = T_{th}\exp(\frac{-3\pi^2\Delta n^2 rd}{n^2\lambda^2}) \qquad \text{eq. 2.1}$$

Using the above model, Liu *et. al*. calculated the refractive indices and birefringence of α'-SiAlON.[2] However, the model was used considering only a single scattering source. Their crystalline phase analysis was limited to x-ray diffraction (XRD) and revealed the presence of M' phase in some samples, but reported the others as pure α'-SiAlON except for the residual amorphous phase.[2] TEM images were used to determine the amount of amorphous phase in each sample.[2] As secondary phases can exist below the detection limit, XRD cannot be used as the sole evidence for crystalline phase purity. Backscatter electron imaging and energy dispersive spectroscopy can be used to detect secondary phases due to the elemental contrast. Considering all the potential scattering sources still present in the "transparent" α'-SiAlON materials, the results of their work may be skewed from the true values. The wide range of calculated α'-

SiAlON birefringence values (0.0045-0.0136) could be caused by the differing cations in the samples or by the various amount of scattering sources.[2] In their reported data, samples with the same cation show larger birefringence and refractive index values as the intergranular phase increased which suggests secondary phases are skewing their data.[2]

Considering the above factors, polycrystalline materials for window type applications require:

- A density of $\geq 99.985\%$
- Removal of color centers or avoid materials with permanent absorptions in the wavelength region of interest
- Removal of any large secondary phases with large differences in index of refraction from the host material
- A grain size of $\leq 200$ nm if the material is anisotropic and not textured.

Y-α'-SiAlON ceramics are not expected to have an absorption in the optical wavelength range due to the absence of d electrons in $Y^{3+}$. Also, as described in the section 2.2.2 and 2.2.4, controlling the grain aspect ratio and liquid phase content is easier in this system. For these reasons, the Y- α'-SiAlON system is the focus of this thesis.

## 2.2 α'-SiAlON Background

### 2.2.1 $Si_3N_4$ and SiAlON Crystal Structures

Trigonal α (space group P31c), hexagonal β (space group $P6_3$ or $P6_3/m$), and cubic γ (space group Fd-3m) are the three common crystalline $Si_3N_4$ allotrope phases. Thermodynamically, β-$Si_3N_4$ is the room temperature stable phase, while α and γ formation are

dependent on processing. The most common methods used to produce industrial $Si_3N_4$ powder are carbothermal reduction nitridation of $SiO_2$ and ammonolysis of $SiCl_4$ with $NH_3$.[31] In both methods, metastable α-$Si_3N_4$ generally forms before β-$Si_3N_4$ due to the lower temperature (1300-1500°C) and relatively close free energies.[31-33] γ-$Si_3N_4$ forms at high pressures and temperature.

Though α-$Si_3N_4$ and β-$Si_3N_4$ production is well understood in industry, debates on the crystal structures have continued in the scientific community. Researchers question whether β-$Si_3N_4$'s crystal structure contains a center of symmetry or not. Studies by Bando, Grun, and Ching *et. al*. concluded that the correct symmetry is $P6_3$ using convergent beam electron diffraction (CBED) analysis, free energy calculations, and ab initio methods (orthogonalized-linear combination of atomic orbital), respectively.[34-37] However, studies by Hardie *et. al.*, Bando, and Belkada *et. al*. concluded that the $P6_3/m$ symmetry is correct by using x-ray powder diffraction, CBED of thin β-$Si_3N_4$ crystals and ab initio methods (using Hallmann-Feynman forces), respectively.[37-39] Recent literature favors the $P6_3/m$ symmetry as the correct symmetry because there is no loss in precision in the structural parameters.[40] For this reason, the $P6_3/m$ is used here.

Significant controversy exists on the composition and stabilization of α-$Si_3N_4$. Grieveson *et. al.* proposed that α-$Si_3N_4$ is not a pure nitride, but an oxynitride stabilized by oxygen and vacancies with a composition between $Si_{11.4}O_{0.3}N_{1.5}$ and $Si_{11.5}O_{0.5}N_{1.5}$.[34; 41; 42] However, multiple researchers produced α-$Si_3N_4$ with less oxygen than the proposed compositions.[43-45] Though processing limitations prevent oxygen free α-$Si_3N_4$ production, these results suggest that α-$Si_3N_4$ is not an oxynitride under ideal conditions.[34] Instead, it is proposed that $Si^{4+}$ can change its valence state to $Si^{3+}$ which occupies the interstitial sites to stabilize the structure when oxygen is not present for valency compensation.[46] The stabilization mechanism is similar to how the α'-

SiAlON phase is stabilized as discussed below.[47] Thus, α-$Si_3N_4$ is a pure nitride material stabilized by defects and is capable of forming a wide range solid solution with oxygen.

Figures 2.3 and 2.4 show the ideal β-$Si_3N_4$ and α-$Si_3N_4$ crystal structures, respectively. β-$Si_3N_4$ is a three dimensional network of slightly distorted $SiN_4$ tetrahedra formed via corner sharing with lattice parameters of a = 0.7608 nm and c = 0.2911 nm.[34; 48; 49] The β-$Si_3N_4$ structure forms layers of superimposed puckered Si-N rings with an ABAB stacking sequence and long channels parallel to the [0001].[34; 47] The $Si^{4+}$ ions occupy the 6(h) sites and N ions occupy the 2(c) and 6(h) sites. The α-$Si_3N_4$ crystal structure is similar to that of β-$Si_3N_4$, but it has an ABCDABCD stacking sequence where the CD layer is rotated 180 ° from the AB layer. The rotated CD layers close the channels formed in β-$Si_3N_4$ and form two large interstitial sites. The c-axis is approximately twice as long as that of β-$Si_3N_4$ because of the CD layers. The purest single crystal produced had lattice parameters of a = 0.7818 $\pm$ 0.0003 nm and c = 0.5591 $\pm$ 0.0004 nm.[34; 45] The $Si^{4+}$ atoms occupy two of the 6(c) positions and the $N^{3-}$ atoms occupy the other two 6(c) positions as well as the 2(b) and 2(a) positions.[50]

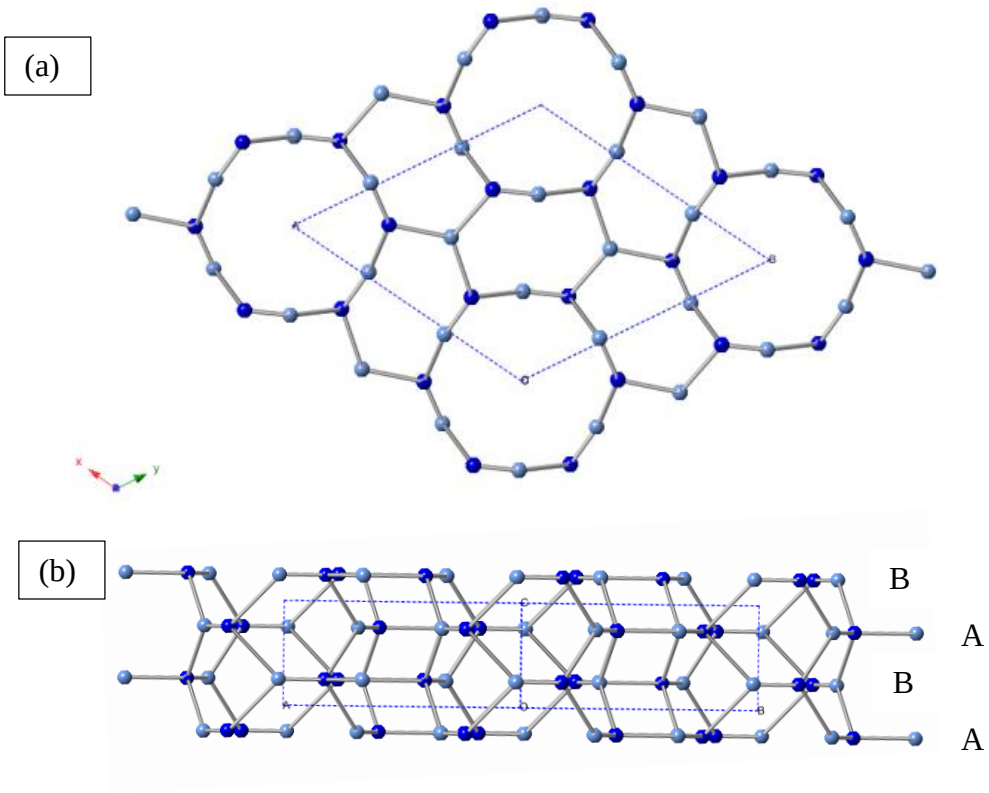


**Figure 2.3 – β-$Si_3N_4$ crystal structure. Dark blue atoms and light blue atoms represent $Si^{4+}$ and $N^{3-}$ respectively. (a) Crystal structure along the [0001] direction showing channels formed by super imposed puckered Si-N rings. (b) Showing stacking sequence of ABAB. The crystal structures were made using Crystal Maker**.

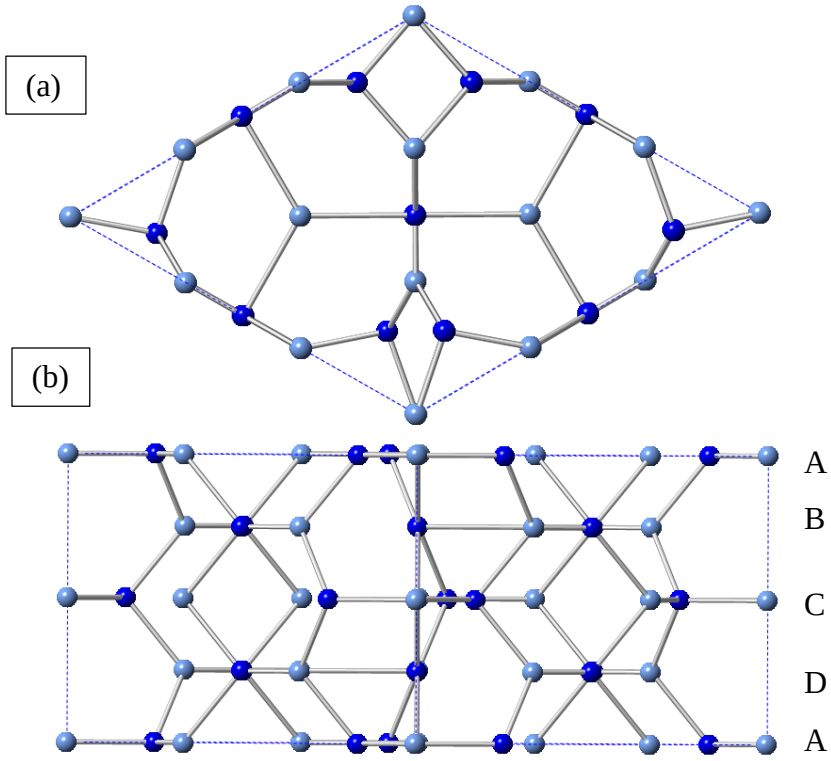


**Figure 2.4 – Idealized α-$Si_3N_4$ crystal structure with empty interstitial sites. Dark blue atoms represent $Si^{4+}$ and light blue atoms represent $N^{3-}$. Stabilizing cations sit inside one of the 2 interstitial sites inside the structure. (a) Viewing the structure down the [001] to show the channels in β-$Si_3N_4$ are no longer present in the α-$Si_3N_4$ structure. (b) Showing the stacking sequence of α-$Si_3N_4$. The crystal structures were made using Crystal Maker.**

Oyama and Kamigaito demonstrated that $Si_3N_4$ forms solid solutions with oxides.[51] The SiAlON systems are the most extensively studied of all $Si_3N_4$ solid solutions. Many solid solution phases in the SiAlON system are isostructural or very similar in structure to the end member compounds in the SiAlON systems (see Figures 2.5 and 2.6) such as the isostructural solid solutions of α-$Si_3N_4$ and β-$Si_3N_4$: α'-SiAlON and β'-SiAlON.[48; 52] In these systems, Al and O directly substitute for Si and N, respectively, in the structures presented in Figures 2.3 and 2.4. β'-SiAlON's composition is commonly described by the formula $Si_{6-z}Al_zO_zN_{8-z}$ where z is the amount of Al and O that substitute into the structure and ranges $0 \leq z \leq 4.2$.[48] The formula describes the average composition along a line with a metal : non-metal atom ratio of 3/4 in the $Si_3N_4$-AlN-$SiO_2$-$Al_2O_3$ phase diagram (see Figure 2.5).[48] The α'-SiAlON phase composition is

described using the general formula $R_{m/v}Si_{12-(m+n)}Al_{m+n}O_nN_{16-n}$ where R is the stabilizing cation, m is the replacement of Si-N bonds with Al-N bonds, n is the replacement of Si-N bonds with Al-O bonds , and v is the valency of the stabilizing cation. Like the β'-SiAlON composition, α'-SiAlON's accepted composition does not specifically denote single phase α'-SiAlON, but an average composition on the "α'-SiAlON" plane (see Figure 2.6). Single phase R-α'-SiAlON's solubility range depends on the stabilizing cation and temperature. In the Y-α'-SiAlON system, the solubility ranges from m = 1 to m = 2.4 and n = 0 to n= 1.2 at 1800 °C (see Figure 2.7).[53] In both α'-SiAlON and β'-SiAlON, the idealized structures are charge compensated by the substituting ions alone.

Solid solution phases with structures based on AlN, mullite, silicon oxynitride, yttrium aluminum monoclinic (YAM), and nitrogen melilite ($R_2O_3 \bullet Si_3N_4$) exist in the R-SiAlON systems as AlN polytypoids, X, O', J', and M' phases, respectively. The AlN-polytypoids are structures similar to the wurtzite AlN structure, but differ due to inversion domain boundaries as the composition changes with Si and O content.[54] The phases are designated using Ramsdell symbols: $2H^{\delta}$, 8H, 12H, 15R, 21R, and 27R where n/3R and n/2H represent different layers of metal atom stacking sequences in rhombohedral crystals and hexagonal crystals, respectively.[48] For example, 8H consists of 8 layers of metal atoms in the form of two $M_4X_5$ (where M is a metal and X is a non-metal) which are related by a c-glide plane.[48; 52] The J' phase's composition is described as $R_4Si_{2-x}Al_xO_{7+x}N_{2-x}$ where the solid solution phase field extends between $R_4Al_2O_9$ and $R_4Si_2O_7N_2$.[55] The M' phase composition is described as $R_2Si_{3-x}Al_xO_{3+x}N_{16-x}$ where the x solubility is limited by the stabilizing cation R. In the Y-SiAlON system, the M' phase has a maximum solid solubility of x = 0.7 in this system.[56] There are other phases in the system, but they are not pertinent to research carried out in this work.

### 2.2.2 SiAlON Behavioral Diagrams

Oxynitride phase diagrams such as those in the SiAlON system do not represent true thermodynamic equilibrium, but instead represent the kinetic limited behavior due to various processing parameters such as particle size and dispersion.[48; 57] Thus, the phase diagrams ignore minor constituent phases that may be present even in regions designated as a single phase field.[57] Figure 2.5 shows the most used SiAlON system representation where it is depicted as a pseudo-quaternary square, the end members are $Si_3N_4$, AlN, $SiO_2$, and $Al_2O_3$, and each ion maintains their normal accepted valency.[48; 58] In this representation, the system does not keep a constant molar mass (i.e. 1 mole), but instead it maintains a constant charge of 12+ and 12- (assuming 1 mol of $Si_3N_4$) so that a square diagram forms. From left to right, $Si^{4+}$ ions are replaced by $Al^{3+}$ ions. Similarly, from bottom to top, $N^{3-}$ ions are replaced by $O^{2-}$ ions. Hence, the diagram assumes 1 mole of $Si_3N_4$ and the other end members are 4 moles of AlN ($Al_4N_4$), 2 moles of $Al_2O_3$ ($Al_4O_6$), 3 moles of $SiO_2$ ($Si_3O_6$) so that the sum total charge is 12+ and 12- at every point. Conversion between molar and equivalence quantities can be done by the follow relationships:[48]

$$\frac{3[Al]}{4[Si]+3[Al]} \quad \text{and} \quad \frac{2[O]}{3[N]+2[O]} \qquad \text{eq: 2.2}$$

where terms in brackets represent molar concentrations of the ions with respect to each other and the coefficient in front is the charge of the ion. For instance, the composition in the middle of the diagram is $Si_{1.5}Al_2O_3N_2$ and $[Al] = \frac{2}{(1.5+2)}$.

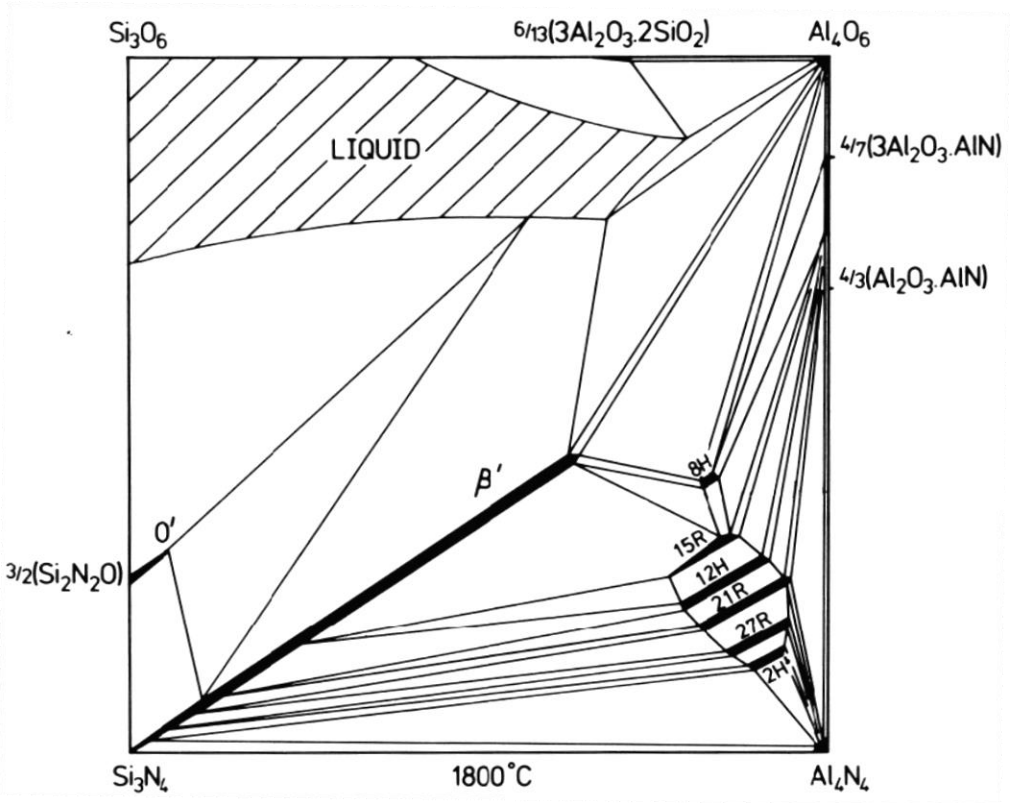


**Figure 2.5 – SiAlON system phase diagram. The x and y axis represent equivalence instead of molar concentrations.[58]**

The R-SiAlON systems are represented in a similar manner to the quaternary diagram. Using The SiAlON diagram as the base, a Janecke prism is constructed by extending the R element above the diagram to form a triangular prism where end members are oxide and nitride compounds and all ions maintain their normal accepted valency. A molar composition can be converted into terms of equivalents using eq. 2.2 and similar relationships on the $R_xN_y$-$R_xO_y$-$Si_3N_4$-$SiO_2$ and $R_xN_y$-$R_xO_y$-AlN-$Al_2O_3$ rectangular faces. The compositional point on the diagram is found by the line intersections drawn from the points on each prism face to the join on the opposite side of the phase diagram, similar to normal ternary phase diagrams. Figure 2.6 shows the Y-SiAlON system phase diagram at 1800 °C by combining data from Jack, Sun *et. al.*, Zhijian and Nygren, Thompson *et. al.*, Huang and Chen, and Ekstrom *et. al.*[48; 53; 55; 56; 59-61]

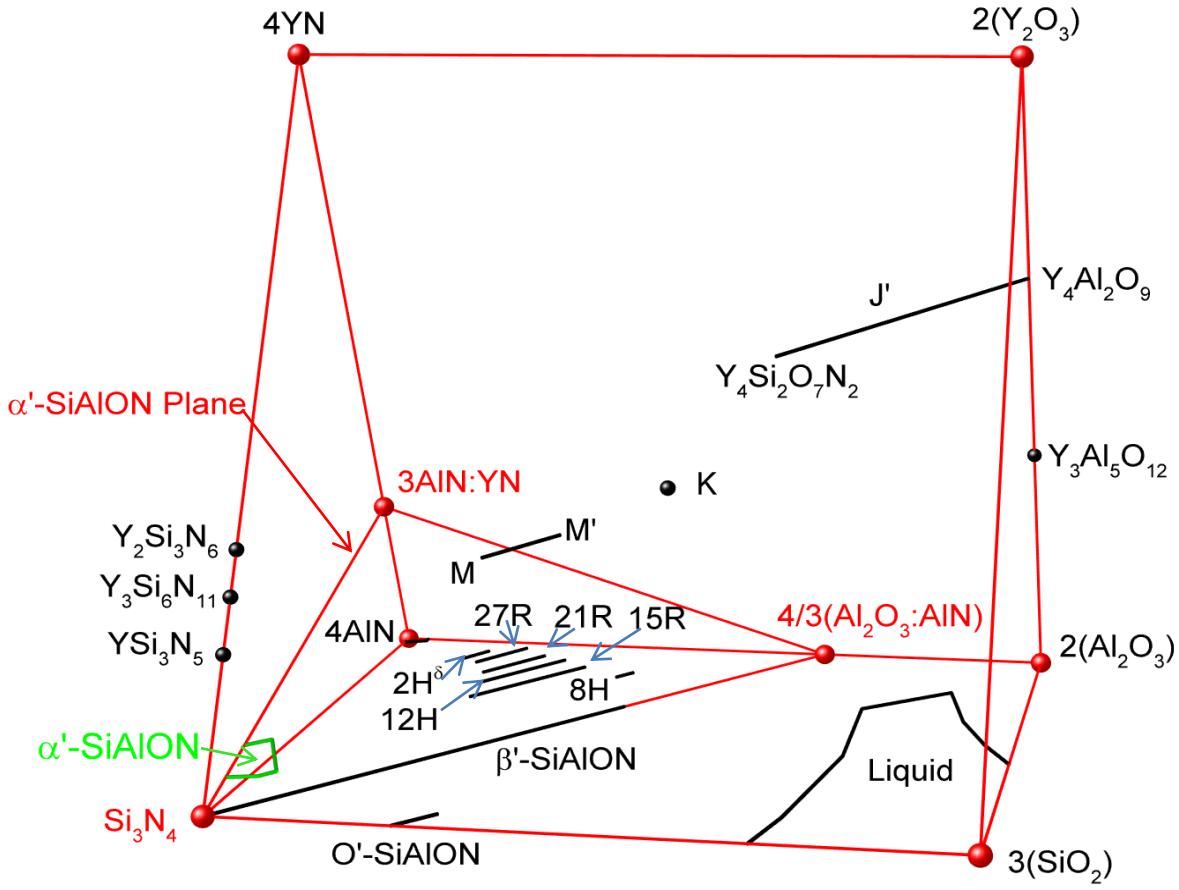


**Figure 2.6 – Y-SiAlON phase diagram at 1800 °C.**[48; 53; 55; 56; 59-61]

The α'-SiAlON phase field is a small region very close to the $Si_3N_4$ corner. Even though the phase field should be a volume with a finite width, researchers assume that α'-SiAlON is a planar slice based on the α'-SiAlON plane's composition formula. Sun *et. al.* determined that the Y-α'-SiAlON solubility limits ranged from m = 1 to m = 2.4 and n = 0 to n = 1.7 based on the compositions he used.[59] However, Shen and Nygren showed that the nominal composition range of "single phase" α'-SiAlON ceramics is larger than that of the actual α'-SiAlON crystal structure. Thus, the solubility limits are the lower limits that were stated in the previous section (see 2.2.1). Figure 2.7 shows the Y-α'-SiAlON combining the results from both Sun and Shen. The area enclosed in the dotted blue line is the work by Sun *et. al.* while the solid green line shows the actual solubility limits determined by Shen *et. al.*[53; 59]

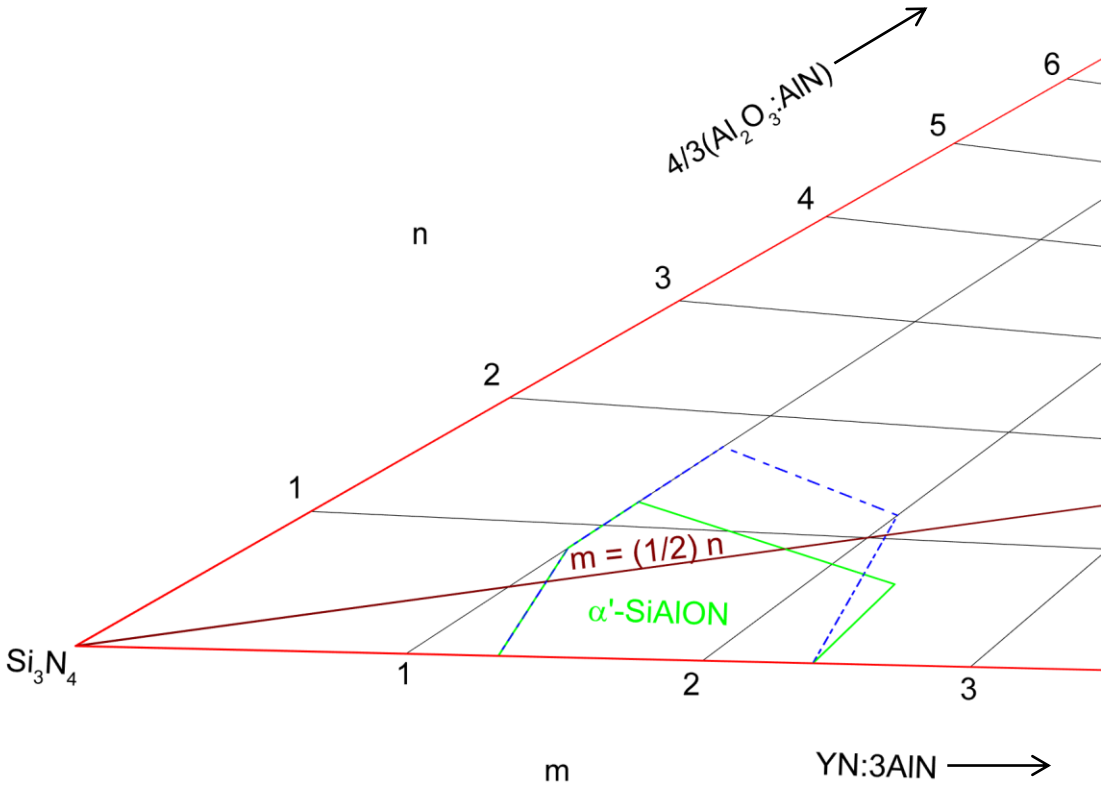


**Figure 2.7 – The α'-SiAlON plane. The solubility limits of α'-SiAlON as determined by Shen and Nygren are shown in the solid green line, while the dotted blue line shows the solubility limits as determined by Sun *et al.*[53; 59]**

The size and range of the α'-SiAlON phase field depends on the solute. The solutes used to stabilize the α'-SiAlON structure are Li, Mg, Ca,Y and most lanthanides (except La, Ce, Pr and Eu). The size of the cation largely determines the α'-SiAlON phase's upper limits (though temperature also affects the upper limits).[57] In general, as the cation size decreases, there is an increase in the overall solubility range, where Nd has the lowest and Ca has the highest.[57] Also, the stability of α'-SiAlON appears to increase as the cation size decreases. Less stable cations tend to form more glass phase during α'-SiAlON processing which can affect their final microstructure as discussed in the section 2.2.3.2.

### 2.2.3 Processing of α'-SiAlON

#### 2.2.3.1 Reaction Hot Pressing and Densification

Due to thermal decomposition of $Si_3N_4$ before melting, $Si_3N_4$ ceramics cannot be processed through a melt growth process. Thus, most $Si_3N_4$ based bulk ceramics are processed using powder processing techniques and sintering using a mixture of oxide and nitride powders. Y- α'-SiAlON ceramics are generally made using α-$Si_3N_4$, AlN, $Al_2O_3$ and $Y_2O_3$ powders which limits their composition to the oxygen rich area (above the n = 1/2m line) of Figure 2.6. Though compositions in the nitrogen rich area have been made, the relatively low cost of fine high purity oxide powders and the ease of microstructural control has led to most research focus in the oxygen rich region.[62; 63]

α'-SiAlON formation occurs via a solution-reprecipitation mechanism from an oxynitride melt similar to that of β'-SiAlON.[64] Due to the low diffusion rate of nitrogen, it is likely that all solid solution SiAlON phases form through this mechanism. Hwang and Chen demonstrated that α'-SiAlON precipitation always occurs via heterogeneous nucleation on α-$Si_3N_4$.[65] Figure 2.8 shows a TEM micrograph of the core shell structure of an α'-SiAlON grain.[66]

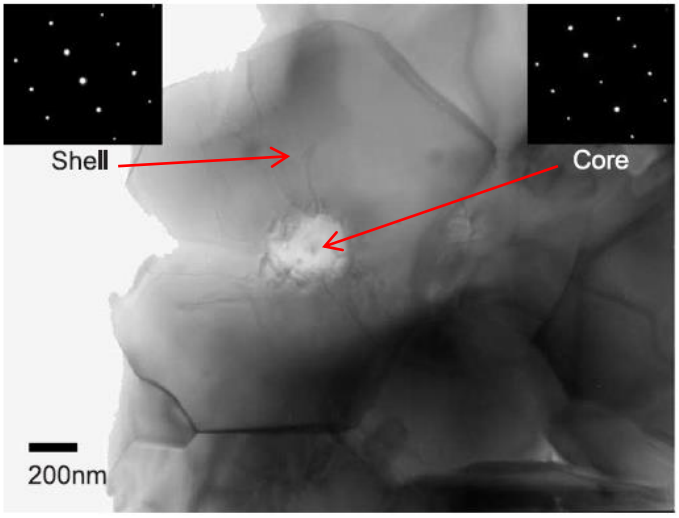


**Figure 2.8 – Bright field TEM image showing the core-shell structure of α'-SiAlON. The α-$Si_3N_4$ core is the brighter region in the middle of the grain. TEM diffraction patterns are shown as insets with B=[-12-13][66]**

After nucleation occurs, changes in the local liquid phase's composition result in a composition gradient across α'-SiAlON grains. Both Sheu and Miyazaki *et. al.* showed the concentration gradient of stabilizing cations in α'-SiAlON grains.[66; 67] Sheu utilized XRD analysis to show that α'-SiAlON formation started at lower angles (higher d-spacings) and shifted to higher angles (lower d-spacings).[67] α'-SiAlON's lattice parameters increase above α-$Si_3N_4$ as the Y/Al content (i.e. the m value) increases and as the oxygen content increases (i.e. the n value).[53] Miyazaki *et. al.* confirmed this finding in the Yb-α'-SiAlON system using scanning tunneling electron microscopy (STEM) and a line scan using energy dispersive spectroscopy (EDS).[66] They attributed this behavior to the changes in the oxynitride melt's composition during sintering.[66] Sheu and Miyazaki *et. al.*'s findings are surprising because heterogeneous nucleation should favor the composition with a lattice parameter closest to that of α-$Si_3N_4$ due to the lower strain energy. Since this is not the case, the strain energy difference between high and low Y/Al compositions must be small. In Y-α'-SiAlON's, the *a* and *c* lattice parameters do not increase beyond approximately 0.2% and 2.3%, respectively, above α-$Si_3N_4$

which is in agreement.[53] Based on the above, the oxynitride melt's local composition around an α-$Si_3N_4$ particle determines the composition and growth of α'-SiAlON.

The liquid phase composition changes according to the reaction sequence between the oxide and nitride particles. The first liquid to form is the specific M-SiAlON system's eutectic oxide ($SiO_2 – Al_2O_3 – M_xO_y$) at or below the eutectic temperature depending on impurities.[57; 68; 69] The nitride particles that react first with the eutectic oxide should primarily dictate the compositional shifts in the liquid melt and the reaction path for α'-SiAlON formation. Many papers report phase evolution sequences during the sintering of α'-SiAlON, but very few studies attempt to understand the fundamental mechanism governing the reaction sequence based on this logic. In general, studies agree that the reaction pathway occurs through 3 general steps: formation of a eutectic oxide and oxynitride melt, precipitation of an intermediate phase and precipitation of the α'-SiAlON phase.

Studies by Hwang *et. al.* and Chen *et. al.* are the only to attempt to understand α'-SiAlON formation based on the liquid phase wetting behavior. They concluded that the eutectic oxide wetting behavior on the nitride powders of the specific M-SiAlON system determined the reaction sequence and densification of α'-SiAlON ceramics.[70-72] Hwang's work is the first study to show this relationship between the nitride powder wetting and the specific intermediate phase that forms in α'-SiAlON ceramic processing. In the Y-α'-SiAlON system, Hwang showed that the eutectic oxide melt preferentially wets AlN with respect to $Si_3N_4$. Figure 2.9 shows the eutectic oxide wetting angle on $Si_3N_4$ and AlN substrates as the temperature changes. The eutectic oxide completely reacted with the AlN substrate by 1500 °C, but not the $Si_3N_4$ substrate. The reaction zone between the melt and the AlN substrate contained YAG, 15R, and $\beta_{60}$-SiAlON which were the same intermediate products found during interruption runs of α'- or α'/β'-

SiAlON compositions. Thus, there may be a correlation between the eutectic oxide's preferential wetting of the nitride powders and the specific intermediate phase that forms.

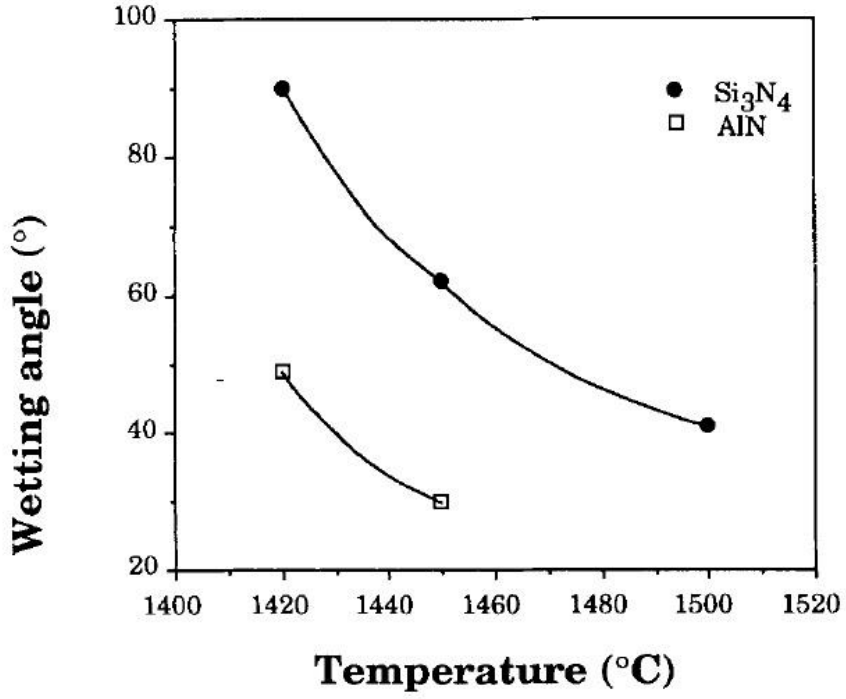


**Figure 2.9 – Wetting angle variation vs temperature of the $Y_2O_3$-$Al_2O_3$-$SiO_2$ eutectic oxide on AlN and $Si_3N_4$ substrates. Only two data points are shown for the AlN substrate because the melt completely reacted with substrate at the final measuring temperature.[70]**

Extending the study Hwang performed, Menon compared the acid-base chemistry of multiple M-SiAlON systems with the nitride wetting characteristics, intermediate phase formation and $pH_o$ of the respective stabilizing cation's oxide.[71] Table 2.2 gives a summary of the systems studied by Menon.

| Stabilizing Oxide | Preferential Nitride Wetting | Reaction Zone Phase / Intermediate Phase | $pH_o$ |
|---|---|---|---|
| $Li_2O$ | $Si_3N_4$ | O'-SiAlON | 11.76 |
| CaO | $Si_3N_4$ | O'-SiAlON | 10.67 |
| MgO | AlN | $Mg_2Al_4Si_5O_{18}$ | 10.27 |
| $Nd_2O_3$ | $Si_3N_4$ | $Nd_2Si_{3-x}Al_xO_{3+x}N_{4-x}$ (M') | 8.93 |
| $Gd_2O_3$ | $Si_3N_4$ | $Gd_2Si_{3-x}Al_xO_{3+x}N_{4-x}$ (M') | 8.88 |
| $Y_2O_3$ | AlN | β-SiAlON and $Y_3Al_5O_{12}$ | 8.86 |
| $Sm_2O_3$ | $Si_3N_4$ | $Sm_2Si_{3-x}Al_xO_{3+x}N_{4-x}$ (M') | 8.77 |
| $Dy_2O_3$ | AlN | $Dy_2Si_{3-x}Al_xO_{3+x}N_{4-x}$ (M') | 8.75 |
| $Er_2O_3$ | AlN | β-SiAlON and $Er_3Al_5O_{12}$ | 8.72 |
| $Yb_2O_3$ | AlN | β-SiAlON and $Yb_3Al_5O_{12}$ | 8.49 |

**Table 2.2 – Results of study by Menon *et. al*. The table shows a list of stabilizing cations for α'-SiAlON, which raw nitride powder the eutectic oxide in the system preferentially wets, the intermediate phases formed and the point of zero charge ($pH_o$) of each oxide.[71]**

Table 2.2 shows that generally as the basicity of the stabilizing oxide decreases the wetting angle begins to preferentially wet AlN instead of $Si_3N_4$. Menon attributed this trend to the Pearson's principle in acid-base chemistry, i.e. hard acids and soft acids preferentially react with hard bases and soft bases, respectively.[71] Considering that nitrides always have surface oxides, their respective oxides determine their acidity or basicity. Thus, $Si_3N_4$ is more acidic than AlN and each eutectic oxide preferentially wets $Si_3N_4$ or AlN accordingly.[71] Another trend shows that as the basicity changes, there is a relative change in the reactivity between the eutectic and the wetted nitride.[71] Except for $Mg_2Al_4Si_5O_{18}$, the intermediate phases show a decrease in the Si / Al ratio as the basicity decreases due to the decreasing preference for $Si_3N_4$.[71] This trend correlates well with the basicity of the oxides and the preferential wetting of the nitride powders. MgO is in an exception to this trend because even though the eutectic oxide preferentially wets AlN, there is a preferential reaction with $Si_3N_4$.[71]

α'-SiAlON densification studies by Hwang and Menon further demonstrate the importance of the eutectic oxide wetting the nitride powders.[70; 72] Depending on which nitride is wetted or preferentially reacted with, a different densification process is observed. If $Si_3N_4$ is

wetted first like in the more basic oxides of table 2.2, then an immediate shrinkage step occurs upon wetting. If AlN is wetted first, then there is little or no change in the densification. Hwang proposed that this occurs due to liquid phase localization on the small amount of AlN in α'-SiAlON ceramics.[70] Figure 2.10 schematically shows the densification behavior upon wetting $Si_3N_4$ or AlN. The indicated temperatures are characteristic temperatures that correspond to specific observed reactions: $T_1$ is the formation of a eutectic oxide, $T_2$ is the preferential wetting of the nitride powder and potential intermediate phase formation, $T_3$ is the wetting of the other nitride powder, $T_4$ is the dissolution of the intermediate phase and $T_5$ is the precipitation of the final phase. The characteristic temperatures do not necessarily appear sequentially. Depending on the system, different variations of this schematic are possible.

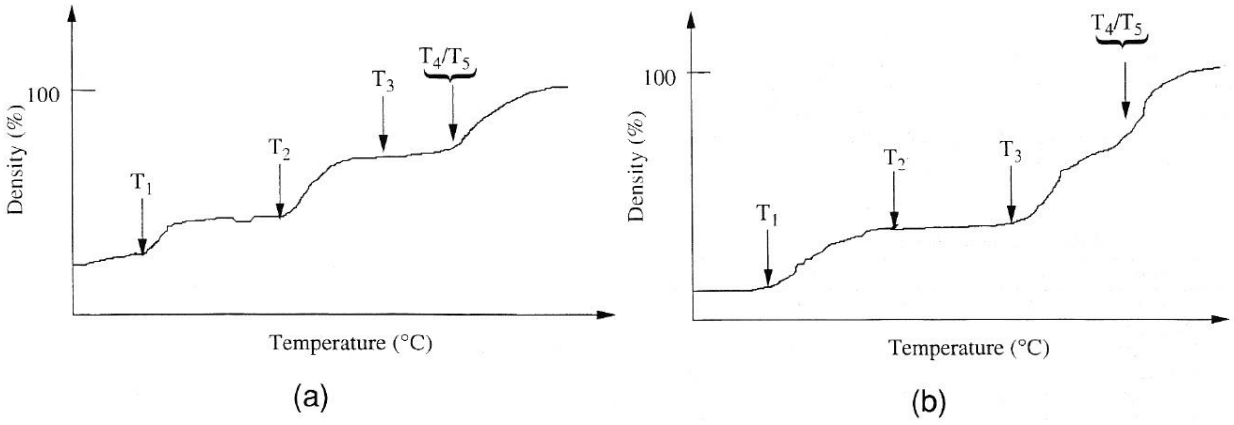


**Figure 2.10 – Reaction densification behavior of α'-SiAlON depending on preferential wetting of (a) $Si_3N_4$ or (b) AlN. Characteristic temperatures presented do not necessarily occur in the order presented, but shrinkage steps after the labeled temperature occur as shown. The characteristic temperatures are as follows: $T_1$ is the formation of a eutectic oxide, $T_2$ is the wetting of the nitride powder and intermediate phase formation, $T_3$ is the wetting of the other nitride powder, $T_4$ is the dissolution of the intermediate phase and $T_5$ is the precipitation of the final phase.[72]**

Hwang and Menon suggested temperature ranges and phase formations for the 3 general reactions that occur (i.e. formation of the ternary eutectic oxide reaction, initial nitride precipitation and secondary nitride precipitation) based on the above principles, the phase

diagrams and the partially filled M-SiAlON system diagrams. Using their results, phase relationships and evolutions reported in the literature, the reaction pathway for Y-α'-SiAlON is:

- 1340 -1350 °C

Eutectic Oxide Formation:
$SiO_2(S) + Al_2O_3(S) + Y_2O_3(S) \rightarrow (Si, Al, O)_x O_y\ (Liquid) + Y_3Al_5O_{12}(S)$

- 1380 – 1550 °C

Initial Nitride Precipitation:
$(Si, Al, O)_x O_y\ (Liquid) + AlN\ (S) + Si_3N_4(S) \rightarrow \beta' - SiAlON\ (S, supersaturated) + Y - \alpha' - SiAlON\ (S, supersaturated) + (Si, Al, Y)_x (O, N)_y\ (Liquid) + AlN(S, residual) + AlN - polytypoid\ (S)$

- 1420 – 1700+ °C

Secondary Nitride Precipitation:
$(Si, Al, Y)_x (O, N)_y\ (Liquid) + AlN\ (S) + Si_3N_4(S) + Y_3Al_5O_{12}(S) + \beta' - SiAlON(S, supersaturated) \rightarrow Y - \alpha' - SiAlON(S) + AlN(S, residual) + AlN - polytypoids\ (S)$

This reaction sequence is primarily based on the work by Hwang, but it has several differences. The first difference is the α'-SiAlON precipitation during the initial nitride precipitation reaction. Formation of α'-SiAlON has been shown to occur at lower temperatures than the 1470 °C determined by Hwang.[73] Based on the wetting and preferential reaction, the liquid phase is supersaturated by Al during the initial nitride precipitation. As Y-α'-SiAlON nucleates, it initially has a much higher Y / Al content than the nominal composition as discussed earlier. Thus, the initial α'-SiAlON nucleation must occur close to the formation of β-SiAlON while the liquid phase is still saturated with Al and Y for the observed composition gradient to occur. The second difference is that only α'-SiAlON and AlN-polytypoids remain after the reaction. During the secondary nitride precipitation, most remaining components nominally dissolve into the liquid and α'-SiAlON phase formation continues. Though the α-$Si_3N_4$ → β-$Si_3N_4$ transformation is irreversible, the α'-SiAlON → β'-SiAlON is fully reversible. Thus, in nominally single phase

α'-SiAlON, the final reaction should also include any β'-SiAlON that formed previously. AlN-polytypoids are commonly found as a minor secondary phase constituent in α'-SiAlON ceramics.[60; 62; 74; 75] AlN-polytypoids do not dissolve because they are compatible with α'-SiAlON.[60] As discussed in Chapter 3, their formation is dictated by the presence of heterogeneous nuclei (residual AlN particles) and is not likely to occur during cooling. The exact reaction temperature range is unknown, but it is assumed that the reaction can occur during either the initial or secondary nitride precipitation reactions because of the presence of large AlN particles and the high Al/Si ratio of the liquid composition near the particles during dissolution.

The reaction sequence presented above should be observed with caution. The preferential wetting is based on the assumption that the β-$Si_3N_4$ substrates have the same wetting characteristics as α-$Si_3N_4$. However, the difference in the wetting angle between the liquid phase and α-$Si_3N_4$ or β-$Si_3N_4$ should be small enough to ignore. Also, various other intermediate phases such as J', M', and AlN-polytypoids are reported to form during Y-α'-SiAlON sintering.[57; 60; 76] No study has presented a reason for the discrepancies in the M-α'-SiAlON systems' phase evolution within the same cation system. Cao's studies show that the small compositional differences may explain the discrepancies, but the work by Hwang and Chen and Menon and Chen show only YAG forming as the intermediate phase in various Y-SiAlON compositions on the α'-SiAlON plane.[57; 70; 71; 73] The Y-α'-SiAlON system may still provide some explanation. Table 2.2 shows $Y_2O_3$'s $pH_o$ is between $Gd_2O_3$ and $Sm_2O_3$ which preferentially wet $Si_3N_4$ and form M' as an intermediate phase, yet the $Y_2O_3$-$SiO_2$-$Al_2O_3$ oxide system still preferentially wets AlN. $Y_2O_3$ may act as an intermediate compound that can preferentially wet or react with either nitride powder depending on if other factors change the surface energies between the solid, liquid and gas phases such as impurities, powder

morphology, powder mixing, and atmosphere environment during sintering. This is in agreement with a study by Rosenflanz and Chen as they concluded $Y_2O_3$ wetted $Si_3N_4$ first instead of AlN to form M' as an intermediate phase.[77] Even if the discrepancies are not yet explained, the principle that the nitride powder wetting determines the overall reaction pathway is still valid.

#### 2.2.3.2 α'-SiAlON Microstructure Control

Until recently, α'-SiAlON ceramic microstructures were considered to always have a fine-grain equiaxed microstructure.[57] α'-SiAlON ceramics have a higher hardness than β'-SiAlON, but the equiaxed microstructure gives them a lower toughness. Also, α'-SiAlON ceramics ideally have no residual amorphous phase, but kinetic and processing limitations always create residual amorphous phase which decrease the high temperature strength.[57] Thus, researchers have focused on increasing the toughness and/or decreasing the amorphous phase content by making various composites such as α'-β', α'-TiN, α'-$MoSi_2$ and α'-SiC.[64; 78-82] Other work has tried to reduce the grain boundary content by crystallizing the glassy phase.[82; 83]

Recently, researchers have focused on pure α'-SiAlON microstructure control. Rosenflanz and Shuba *et. al.* both studied the effect of introducing excess $Si_3N_4$ and / or AlN to shift the nominal composition away from the α'-SiAlON plane.[84; 85] Rosenflanz compared stoichiometric α'-SiAlON samples with samples containing an excess of $Si_3N_4$ and AlN (up to 30 wt% of a predetermined ratio).[84] By adding excess $Si_3N_4$ and AlN, Rosenflanz moved the nominal composition of the ceramics below the plane and effectively removed all the glassy phase from the grain boundaries and triple junctions based on BSEM images.[84] Considering Le Chatelier's principle, increasing the nitride content should increase the driving force for the

formation of α'-SiAlON.[85] Shuba *et. al.* used this principle to determine that excess AlN is more effective at removing the glass phase content than $Si_3N_4$ because shifts in AlN cause a greater shift in the Al content than shifts in $Si_3N_4$ can for Si.[85]

More novel research by Rosenflanz and Chen demonstrates that the microstructure of α'-SiAlON is controlled through its nucleation and growth.[86] Previous studies showed that an elongated grain microstructure could be achieved by using high-(m,n) compositions of various cations or cation combinations.[87-89] Under these conditions, a relatively large amount of low viscosity liquid phase forms which provides extra room for growth.[62] These conditions are undesirable because a large amount of glassy phase results in poor mechanical properties.[62] Rosenflanz *et. al.* systematically controlled the nucleation and growth of α'-SiAlON by substituting the α-$Si_3N_4$ powder with β-$Si_3N_4$ and by using two step hot pressing to achieve self-reinforced microstructures.[86] Because β-$Si_3N_4$ is more stable than α-$Si_3N_4$, its use in α'-SiAlON processing results in slower phase formation. Also, α- and β-$Si_3N_4$ powders are not pure; each containing some amount of the other. The small amount of α in the β-$Si_3N_4$ acts as nucleation sites and α'-SiAlON can grow without risk of early impingement.[86] In cases where the driving force for α'-SiAlON is too high (such as in Y and Yb), β-$Si_3N_4$ conversion occurs too quickly and 2 step hot pressing is required to create elongated α'-SiAlON grains.[86] The self-reinforced microstructure in all the ceramics exhibited the same hardness as in equiaxed microstructures, but with a toughness comparable to β-$Si_3N_4$.[86]

Another means of controlling the nucleation and growth of α'-SiAlON is through seeding. Though α'-SiAlON's formation occurs through heterogeneous nucleation on α-$Si_3N_4$, the use of α'-SiAlON seed particles can control the nucleation. The seeds must be stable and have a close lattice parameters (+ or – 15%) to allow epitaxial nucleation. Because α-$Si_3N_4$ is a

reactant in α'-SiAlON's formation, the only particles that can be considered to be stable are the larger particles because the larger particles are able to survive the dissolution process until nucleation becomes favorable. The same argument can be applied to α'-SiAlON seed crystals .[90] Zenotchkine *et. al.* used α'-SiAlON seed crystals at various concentrations to control the amount of elongated grains in Y-α'-SiAlON.[90] Their work reaffirms that the seed number density generally controls the final morphology.[62; 90]

## 2.3 References


[1]R. E. Hummel, "Electronic Properties of Materials," Third ed. Springer, (2001).

[2]L. Liu, F. Ye, S. Zhang, B. Peng, W. Luo, Z. Zhang, and Y. Zhou, "Light Transmittance in α-SiAlON Ceramics: Effects of Composition, Microstructure, and Refractive Index Anisotropy," *J. Euro. Ceram. Soc.*, **32,** 2487-94 (2012).

[3]M. Bass (editor), "Handbook of Optics: Optical Properties of Materials, Nonlinear Optics, Quantum Optics," Third ed. **Vol. IV**. McGraw Hill: New York, (2010).

[4]CDGM Glass Co., "CDGM Optical Glass Products Database," 2006

[5]I. H. Malitson, "Interspecimen Comparison of the Refractive Index of Fused Silica," *J. Opt. Soc. Am.*, **55,** [10] 1205-09 (1965).

[6]T. Baak, "Silicon Oxynitride; a Material for GRIN Optics," *Appl. Optics*, **21,** [6] 1069-72 (1982).

[7]S. Kochawattana, A. Stevenson, S.-H. Lee, M. Ramirez, V. Gopalan, J. Dumm, V. K. Castillo, G. J. Quarles, and G. L. Messing, "Sintering and Grain Growth in $SiO_2$ doped Nd:YAG," *J. Euro. Ceram. Soc.*, **28,** 1527-34 (2008).

[8]Y.-Q. Li, N. Hirosaki, R.-J. Xie, J. Li, T. Takeda, Y. Yamamoto, and M. Mitomo, "Structural and Photoluminescence Properties of $Ce^{3+}$ - and $Tb^{3+}$ - Activated Lu-α-SiAlON," *J. Am. Ceram. Soc.*, **92,** [11] 2738-44 (2009).

[9]Y.-N. Xu and W. Y. Ching, "Electronic Structure and Optical Properties of α and β Phases of Silicon Nitride, Silicon Oxynitride, and with Comparison to Silicon Dioxide," *Phys. Rev. B*, **51,** [24] 17379-89 (1995).

[10]Z. Shen, M. Nygren and U. Halenius, "Absorption Spectra of Rare-Earth-Doped α-SiAlON Ceramics," *J. Mater. Sci. Lett.*, **16,** 263-66 (1997).

[11]A. J. Stevenson, B. C. Bittel, C. G. Leh, X. Li, E. C. Dickey, P. M. Lenahan, and G. L. Messing, "Color Center Formation in Vacuum Sintered $Nd_{3x}Y_{3-3x}Al_5O_{12}$ Transparent Ceramics," *Appl. Phys. Lett.*, **98,** [051906] 1-3 (2011).

[12]M. Herrmann and O. Goeb, "Colour of Gas-Pressure-Sintered Silicon Nitride Ceramics Part I. Experimental Data," *J. Euro. Ceram. Soc.*, **21,** 303-14 (2001).

[13]M. Herrmann and O. Goeb, "Colour of Gas-Pressure-Sintered Silicon Nitride Ceramics Part II. Thermodynamic Considerations," *J. Euro. Ceram. Soc.*, **21,** 461-69 (2001).

[14]M. I. Jones, H. Hyuga, K. Hirao, and Y. Yamauchi, "Highly Transparent Lu-α-SiAlON," *J. Am. Ceram. Soc.*, **87,** [4] 714-16 (2004).

[15]G. J. Peelen and R. Metselaar, "Light Scattering by Pores in Polycrystalline Materials-Transmission Properties of Alumina," *J. Appl. Phys.*, **45,** [1] 216-20 (1974).
[16]A. Ikesue and Y. L. Aung, "Ceramic Laser Materials," *Nature Photonics,* **2,** 721-27 (2008).
[17]A. Ikesue and I. Furusato, "Influence of Pore Volume on Laser Performance of Nd : YAG Ceramics," *J. Am. Ceram. Soc.,* **78,** [1] 225-28 (1998).
[18]D. N. Coon and T. E. Doyle, "Refractive Indices of Glasses in the Y-Al-Si-O-N System," *J. Non.-Cryst. Solids,* **108,** [180-186] (1989).
[19]W. Redington, M. Redington, S. Hampshire, and M. Serantoni, "Properties of Some High Al Content Glasses in Various Lanthanide-Si-Al-O-N Systems," *J. Non.-Cryst. Solids,* **316,** 74-81 (2003).
[20]R. A. L. Drew, S. Hampshire and K. H. Jack, "The Preparation and Properties of Oxynitride Glasses," pp. 323-30. Progress in Nitrogen Ceramics**.** Edited by F. L. Riley. Martinus Nijhoff, 1983.
[21]M. I. Jones, H. Hyuga and K. Hirao, "Optical and Mechanical Properties of α/β Composite SiAlONs," *J. Am. Ceram. Soc.,* **86,** [3] 520-22 (2003).
[22]Y. Xiong, Z. Y. Fu, H. Wang, Y. C. Wang, J. Y. Zhang, and Q. J. Zhang, "Microstructure and Properties of Translucent Mg-SiAlON Ceramics Prepared by Spark Plasma Sintering," *Mater. Sci. Eng., A,* **488,** 475-81 (2008).
[23]J. Xue, Q. Liu and L. Gui, "Lower-Temperature Hot-Pressed Dy-α-Sialon Ceramics with a LiF Additive," *J. Am. Ceram. Soc.,* **90,** [5] 1623-25 (2007).
[24]J. Pastrnak and L. Roskovcova, "Refraction Index Measurements on AlN Single Crystals," *Phys. Stat. Sol.,* **14,** K5-K8 (1966).
[25]R. Apetz and M. P. B. v. Bruggen, "Transparent Alumina: A Light-Scattering Model," *J. Am. Ceram. Soc.,* **86,** [3480-486] (2003).
[26]A. Ikesue and K. Yoshida, "Scattering in Polycrystalline Nd:YAG Lasers," *J. Am. Ceram. Soc.,* **81,** [8] 2194-96 (1998).
[27]A. L. Dalisa and R. J. Seymour, "Convolution Scattering Model for Ferroelectric Ceramics and Other Display Media," *Proc. IEEE,* **61,** [7] 981-91 (1973).
[28]R. L. Coble, U.S. Patent No. 3026210 (March 20, 1962)
[29]R. C. Anderson, U.S. Patent No. 354987 (8 December 1970)
[30]A. Krell, P. Blank, H. Ma, T. Hutzler, R. Apetz, and M. P. B. Bruggen, "Transparent Sintered Corundum with High Hardness and Strength," *J. Am. Ceram. Soc.,* **86,** [1] 12-18 (2003).
[31]Y. W. Cho and J. A. Charles, "Synthesis of Nitrogen Ceramic Powders by Carbothermal Reduction and Nitridation: Part 1 Silicon Nitride," *Mat. Sci. Tech.,* **7,** 289-98 (1991).
[32]D. R. Messier, F. L. Riley and R. J. Brook, "The α/β Silicon Nitride Phase Transformation," *J. Mater. Sci.,* **13,** 1199-206 (1978).
[33]A. Zerr, G. Miehe, G. Serghiou, M. Schwarz, E. Kroke, R. Riedel, H. FueB, P. Kroll, and R. Boehler, "Synthesis of Cubic Silicon Nitride," *letters to Nature,* **400,** 340-42 (1999).
[34]C.-M. Wang, X. Q. Pan and M. Ruhle, "Review: Silicon Nitride Crystal Structure and Observations of Lattice Defects," *J. Mater. Sci.,* **31,** 5281-94 (1996).
[35]R. Grun, "The Crystal Structure of β-$Si_3N_4$; Structural and Stability Considerations Between α and β-$Si_3N_4$," *Acta. Cryst.,* **B35,** 800-04 (1979).
[36]W. Y. Ching, L. Quyang and J. D. Gale, "Full AB Initio Geometry Optimization of All Known Crystalline Phases of $Si_3N_4$," *Phys. Rev. B,* **61,** [13] 8697-700 (2000).
[37]Y. Bando, "Weak Asymmetry in β-Si3N4 as Revealed by Convergent-Beam Electron Diffraction," *Acta. Cryst.,* **B39,** 185-89 (1983).

[38]R. Belkada and M. Kohyama, "Relative Stability of $P6_3/m$ and $P6_3$ Structures of β-Si3N4," *Phys. Rev. B,* **65,** [092104] 1-4 (2002).
[39]D. Hardie and K. H. Jack, "Crystal Structures of Silicon Nitride," *Letters to Nature,* **180,** 332-33 (1957).
[40]D. d. Boulay, N. Ishizawa, T. Atake, V. Strelstov, K. Furuya, and F. Munakata, "Synchrotron X-ray and AB Initio Studies of β-$Si_3N_4$," *Acta Crystal.,* **B60,** 388-405 (2004).
[41]P. Grieveson, K. H. Jack and S. Wilde, "Special Ceramics," pp. 237. **Vol. 4.** Edited by P. Popper. George Faulkner Press, Manchester, 1968.
[42]S. Wilde, P. Grieveson and K. H. Jack, "Special Ceramics," pp. 385. Edited by P. Popper. George Faulkner Press, Manchester, 1972.
[43]A. J. Edwards, D. P. Elias, M. W. Lindley, A. Atkinson, and A. J. Moulson, "Oxygen Content of Reaction-Bonded α-$Si_3N_4$," *J. Mater. Sci.,* **9,** 516-17 (1974).
[44]K. Kato, Z. Inoue, K. Kijima, I. Kawada, and H. Tanaka, "Structural Approach to the Problem of Oxygen Content in Alpha Silicon Nitride," *J. Am. Ceram. Soc.,* **58,** [3-4] 90-91 (1975).
[45]K. Kijima, K. Kato, Z. Inoue, and H. Tanaka, "Oxygen Content of α-Si3N4 Single Crystals," *J. Mater. Sci.,* **10,** 362-63 (1975).
[46]K. H. Jack, "The Characterization of α'-SiAlONs and the α-β Relationships in SiAlONs and Silicon Nitride," pp. 45-60. Progress in Nitrogen Ceramics**.** Edited by F. L. Riley. Martinus Nijhoff, 1983.
[47]S. Hampshire, H. K. Park, D. P. Thompson, and K. H. Jack, "α′-SiAlON Ceramics," *Letters to Nature,* **274,** 880-82 (1978).
[48]K. H. Jack, "Review: Sialons and Related Nitrogen Ceramics," *J. Mater. sci.,* **11,** 1135-58 (1976).
[49]O. Borgen and H. M. Seip, "The Crystal Structure of β-$Si_3N_4$," *Acta Chem. Scand.,* **15,** [8] 1789 (1961).
[50]J. J. melendez-Martinez and A. Dominguez-Rodriguez, "Creep of Silicon Nitride," *Progress in Materials Science,* **49,** 19-107 (2004).
[51]Y. Oyama and O. Kamiga, "Solid Solubility of Some Oxides in $Si_3N_4$," *Jpn. J. Appl. Phys,* **10,** 1637 (1971).
[52]D. P. Thompson, "The Crystal Chemistry of Nitrogen Ceramics," *Mater. Sci. Forum,* **47,** 21-41 (1989).
[53]Z. Shen and M. Nygren, "On the Extension of the α-SiAlON Phase Area in Yttrium and Rare-Earth Doped Systems," *J. Euro. Ceram. Soc.,* **17,** 1639-45 (1997).
[54]Y. Yan, m. terauchi and M. Yanaka, "Structures of Polytypoids in AlN Crystals Containing Oxygen," *Philosophical Magazine A,* **77,** [4] 1027-40 (1998).
[55]D. P. Thompson, K. Liddell, Z.-B. YU, and L. Gao, "J-Phase Structure in the Y-Si-Al-O-N System," *Key Eng. Mater.,* **264-268,** 1013-16 (2004).
[56]Z.-K. Huang and I.-W. Chen, "Rare-Earth Melilite Solid Solution and its Phase Relations with Neighboring Phases," *J. Am. Ceram. Soc.,* **79,** [8] 2091-97 (1996).
[57]G. Z. Cao and R. Metselaar, "α'-SiAlON Ceramics: A Review," *Chem. Mater.,* **3,** [2] 242-52 (1991).
[58]K. H. Jack, "SiAlONs: A Study in Materials Developments," pp. 1-30. Non-Oxide Technical and Engineering Ceramics**.** Edited by S. Hampshire. Elsevier Applied Science, New York, NY, 1986.
[59]W.-Y. Sun, T.-Y. Tien and T.-S. Yen, "Solubility Limits of α'-SiAlON Solid Solutions in the System Si,Al,Y/N,O," *J. Am. Ceram. Soc.,* **74,** [10] 2547-50 (1991).

[60]W.-Y. Sun, T.-Y. Tien and T.-S. Yen, "Subsolidus Phase Relationships in Part of the System Si,Al,Y,/N,O: The System $Si_3N_4$-AlN-YN-$Al_2O_3$-$Y_2O_3$," *J. Am. Ceram. Soc.,* **74,** [11] 2753-58 (1991).
[61]T. C. Ekstrom, K. J. D. MacKenzie, M. J. Ryan, I. W. M. Brown, and G. V. White, "Phases Occurring in the $Si_3N_4$-YN System," *J. Mater. Chem.,* **7,** [3] 505-09 (1997).
[62]I.-W. Chen, R. Shuba and M. Y. Zenotchkine, "Development of Tough Alpha-SiAlON," *Key Eng. Mater.,* **237,** 65-78 (2003).
[63]Y. Cai, "Synthesis and Characterization of Nitrogen-Rich Calcium α-Sialon Ceramics"; Thesis. Stockholm University, 2009
[64]T. Ekstrom and M. Nygren, "SiAlON Ceramics," *J. Am. Ceram. Soc.,* **75,** [2] 259-76 (1992).
[65]S.-L. Hwang and I.-W. Chen, "Nucleation and Growth of α'-SiAlON on α-$Si_3N_4$," *J. Am. Ceram. Soc.,* **77,** [7] 1711-18 (1994).
[66]H. Miyazaki, M. I. Jones and K. Hirao, "Concentration Gradient of Solute Ions within α-SiAlON Grains," *Mater. Lett.,* **59,** 44-47 (2005).
[67]T.-S. Sheu, "Microstructure and Mechanical Properties of the In Situ β-$Si_3N_4$/α'-SiAlON Composite," *J. Am. Ceram. Soc.,* **77,** [9] 2345-53 (1994).
[68]C. O'Meara, G. L. Dunlop and R. Pompe, "Phase Relationships in the System $SiO_2$-$Y_2O_3$-$Al_2O_3$," pp. 265-70. in High Tech Ceramics, **Vol. 1.** Edited by P. Vincenzini. Elsevier, Amsterdam, 1987.
[69]S. Hampshire and K. H. Jack, "Densification and Transformation Mechanisms in Nitrogen Ceramics," pp. 225-30. Progress in Nitrogen Ceramics**.** Edited by F. L. Riley. Martinus Nijhoff, 1983.
[70]S.-L. Hwang and I.-W. Chen, "Reaction Hot Pressing of α'- and β'-SiAlON Ceramics," *J. Am. Ceram. Soc.,* **77,** [1] 165-71 (1994).
[71]M. Menon and I.-W. Chen, "Reaction Densification of α'-SiAlON: I, Wetting Behavior and Acid-Base Reactions," *J. Am. Ceram. Soc.,* **78,** [3] 545-52 (1995).
[72]M. Menon and I.-W. Chen, "Reaction Densification of α'-SiAlON: II, Densification Behavior," *J. Am. Ceram. Soc.,* **78,** [3] 553-59 (1995).
[73]G. Z. Cao, R. Metselaar and G. Ziegler, "Formation and Densification of α'-SiAlON Ceramics,*"* pp. 1285-93 in Proceeding of the 7th Internation Meeting on Modern Ceramics Technologies. Edited by P. Vincenzini.
[74]Z. Yang, H. Wang, X. Min, W. Wang, Z. Fu, S. W. Lee, and K. Niihara, "Optical and Mechanical Porperties of Mg-doped SiAlON Composite with $La_2O_3$ as Additive," *J. Euro. Ceram. Soc.,* **32,** 931-35 (2012).
[75]Z. Shen, H. Peng and M. Nygren, "Formation of In-Situ Reinforced Microstructure in α-SiAlON Ceramics I: Stoichiometric Oxygen-Rich Compostiions," *J. Mater. Res.,* **17,** [2] 336-42 (2002).
[76]W. Y. Sun, F. Y. Wu and D. S. Yan, "Studies of the Formation of α' and α'-β' SiAlON," *Mater. Lett.,* **6,** [1-2] 11-15 (1987).
[77]A. Rosenflanz and I.-W. Chen, "Kinetics of Phase Transformations in SiAlON Ceramics: Effects of Cation Size, Composition and Temperature," *J. Euro. Ceram. Soc.,* **19,** 2325-35 (1999).
[78]L. O. Nordberg and T. Ekstrom, "Simultaneously $MoSi_2$ and SiC-reinforced α-SiAlON composites," *J. Mater. Res. Lett.,* **16,** 917-20 (1997).
[79]V. A. Izhevskiy, L. A. Genova, J. C. Bressiani, and F. Aldinger, "Progress in SiAlON Ceramics," *J. Euro. Ceram. Soc.,* **20,** 2275-95 (2000).

[80]F. Xu, S. Wen, L.-O. Nordberg, and T. Ekstrom, "TEM Study of Y-doped α'-SiAlON Composite with 10 vol% TiN Particulates," *Mater. Lett.*, **34,** 248-52 (1998).
[81]T. Ekstrom and J. Persson, "Hot Hardness Behavior of Yttrium Sialon Ceramics," *J. Am. Ceram. Soc.*, **73,** [10] 2834-38 (1990).
[82]S. Bandyopadhyay, M. J. Hoffmann and G. Petzow, "Densification Behavior and Properties of $Y_2O_3$-Containing α-SiAlON Composites," *J. Am. Ceram. Soc.,* **79,** [6] 1537-45 (1996).
[83]M. K. Cinibulk and G. Thomas, "Grain-Boundary-Phase Crystallization and Strength of Silicon Nitride Sintered with a YSiAlON Glass," *J. Am. Ceram. Soc.,* **73,** [6] 1606-12 (1990).
[84]A. Rosenflanz, "Glass-Reduced SiAlONs with Improved Creep and Oxidation Resistance," *J. Am. Ceram. Soc.*, **85,** [9] 2379-81 (2002).
[85]R. Shuba and I.-W. Chen, "Elimination of Grain Boundary Glass in α-SiAlON by Adding Aluminium Nitride," *J. Am. Ceram. Soc.*, **89,** [3] 1065-71 (2006).
[86]I.-W. Chen and A. Rosenflanz, "A Tough SiAlON Ceramic Based on α-$Si_3N_4$ with a Whisker-like Microstructure," *Letters to Nature*, **389,** 701-04 (1997).
[87]C. J. Hwang, D. W. Susnitzky and D. R. Beaman, "Preparation of Multication α-SiAlON Containing Strontium," *J. Am. Ceram. Soc.,* **78,** [3] 588-92 (1995).
[88]Z. K. Huang, Y. Z. Jiang and T. Y. Tien, "Formation of α-SiAlON with Dual Modifying Cations (Li+Y and Ca+Y)," *J. Mater. Sci. Lett.,* **16,** 741-51 (1997).
[89]Z. J. Shen, L.-O. Nordberg, M. Nygren, and T. Ekstrom, "α-SiALON Grains with High Aspect Ratio − Utopia or Reality?," pp. 169-78. Engineering Ceramics '96: High reliability through Processing**.** Edited by G. N. Babini, M. Haviar and P. Sajgalik. Kluwer Academic Press, Netherland, 1997.
[90]M. Zenotchkine, R. Shuba, J.-S. Kim, and I.-W. Chen, "Effect of Seeding on the Microstructure and Mechanical Properties of α-SiAlON: I, Y-SiAlON," *J. Am. Ceram. Soc.,* **85,** [5] 1254-59 (2002).

# Chapter 3

## The Effect of AlN-Polytypoid Formation, Amorphous Glass and Birefringence on Light Transmission in Y-α'-SiAlON Ceramics

### 3.1 Introduction

Until recently, researchers considered silicon aluminum oxynitride (SiAlON) ceramics as materials with limited applications such as wear resistance, cutting tools, abrasives, molten nonferrous metal handling, and refractories because of their superior mechanical, chemical and thermal properties. However, the increasing demand for materials with comparable mechanical properties and optical or electrical properties has driven many advances in ceramic technology including piezoelectric actuators, low k dielectrics, lasers and transparent ceramic windows. Recently, researchers have demonstrated that α'-SiAlON ceramics show promise for optical applications such as transparent windows and hosts for phosphor materials.

Karunaratne *et. al*. first reported visible light transmission in α'-SiAlON.[1] Since then, α'-SiAlON ceramic research has been focused on understanding microstructure control, mechanical properties and optical properties when utilizing different stabilizing cations or sintering conditions. Most reports discuss making composite microstructures to increase the material's toughness while retaining some translucency. Jones *et. al.* fabricated a fully dense 1:1 α'-β' composite by hot pressing a composition in the α'-β' two phase field (m=0.5 and n=0.5 on the α'-SiAlON plane).[2] The sample had a fracture toughness of 4.97 $MPam^{1/2}$, nearly twice that of equiaxed single phase α'-SiAlON, and it was optically translucent in the visible with a maximum

forward transmission of ≈35% at 800 nm.[2] Shuba and Chen fabricated self-reinforced translucent Y-α'-SiAlON with a fracture toughness of ≈5.5 $MPam^{1/2}$ using $La_2O_3$ as an additional sintering aid.[3] Though they did not provide optical property data, their sample was twice as thick (1mm) as Jones' and qualitatively shows clearer visual text with a back lighting.[3] However, even if the composite microstructure samples had mechanical properties equal to or superior to those of other transparent ceramic ballistic armors, such as sapphire (hardness ≈ 22-23 GPa and fracture toughness ≈2.38 to 4.54 $MPam^{1/2}$) and ALON (hardness ≈ 13.8 GPa and fracture toughness ≈2.4-2.9 $MPam^{1/2}$), none have yet to demonstrate high enough light transmission to be applicable for industrial optical applications.[4-6]

"Single phase" α'-SiAlON materials have demonstrated much higher visible light forward transmission than the composite microstructure samples. Chen *et. al.* made 1.06 mm thick Gd-α'-SiAlON ceramics with a forward transmission of 51% transmission at 800 nm.[7] Jones *et. al.* and Chen *et. al.* also achieved similar results using Lu, Y, Nd, and Dy, though with half or less the thickness of the Gd sample.[8; 9] The microstructures of these ceramics consisted of approximately 1 μm equiaxed grains. The relative improvement in visible light transmission between composite microstructures and approximately single phase α'-SiAlON demonstrates the microstructure-property relationship between light transmission and light scattering (see section 2.1). In nominally transparent media, scattering is caused by the changes in refractive index within a material resulting in a loss of transmission. Processing the composite microstructures typically results in excessive glass phase and elongated grains. The presence of excessive amorphous glass and large elongated birefringent crystals introduces numerous potential scattering sites in the ceramics.

Many α'-SiAlON reports use only x-ray diffraction (XRD) data to identify minor secondary phases or to claim phase purity in the ceramic. However, secondary phases can exist below the detection limit of the technique. YAG is an example of a line compound ceramic which experiences loses in optical quality when containing any non-stoichiometric phases during processing.[10] Below the XRD detection limit, the optical transmission quality or transmission/scanning electron microscopy images can be better measures for determining if secondary phases are present. A preliminary study was conducted by Parcianello in which Y-α'-SiAlON was fabricated with equivalent or superior optical properties to that reported in the literature (see Figure 1.2). Figure 1 shows XRD data and back scatter electron microscopy (BSEM) images data of a Y-α'-SiAlON sample. Most of the peaks are due to α'-SiAlON, while a very small peak around 33° indicates the presence of a second phase. The secondary phase concentration is near the limit of the XRD technique, so accurately identifying the crystal is impossible with this data alone. BSEM images and energy dispersive spectroscopy were used to identify the phase as an AlN-polytypoid (see section 3.3.1).

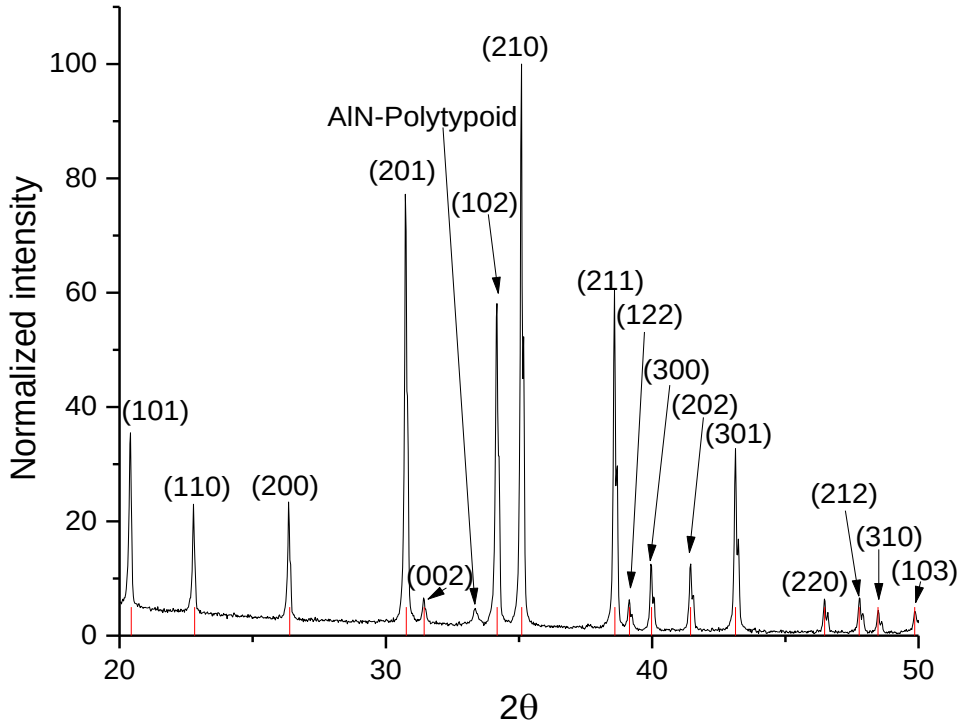


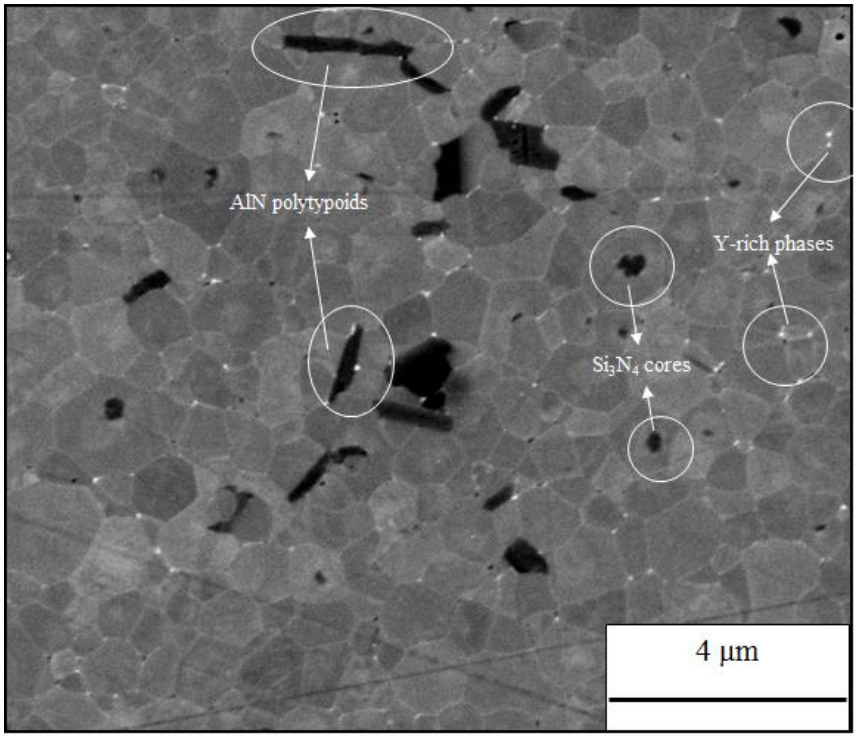


**Figure 3.1 – (a) Showing the XRD data of the sample in Figure 1.2. The red lines indicate α'-SiAlON peaks (ICCD 98-001-1457), while the small peak near 33 °2θ is likely an AlN-polytypoid phase. (b) Backscatter scanning electron image showing the microstructure of**

**the sample. The white areas at triple junctions are amorphous glass phases. The dark areas correspond to AlN-polytypoids or $Si_3N_4$ cores.**

Sun *et. al.* reported 16 compatibility tetrahedra with Y-α'-SiAlON.[11] Based on the compatibility tetrahedra, the various secondary phases that can coexist with α'-SiAlON include AlN-polytypoids, M', β', $Y_2Si_3N_6$, and YAG.[11] However, this is not based on true equilibrium, but rather behavioral studies due to the processing dependencies such as particle sizes, dispersion and different starting materials.[12] Also, compatibility tetrahedra refer to a liquid phase's crystallization pathways during cooling. Though α'-SiAlON forms via a solution-reprecipitation mechanism, no evidence in the literature suggests that homogeneous nucleation from the melt ever occurs in the formation of other SiAlON phases during α'-SiAlON processing. There are two reasons that crystallization upon cooling may be ignored. First, studies of α'-SiAlON liquid phase grain boundary crystallization require careful heat treatments over a long time, usually about 7 to 24 hours.[13; 14] The second reason is based on the confusion principle observed in bulk metallic glasses whereby multiple elements in a composition inhibit crystallization due to various crystals competing to form.[15] Due to the complexity of the crystal structures in the R-Si-Al-O-N system (where R is a cation that stabilizes α'-SiAlON) and the 5 element system, crystallization of the melt is difficult unless the initial nucleation barrier is circumvented.

Current evidence in the literature suggests heterogeneous nucleation plays a critical role in secondary phase formation. Heterogeneous nucleation requires the particles or grains to have a similar crystal structure and lattice parameter to the nucleating phase. It is known that α'-SiAlON and β'-SiAlON primarily form via nucleation on α and β-$Si_3N_4$.[16; 17] Many of the solid solution phases in the M-SiAlON systems have a similar crystal structure and lattice parameters to end member phases. In the case of AlN-polytypoids, the structures differ from wurtzite AlN due to stacking sequence differences created by inversion domain boundaries, but have similar

lattice parameters (except in the *c*-direction).[12; 18; 19] Figure 3.1(b) shows that the AlN-polytypoids form via heterogeneous nucleation because they are not homogeneously dispersed. Shuba and Chen's data also suggests heterogeneous nucleation takes place.[3] Varying the AlN content in Y-α'-SiAlON by $\pm$ 5 wt% showed a significant increase or decrease, respectively, in the AlN polytypoid content in their BSEM images.[3] However, they did not discuss this aspect of the microstructure control. As seen in the experiments below, a 5 wt% change is a very small overall increase or decrease in the overall composition. Thus, such drastic changes are likely due to occur through a change in nucleation frequency via the introduction or removal of heterogeneous nuclei. Finally, Inger-Lise Tangen *et. al.* showed "small AlN grains" inside AlN-polytypoid grains of AlN - AlN-polytypoid composites.[20] These "small AlN grains" are likely to be heterogeneous nucleation sites for AlN-polytypoid formation.

It is not known what light scattering sources are dominant in translucent α'-SiAlON ceramics. Secondary phases or birefringence may act as the dominant scattering mechanism. Liu *et. al.* used the Apetz *et. al*. birefringent scattering model to determine the refractive indices and the birefringence of various M-α'-SiAlON (ranging from 0.0045 for YbNd-α'-SiAlON to 0.0136 for Y-α'-SiAlON).[21] However, they relied only on XRD to identify phase purity (other than amorphous glass and M' found in some samples) and did not report any BSEM images.[21] Utilizing TEM images, they estimated the amount of amorphous glass to range from ≈3 to ≈5 vol%.[21] The glass phase and any undetected crystalline secondary phases may scatter light in their ceramics if their size approaches the wavelength of light. Thus, their results may be skewed because they assumed that birefringence is the only scattering source in the α'-SiAlON ceramics.

Once secondary phases are no longer a scattering source, theoretical light transmission can be achieved by limiting birefringent light scattering. Texturing and grain size reduction are

the primary means for limiting birefringent scattering in ceramics. α'-SiAlON ceramic texturing work and understanding is limited. A high quality texture has not been reported in the literature in α'-SiAlON ceramics.[22; 23] However, it is well understood that α'-SiAlON's microstructure evolution is controlled via seeded nucleation and growth.[24-27] Kumagai and Messing showed that the grain size in seeded ceramics is determined by the nucleation frequency.[28] Equation 3.1 shows the relationship between the grain size (D), grain shape (k) and the nucleation frequency ($N_v$) as proposed by Kumagai *et. al*:[28]

$$D = kN_v^{-\frac{1}{3}} \qquad \text{eq. 3.1}$$

Reports on α'-SiAlON ceramic grain size control have been limited to achieving large, anisotropic grains to increase the fracture toughness. These studies generally did so by decreasing the overall nucleation frequency to allow for growth of α'-SiAlON. Based on the above model, increasing the nucleation frequency should result in the opposite effect.

No study has systematically investigated the relationships between powder processing α'-SiAlON ceramics, secondary crystalline phase formation in α'-SiAlON ceramics, the α'-SiAlON ceramic's grain size, and the dominant light scattering source in transparent α'-SiAlON ceramics. To achieve close to theoretical transparency in α'-SiAlON, understanding such relationships is vital. The following study attempts to understand these relationships, proposes that AlN-polytypoid formation occurs due to heterogeneous nucleation on AlN particles, and analyzes the processing-microstructure-optical property relationship in various α'-SiAlON compositions.

## 3.2 Experiment

### 3.2.1 α'-SiAlON Compositions

As described in section 2.2.1, α'-SiAlON ceramic compositions follow the general formula $R_{m/v}Si_{12-(m+n)}Al_{m+n}O_nN_{16-n}$, where v is the valence of the R cation. The base composition of all samples is m=1.25 and n=1.15. Compositions in this study are designated by their shift away from the nominally stoichiometric α'-SiAlON. In this study, AlN deficient (AD#), excess $Y_2O_3$ (EY#), and excess stoichiometric ratio oxides (ESRO#) are used as the designations. The number at the end represents the wt% difference from the stoichiometric content. For instance, EY10 represents a 10 wt% increase in the stoichiometric $Y_2O_3$ concentration. A final sample designation, excess silicon nitride (ESN), refers to samples intended to decrease the grain size based on a model prediction.

#### 3.2.1.1 Preliminary Study

Before attempting to control secondary phase formation, a preliminary stoichiometric sample was made to establish a baseline for the powder composition and thermal treatments used in this study. The nominal composition lies near the phase boundary of the α'-SiAlON plane defined by Shen and Nygren with m = 1.25 and n = 1.15.[29] However, due to the uncertainty in the nitride powder oxygen content, attempts to optimize the composition for light transmission were performed by assuming various oxygen contents in the powders and adjusting the powder compositions accordingly. The best sample (see Figures 1.2 and 3.1) fabricated is comparable or

superior to other work in the literature and assumed a 1.4 wt% and a 1.8 wt% oxygen content in the $Si_3N_4$ and AlN powders, respectively. Also, the sample had the minimum amount of amorphous glass phase out of all tested compositions. Kennametal used a LECO TC600 oxygen gas analyzer to analyze the AlN and $Si_3N_4$ powders and measured 1.2 wt% and 1.52 wt% oxygen for the powders, respectively. When the nitride powders were analyzed for oxygen content, neither smelled of ammonia anymore, suggesting that oxidation of the powders at room temperature had become kinetically limited. For the oxygen analysis performed by Kennametal, the nitride powders were heated to 100 °C to remove water adsorbed on the surface, moved to an Argon filled glove box and sealed before the analysis. Based on the assumption of a higher oxygen wt% in the AlN powder than $Si_3N_4$ powder and the effects of excess AlN demonstrated by Shuba *et. al*., the oxygen assumptions resulted in excess AlN, which decreased the glass phase concentration and made the sample slightly off stoichiometry.[30]

#### 3.2.1.2 Methodology for Reducing AlN-polytypoids Formation in Y-α'-SiAlON and Decreasing Grain Size

The general methodology for avoiding AlN-polytypoids was to make compositions above the α'-SiAlON plane. By using compositions above the plane, the driving force for the dissolution of AlN should increase and the driving force for the formation of AlN-polytypoids should decrease. Two methodologies were used to determine the compositions utilized in this study.

The first methodology is based on the reaction sequence for Y-α'-SiAlON formation. As discussed in section 2.2.3, Y-α'-SiAlON's reaction sequence involves an oxynitride liquid which reacts and consumes AlN and $Si_3N_4$ during sintering. Based on Hwang and Chen's study, AlN is

preferentially wetted and reacted before $Si_3N_4$ by the eutectic oxide.[31] An increase in the liquid phase content is expected to result in a systematic decrease of AlN-polytypoid phase formation due to an increased driving force for dissolution. Thus, 2 separate compositional shifts were chosen: excess $Y_2O_3$ (EY) and excess stoichiometric ratio oxides (ESRO). The ESRO compositions increase the total oxide content, but with the same ratio as that observed in stoichiometric α'-SiAlON. Thus, the eutectic oxide liquid phase composition will increase, but the relative composition will not change. As AlN-polytypoids are a solid solution of Si-O and Al-O bonds into the AlN structure, the EY compositions were chosen to increase the oxide content without increasing the $Al_2O_3$ or $SiO_2$ concentration. The EY compositions increase only the $Y_2O_3$ oxide content which increases the oxide content and shifts the composition of the oxide liquid phase more to $Y_2O_3$.

The second methodology for determining sample compositions to reduce the AlN polytypoid concentration is based on the proposal that nucleation of AlN-polytypoids occurs via heterogeneous nucleation. Based on this, the principles of heterogeneous epitaxial nucleation determine whether nucleation occurs: the particles must be stable and must have a similar crystal structure and lattice parameters. Thus, reducing the number of nuclei by removing AlN from the stoichiometric batch should result in a decrease in the overall AlN-polytypoid content. Thus, AlN deficient (Al content is kept constant with the stoichiometric amount with respect to AlN) samples should have less AlN-polytypoids due to the above considerations. Also, this composition has excess liquid phase content (excess $Y_2O_3$) which is expected to increase the driving force for AlN dissolution.

Grain size control was performed by increasing the α'-SiAlON nucleation frequency using excess $Si_3N_4$. Rosenflanz *et. al*. showed α'-SiAlON's structure can handle a large range of

off stoichiometry without an observable reduction in density.[32] Based on the results displayed in the following discussion and by Rosenflanz *et. al.*, ≈17 wt% excess $Si_3N_4$ with respect to the entire sample weight was added to AD10.

Table 3.1 reviews all of the compositions examined in this study. Figure 3.2 graphically shows the overall changes in the composition on the Janecke prism and α'-SiAlON plane. Figure 3.2(a) shows the overall compositional shift while Figure 3.2(b) shows an enlarged α'-plane with each composition plotted.

| Sample Type | Composition Shift | Wt% Shifts | Goal of Composition Change |
|---|---|---|---|
| Stoichiometric | None | None | Establish Baseline |
| EY | Excess $Y_2O_3$ | 5, 10, 20 | Increase the Liquid Phase Concentration to Dissolve AlN Particles |
| ESRO | Excess Stoichiometric Oxide Ratio | 7.5, 10 | Increase and Change the Liquid Phase Composition to Dissolve AlN Particles |
| AD | AlN deficient | 10, 20 | Decrease the AlN-Polytypoid Nucleation Frequency |
| ESN | Excess Silicon Nitride | 17.13 | Increase the α'-SiAlON Nucleation Frequency |

**Table 3.1 – Various compositions used in this study to reduce AlN-polytypoids formation in α'-SiAlON microstructures. The wt% shifts for each sample series corresponds to the stoichiometric amount, not the overall sample batch amount.**

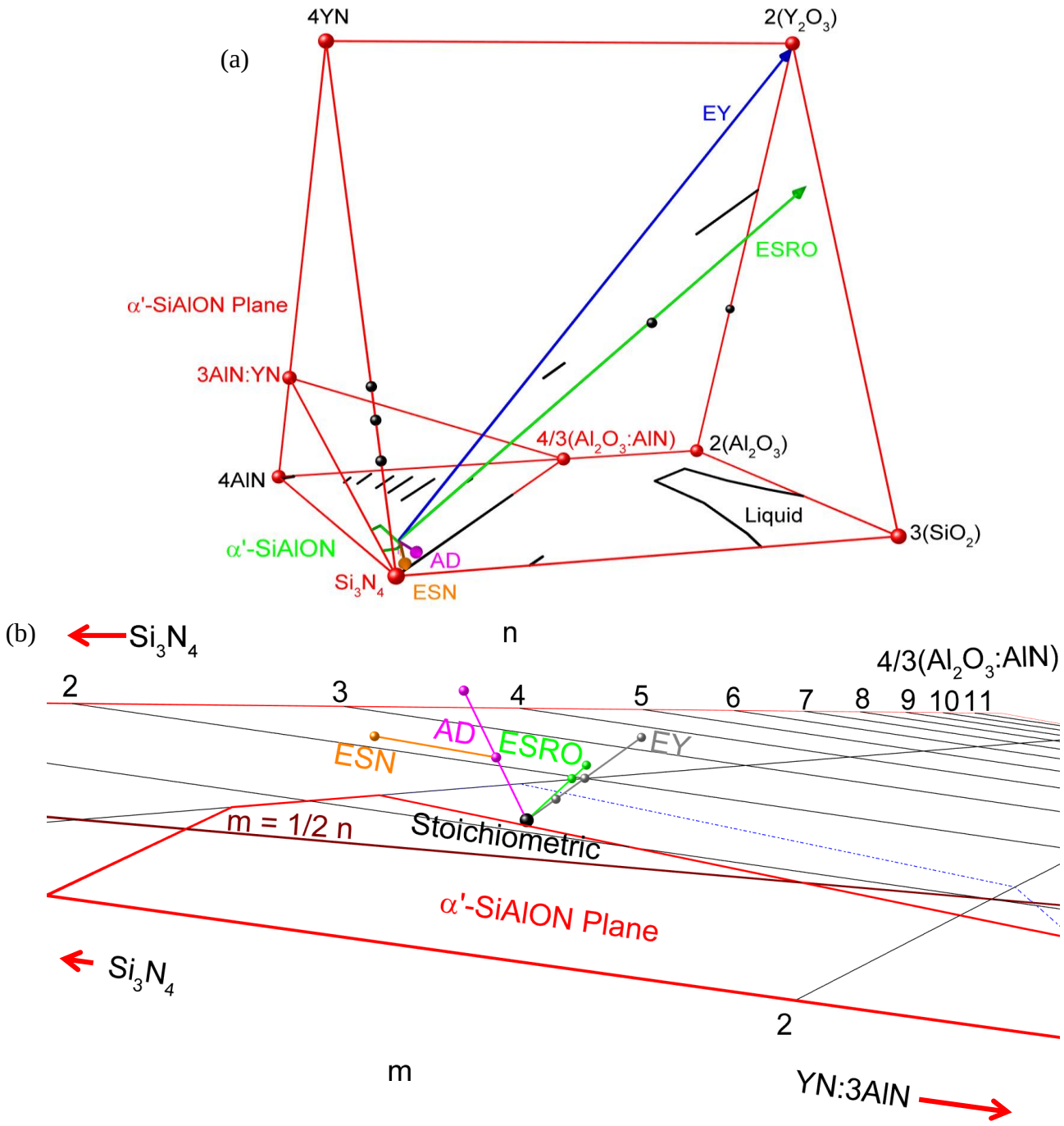


**Figure 3.2 – (a) Compositional shift paths for the various compositions. Each blue arrow shows the compositional shift used in this study. The compositional shifts are excess $Y_2O_3$ (EY), excess stoichiometric ratio oxides (ESRO), and aluminum nitride deficient (AD). (b) Zoomed in α'-SiAlON plane viewing from the $Si_3N_4$ – YN:3AlN join. The relative compositional shift for each sample is shown. Each sphere represents one of the compositions along the specified composition shift, where moving further away from the plane is a greater shift.**

### 3.2.2 Powder Processing

α'-SiAlON samples were prepared using high purity α-$Si_3N_4$ (UBE, SN-E10, Oxygen content <2.0 wt%, α-phase >95 wt%, specific surface area 9-13 $m^2/g$, $d_{50} \approx 500$ nm, Tokyo, Japan), AlN (Tokuyama, E-Grade, Oxygen content ≈0.8 to 0.9 wt%, specific surface area 3.27-3.47 $m^2/g$, particle size ≈0.96-1.07 μm, Tokyo, Japan), α-$Al_2O_3$ (Sumitomo, AKP50, >99.995, 0.2 μm), $Y_2O_3$ (ShinEtsu, BB, >99.99%, specific surface area 35.4 $m^2/g$, Tokyo, Japan) and fumed $SiO_2$ (Evonik Industries, Aerosil 200, > 99.8 wt% $SiO_2$ specific surface area 200 $m^2/g$, Germany) when appropriate. The same powders were used in the preliminary study. Figure 3.3 shows representative SEM images of the as received $Si_3N_4$ and AlN powders stuck on carbon tape. Blown menhaden fish oil (Tape Casting Warehouse, Grade Z-3), xylenes (J.T. Baker, ACS reagent grade) and anhydrous ethanol (Koptec, 200 proof pure Ethanol) were used as the dispersing agent or solvents. Tape cast samples used a 50:50 mixture by weight of ethanol : xylenes, while slip cast samples used only xylenes. The solids loading for all samples varied from 20 to 30 vol%. All slurries were ball milled for 24 h using high purity $Al_2O_3$ media (99.9%, 5 mm diameter, Nikkato Corp., Sakai, Japan).

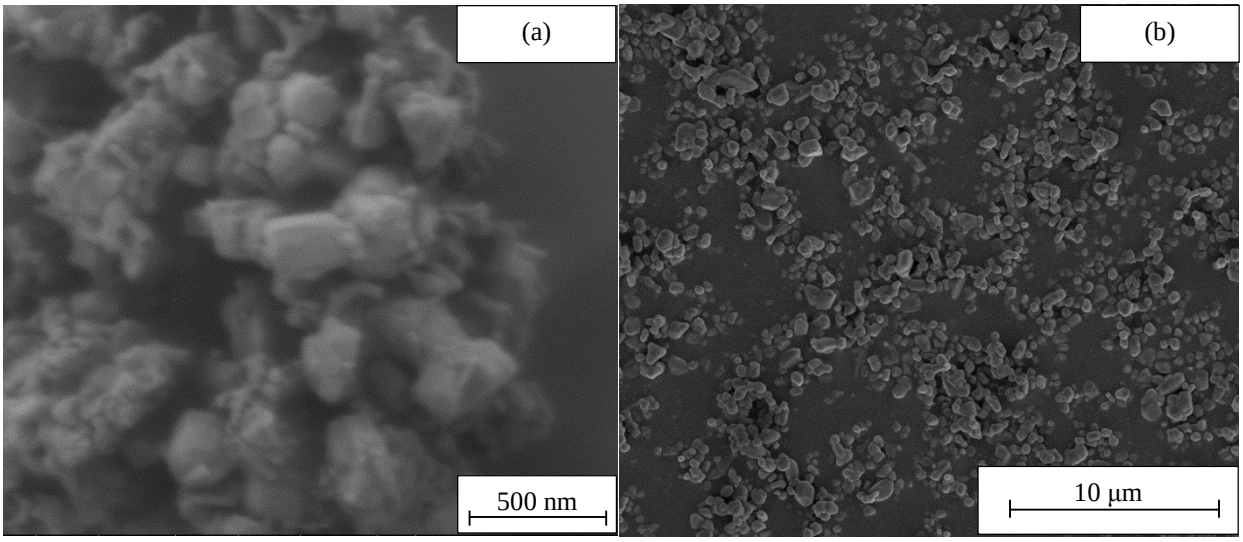


**Figure 3.3 - SEM micrographs of the as-received $Si_3N_4$ and AlN powders, respectively.**

The preliminary stoichiometric samples were prepared using tape casting. After the first 24 h ball milling, polyvinyl butyral (Tape Casting Warehouse, B-98 Grade), butyl benzyl phthalate (Tape Casting Warehouse, UCON50HB2000 Grade), and polyalkylene glycol (Tape Casting Warehouse, S-160 Grade) were added as a binder and plasticizers, respectively. The slurry was milled for an additional 24 h. Under constant stirring, the slurry was sieved using a 55 μm mesh screen and deaired. Cyclohexanone (Alfa Aesar, >99%) was added as a deskinning agent. The slurry was tape cast on silicone-coated Mylar (Tape Casting Warehouse, G10JRM) using a doctor blade gap height of 0.36 mm and a casting rate of ≈75 cm/min. After drying, square pieces were cut from the 80-100 μm tape. Stacks of layers were laminated isostatically at 74 °C and 20.7 MPa for 30 min. The samples were calcined at 600 °C for 12 h in air to remove the organics. After calcination, the samples were cut into 2.54 cm diameter cylinders (diameter of the hot pressing die) and cold isostatically pressed at 200 MPa.

Several tests showed little to no difference between tape cast and slip cast samples. Thus, all other samples were slip cast on Plaster of Paris using covered plastic cups to allow unidirectional casting. The slips were made using the same method as above, but without the

binders, plasticizers and deskinning agent used for tape casting. Additionally, the slurries were only ball milled for 24 h. Slip cast samples were dried for 24 h after casting. The samples were calcined at 600 °C for 12 h in air to remove the organics. After calcination, the samples were cold isostatically pressed at 200 MPa.

### 3.2.3 Sintering

All green samples were thinned to 3.2 mm thickness using 600-grit SiC sandpaper. Above 3.2 mm, samples developed a "core" structure during hot pressing where the middle of the sample contained a darker region likely due to $Si_3N_4$ decomposition and formation of free Si or silicides which limit light transmission. Except for the preliminary experiment, samples were surrounded by a multiple layer powder bed inside a graphite die as shown in Figure 3.4 to limit $Si_3N_4$ decomposition and the core structure formation. The preliminary samples were sintered using only a hexagonal boron nitride (BN) (Lower Friction, MK-hBN-N70, >99%, 70 nm, Mississuaga, Ontario Canada) powder bed. The powder mix layer contained an α-$Si_3N_4$, BN, and fumed $SiO_2$ mixture with a 70:28:2 wt% ratio. The powder mix was used to limit nitride decomposition during sintering. BN layers were used to separate the powder mixture to prevent reactions from the sample and graphite pistons. The samples were all hot pressed in a graphite resistance furnace at 1700 °C and 35 MPa unless otherwise stated. Samples were hot pressed under a vacuum at $\approx 10^{-6}$ torr. Figure 3.5 shows the sintering heat treatment used for all samples.

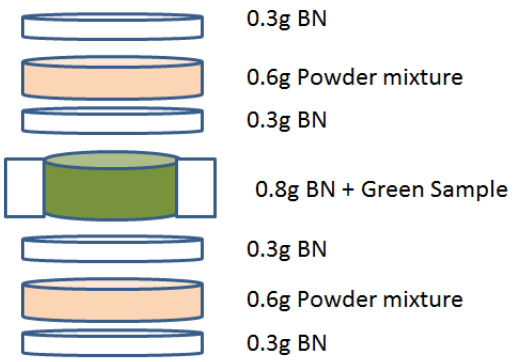


**Figure 3.4 – Schematic showing the powder bed used for hot pressing α'-SiAlON samples.**

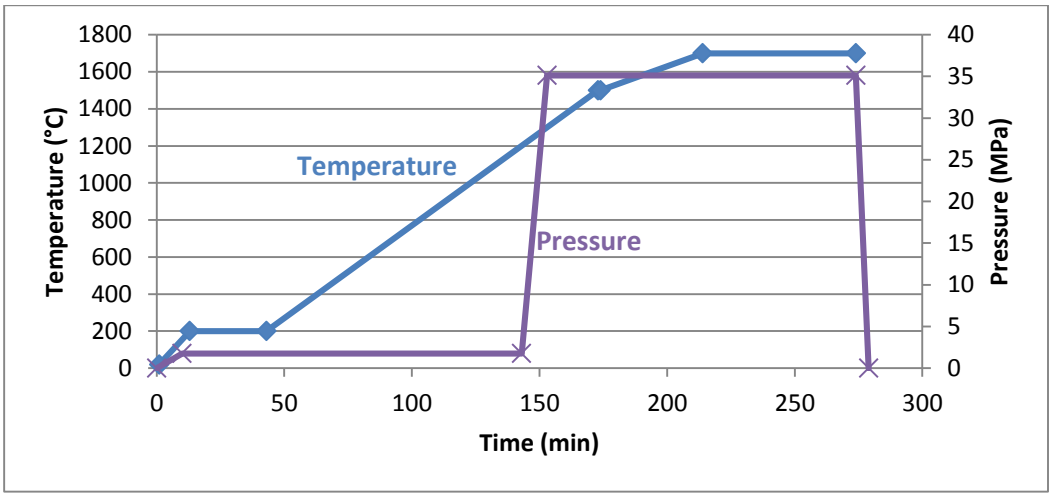


**Figure 3.5 – α'-SiAlON hot pressing heat treatment procedure.**

After sintering, all samples were sand blasted to remove the powder bed. Sample surfaces were ground flat to remove the decomposed surface layers. The samples were polished with 1 μm diamond for SEM characterization and light transmission analysis.

### 3.2.4 Characterization

Phase analysis was performed using XRD (Empyrean, PANalytical). Chemical analysis was used to examine the composition in microstructural features by using energy dispersive X-ray spectroscopy (EDS) (FEI). Field emission scanning electron microcopy (FESEM) (FEI) was used to analyze the microstructures of polished samples using a BSEM detector. The areal AlN-

polytypoid areal % was analyzed using ImageJ software. The images were analyzed by removing all microstructural features that were not identified as AlN-polytypoids and then using pixel counts to determine the area of each polytypoid in the microstructures. A minimum area of ≈750 $\mu m^2$ was used for the analysis. As the AlN-polytypoid grains are randomly oriented in the sample microstructures, the areal fraction is considered to be roughly equal to the volume fraction, thus their concentration is referred to as a volume percentage.

The particle sizes of the nitride powders were analyzed using FESEM secondary electron imaging and ImageJ software. $Si_3N_4$ and AlN particles were dispersed in xylenes using MFO and an ultrasonic bullhorn, dried on glass substrates and collected with carbon-tape. Due to the finer particle size, the $Si_3N_4$ particles were diluted to $\approx 10^{-4}$ Molar and suspension drops were dried on a heated Si substrate. Particle sizes were measured using line length measurements in the ImageJ software. As most particles were roughly equiaxed or had a slight anisotropy, all particle diameters were measured at their longest length. Aggregate particle sizes were not measured, thus the distribution data only contains primary particle sizes.

Light transmission of samples was compared by observing samples directly on a backlit background and 10 cm above a backlit background. A camera was used to take images 64 cm above the backlit background and was focused on the background text. The total optical transmission of the samples was measured using UV-visible spectroscopy with a Perkin-Elmer Lambda 950 UV-Vis-NIR spectrophotometer. The detector used an integrating sphere to detect all transmitted light.

## 3.3 Results and Discussion

### 3.3.1 Effects of Compositional Shifts on AlN-polytypoid Formation

The baseline optical quality and microstructural features were established in the preliminary study (see Figures 1.2 and 3.1). The XRD (Figure 3.1(a)) shows that the sample is close to phase purity, but contains an unidentified peak. The BSEM image in Figure 3.1(b) shows multiple microstructural features. Due to their high concentration of $Y^{3+}$, the bright white regions are assumed to correspond to a YSiAlON amorphous glass phase. α'-SiAlON appears light grey because of the smaller $Y^{3+}$ concentration. Also, most α'-SiAlON grains contain a brighter region inside the grains. The brighter regions are formed due to the higher Y/Al concentration that occurs at nucleation. Thus, these brighter regions are evidence of heterogeneous nucleation on $Si_3N_4$. The darker phases in the microstructure do not contain $Y^{3+}$, thus they are assumed to be either α-$Si_3N_4$ or a different SiAlON phase. Due to the heterogeneous nucleation, α-$Si_3N_4$ cores can be identified if a bright region is seen around the core grain inside the α'-SiAlON grain. Thus, all dark phases not containing a bright ring around them in an α'-SiAlON grain belong to a secondary phase.

Similar microstructural features are observed in all samples in this study. Thus, interpretation of the BSEM images is the same for all samples. Figure 3.6 shows EDS data from ESRO10 sample to determine if the dark phases are AlN-polytypoids or another SiAlON phase. Based on the higher Al content, the phase must be an AlN-polytypoid or a high z β-SiAlON ($Si_{6-z}Al_zO_zN_{8-z}$ where $0 \leq Z \leq 4.2$). The dark phase is not likely to be β-SiAlON because the XRD peaks around ≈27° and ≈33° 2θ (ICCD 00-036-1333) have nearly the same peak height in β'-SiAlON. Thus, if one of the peaks is present in the data, the other peak will be as well, unless

the material is significantly textured. Based on the literature, the phase diagram, the high Al:Si ratio in the EDS data, and the XRD pattern in Figure 3.1(a), the dark phase is judged to be an AlN-polytypoid.

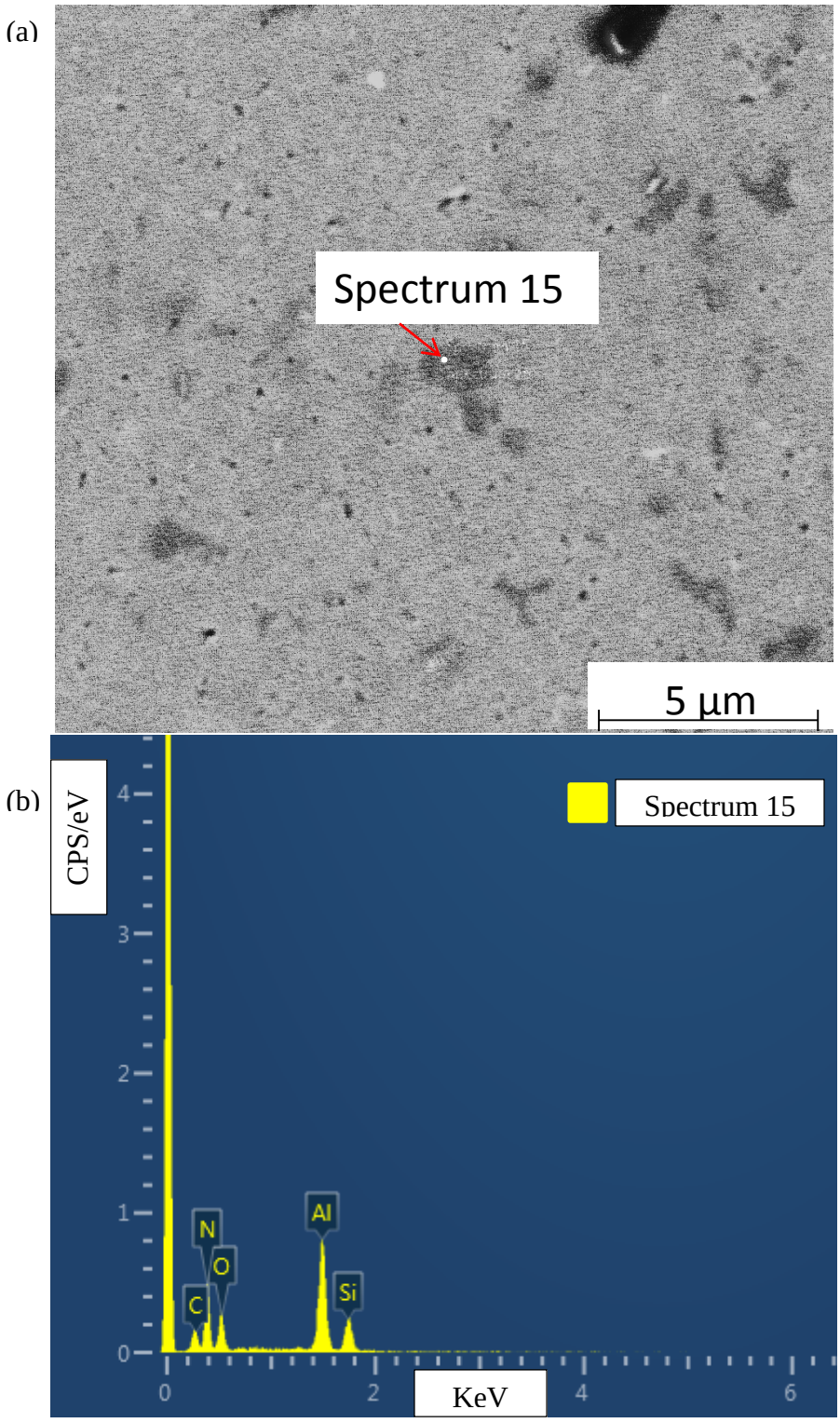


**Figure 3.6 – (a) BSEM image of ESRO10 showing the location of spot EDS analysis on the dark phase. The white dots in the middle of the micrograph show where the EDS analysis was done. (b) Showing the EDS spectra from the spot analysis. Similar EDS spectra were seen in all samples containing AlN-polytypoids. The accelerating voltage was 5 keV. The interrogated volume is approximately 0.014 µm$^3$.**

Due to the possibility of scattering from the AlN-polytypoid phases, attempts were made to reduce their concentration. As a baseline, the stoichiometric sample has an AlN-polytypoid concentration of 1 vol% based on polished BSEM images. The ESRO and EY compositions were designed to increase the driving force for AlN dissolution by increasing the liquid phase content. Thus, as the oxide content increases in the ESRO and EY samples, the residual amorphous glass phase concentration increases. Figure 3.7 shows BSEM micrographs of the ESRO7.5 and ESRO10 samples. The top and bottom micrographs show higher and lower AlN-polytypoid concentrations in the samples, respectively. The ESRO samples show an increase in the AlN-polytypoid content as the oxide content is increased. The ESRO7.5 and ESRO10 samples have an average AlN-polytypoid content of 1.75 and 2.3 volume %, respectively. The AlN-polytypoids form in large clusters as seen in the top micrographs, but there are large areas with little or no AlN-polytypoids as show in the bottom micrographs.

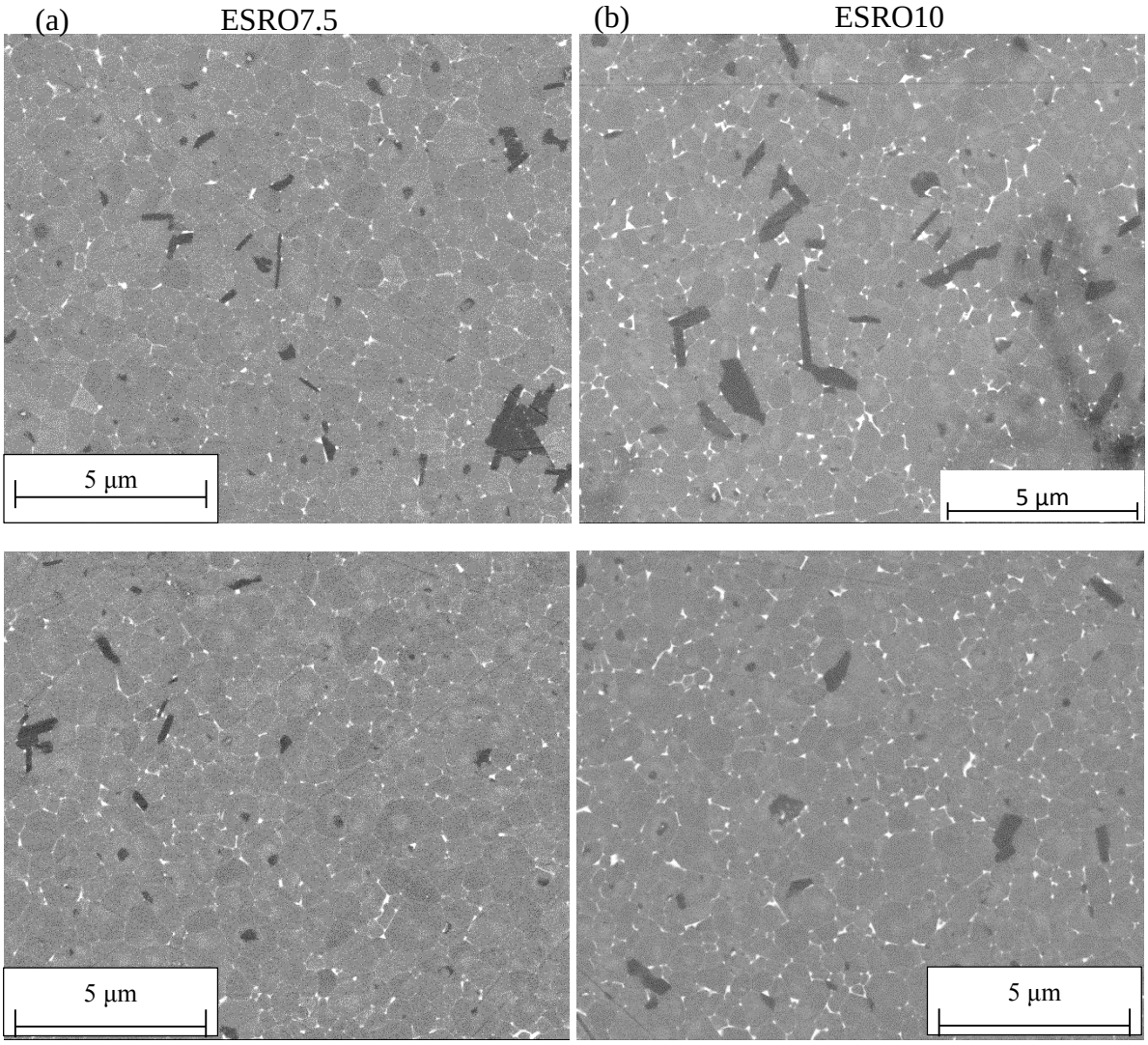


**Figure 3.7 – SEM micrographs of the ESRO samples. The top and bottom micrographs demonstrate the inhomogeneous distribution of AlN-polytypoids in the microstructure. Column (a) shows the microstructure of ESRO7.5. Column (b) shows the microstructures of ESRO10.**

Figure 3.8 shows BSEM micrographs from the EY5, EY10, and EY20 samples. Similar to Figure 3.7, the top and bottom micrographs show areas of high and low concentration of AlN-polytypoids. EY5 shows an initial increase of AlN-polytypoid content to 1.6 vol%. The concentration decreases to 0.98 vol% in the EY10 sample. As the oxide content is increased to 20 wt%, the AlN-polytypoid content decreases to 0.5 vol %. The residual glass phase content does not significantly increase until 20 wt% excess $Y_2O_3$. The AlN-polytypoids do not cluster as much as in the ESRO samples, but tend to form groups of smaller grains.

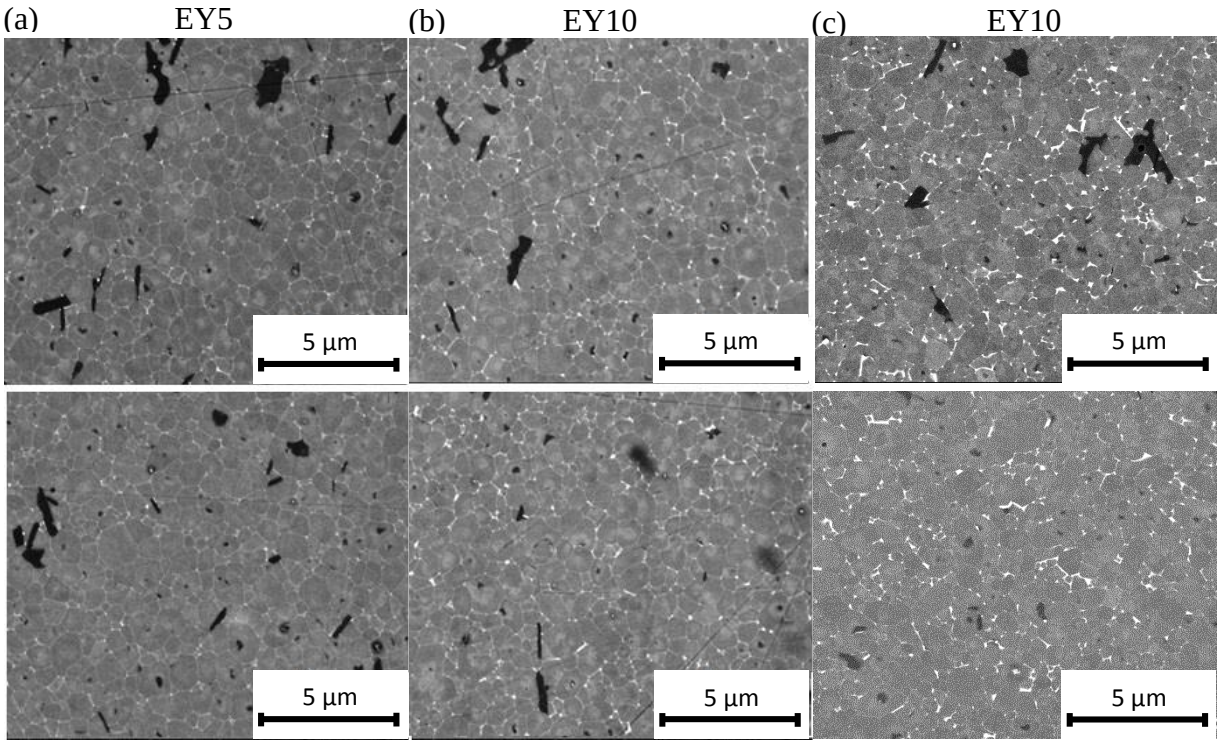


**Figure 3.8 - SEM micrographs of the EY samples. The top and bottom micrographs demonstrate the inhomogeneous distribution of AlN-polytypoids in the microstructure. Column (a) shows the microstructure of EY5. Column (b) shows the microstructures of EY10. Column (c) shows the microstructure of the EY20. There is a relative decrease in the AlN content as the $Y_2O_3$ content is increased above 5 wt%.**

Since the ESRO and EY samples compositions did not significantly reduce the AlN-polytypoid concentration without adversely affecting the optical properties (see section 3.3.2), another composition series based on the heterogeneous nucleation of AlN-polytypoids on AlN was fabricated. Figure 3.9 shows BSEM micrographs of the AD10 and AD20 samples with decreasing AlN content from left to right, respectively. The top and bottom micrographs show high and low AlN-polytypoid concentrations in the samples, respectively. Similar to the ESRO and EY samples, the residual amorphous phase increases as the AlN deficiency increases, which is expected based on Shuba and Chen's study on the removal of the residual amorphous phase and the excess $Y_2O_3$ in the composition.[30] AD10 and AD20 show a significant decrease to 0.11 vol% and 0 vol% AlN-polytypoids, respectively. Figure 3.10 shows the XRD data for both

AD10 and AD20 samples. The absence of the AlN-polytypoid verifies that the concentration was either reduced below the detection limit or completely removed from the structure. Similar to the EY20 sample, AD20 did not remove the AlN-polytypoid content without adversely affecting the optical properties (see section 3.3.2). Table 3.2 summarizes the AlN-polytypoid vol% in all explored compositions.

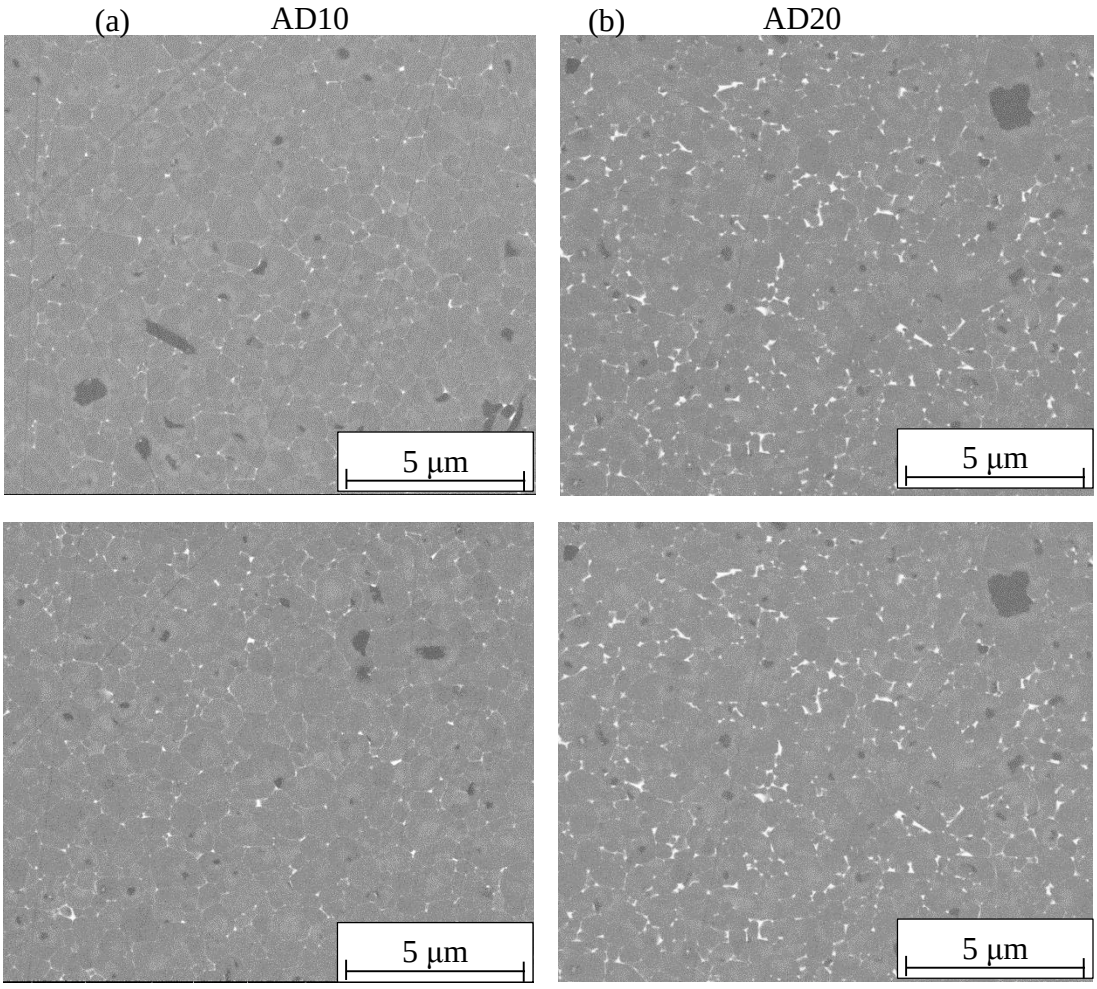


**Figure 3.9 - SEM micrographs of the AD samples. The top and bottom micrographs demonstrate the inhomogeneous distribution of AlN-polytypoids in the microstructure. Column (a) shows the microstructure of AD10. Column (b) shows the microstructures of AD20. There is a drastic decrease in the AlN-polytypoid concentration as the sample becomes more AlN deficient. AlN-polytypoids were not observed in AD20 sample.**

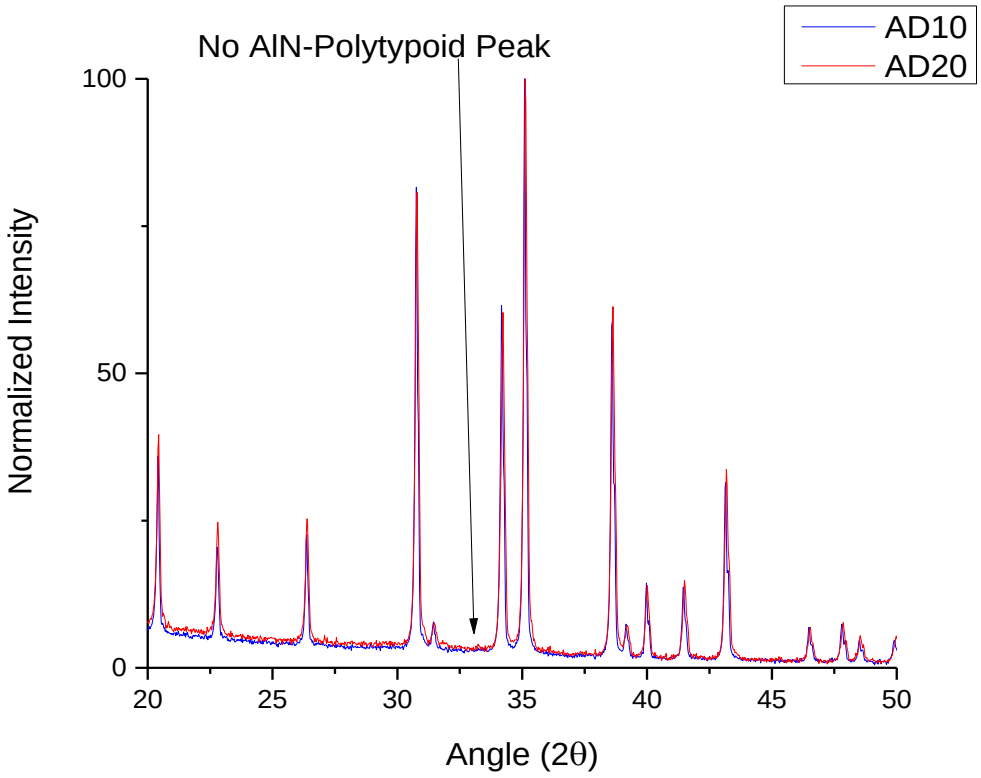


**Figure 3.10 – XRD pattern of the AD10 (blue) and AD20 (red) samples. The absence of the AlN-polytypoid peak between 33° and 34° 2θ verifies the reduced amount of AlN-polytypoids in each structure.**

| Sample | Approximate AlN-Polytypoid Vol% |
|---|---|
| Stoichiometric | 1 |
| ESRO7.5 | 1.75 |
| ESRO10 | 2.3 |
| EY5 | 1.6 |
| EY10 | 0.98 |
| EY20 | 0.5 |
| AD10 | 0.11 |
| AD20 | 0 |

**Table 3.2 – Showing the AlN-polytypoid vol% of each sample series. The vol% was averaged over a minimum of four 190 μm$^2$ micrographs. Secondary phases exclude α-$Si_3N_4$/β-$Si_3N_4$ as these phase can nucleate α'-SiAlON.**

To explain the relative increase or decrease of AlN-polytypoids, recall the composition shifts of the EY, ESRO, and AD sample series. The EY series contains excess $Y_2O_3$, the ESRO series contains excess $Y_2O_3$, $Al_2O_3$, and $SiO_2$, and the AD series contains excess $Si_3N_4$ (thus $SiO_2$) and $Y_2O_3$. The AlN-polytypoid phases all lie near the AlN corner of the phase diagram which is below the alpha plane. As each composition change increases, the driving force for AlN particle dissolution and AlN-polytypoid formation is expected to increase and decrease respectively because the composition changes increase the liquid phase concentration and the average composition moves further away from the AlN-polytypoids on the phase diagram (see Figure 3.2(b)). However, both the ESRO and EY compositional shifts show an increase in the AlN-polytypoid concentration. For AlN-polytypoid formation to occur, the liquid phase composition must be rich in AlN, $Al_2O_3$, and $SiO_2$ which occurs as the eutectic oxide melt reacts with AlN. Inherently, the composition of the liquid phase changes as more particles dissolve, resulting in inhomogeneous regions in the liquid phase. The ESRO samples contain relatively more $Al_2O_3$ and $SiO_2$ than the other compositions and it is the only composition series to directly add $SiO_2$ particles into the batch, which may result in further inhomogeneous composition in the liquid melt. Once AlN-polytypoids nucleate, the excessive content of these components in the liquid melt promote growth in the ESRO samples, creating large clusters of AlN-polytypoid grains. The AlN-polytypoid increase in the EY5 samples may occur for a similar reason. The excess $Y_2O_3$ content causes an increase in the glass phase content without significantly "diluting" the $Al_2O_3$ and $SiO_2$ concentration. Thus, AlN-polytypoids can nucleate, but these are more spread out with less growth. As the $Y_2O_3$ content begins to "saturate" the liquid melt composition with respect to $Al_2O_3$ and $SiO_2$, there is less driving force for AlN-polytypoid nucleation, resulting in a decrease in AlN-polytypoid formation.

A similar argument can be applied to the decrease of the AlN-polytypoid concentration in the AD sample series. As the aluminum nitride deficiency increases, there is an increase in the $Y_2O_3$ content, but the $SiO_2$ content increase is limited due to the small amount of surface oxide on the $Si_3N_4$. Thus, more liquid phase is formed, but the liquid phase's local inhomogeneity is "saturated" with $Y_2O_3$ (and $Si_3N_4$ later in the reaction sequence) rather than $SiO_2$ and $Al_2O_3$.

The argument above is insufficient to explain why the nucleation events occur or why the AlN-polytypoid grains are inhomogeneously dispersed in the microstructures of Figures 3.1, 3.7, 3.8 and 3.9. The inhomogeneous nature of the AlN-polytypoids is believed to occur due to a combination of a heterogeneous dispersion of the AlN particles and heterogeneous nucleation. Heterogeneous nucleation may increase the inhomogeneous disparity if the nucleating agent is also a reactant because the competing forces between reacting and nucleating dictate that only the nuclei that do not fully dissolve will cause nucleation. Thus, not every potential nuclei will necessarily serve as a nuclei. Heterogeneous nucleation on wurtzite AlN particles seems to be a probable cause for the formation of AlN-polytypoids based on the similar crystal structure and lattice parameters (except the *c*-parameter) between the AlN-polytypoids and the wurtzite AlN. It is difficult to see the nuclei in the AlN-polytypoid microstructures because the core does not have a strong elemental contrast difference in a backscatter image. Also, a 2D polished surface often does not intersect near the core of the AlN-polytypoid, similar to how 2D sections of grains do not intersect with the grain's widest cross section. Figure 3.11 shows an enlarged micrograph of the ESRO10 sample where a core structure can be seen which is in agreement with the "small AlN grains" shown by Igner.[20]

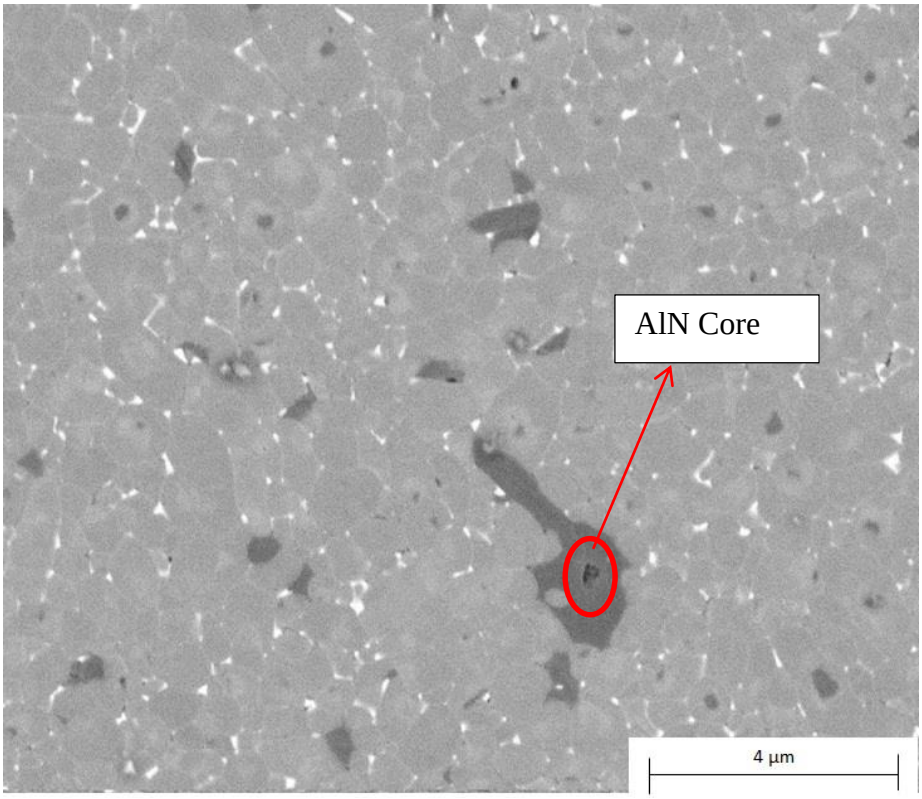


**Figure 3.11 – Enlarged BSEM micrograph revealing an AlN core in the middle of an AlN-polytypoid in the ESRO10 sample.**

Since AlN-polytypoid formation is promoted via a heterogeneous nucleation mechanism, then the nuclei must be stable. Heterogeneous nuclei can be stable either: chemically or size.[27] Because AlN is a reactant in this system, the nuclei are not chemically stable. Larger particles can be considered more stable because of a longer time for dissolution. Thus, large particles in the AlN particle size distribution likely act as heterogeneous nucleation sites. Based on this hypothesis, the AlN particle size distribution was analyzed as shown in Figure 3.12. Most of the AlN particles are under 800 nm in diameter. However, there are AlN particles with a diameter greater than 1.5 µm. Figure 3.13 shows an enlarged image of Figure 3.3(b) and identifies some of the >1.5 µm AlN particles. A statistical analysis of the heterogeneous nuclei size could not be done due to the small number of observable AlN nuclei in the microstructures. Based on the tail of the powder size distribution, ≥1 µm AlN particles are probably acting as heterogeneous nuclei.

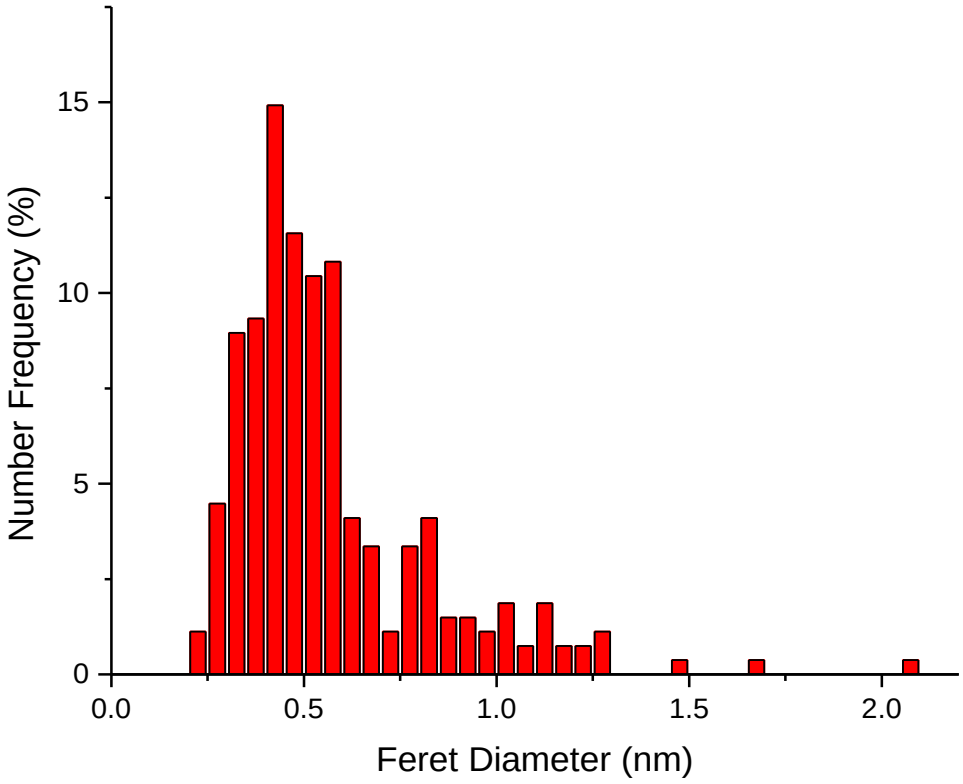


**Figure 3.12 – Particle size distribution of the as-received AlN powder. The analysis covered approximately 270 particles. The Ferret diameter is the longest axis of the particle. Powder size distribution provided courtesy of Ozgur Ozer.**

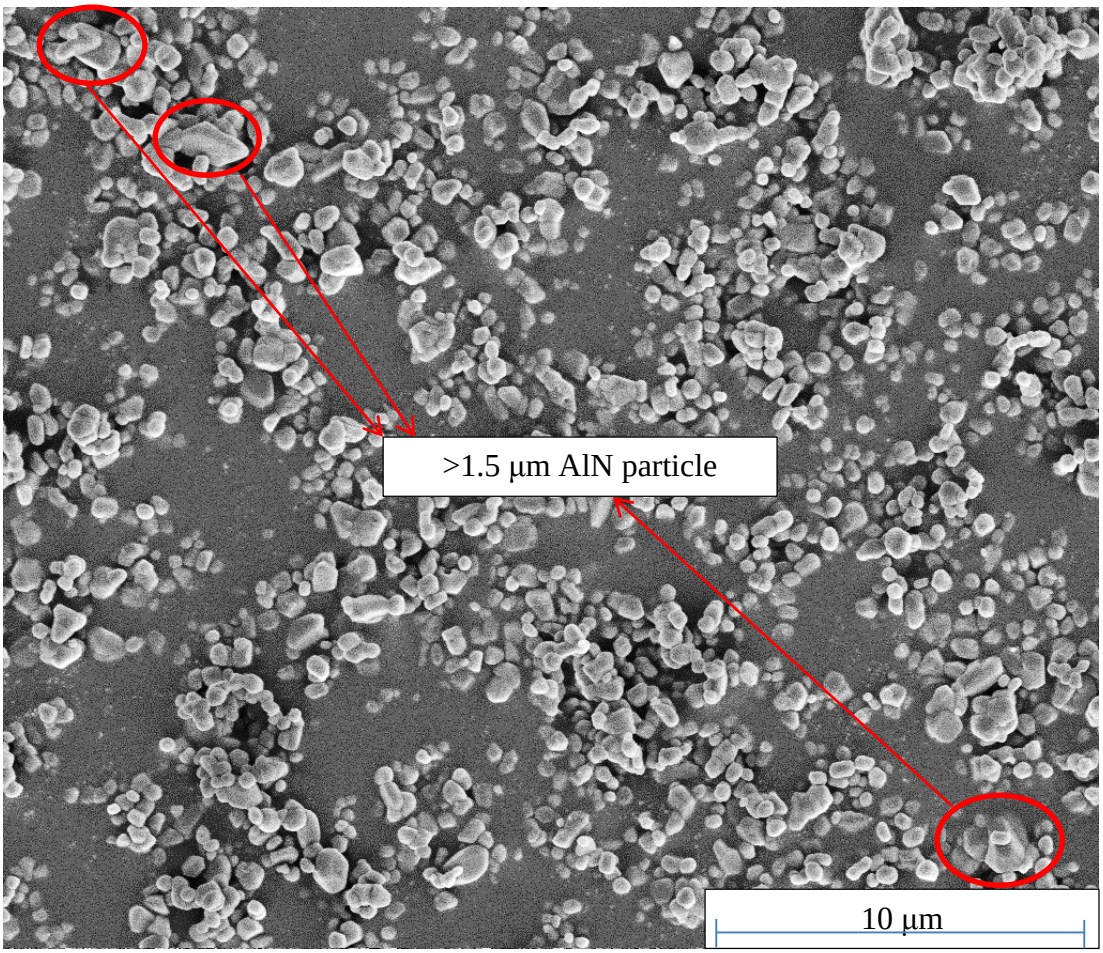


**Figure 3.13 – Enlarged image of Figure 3.3(b) identifying several AlN particles larger than 1.5 μm in diameter.**

A complete explanation for the formation of AlN-polytypoids in the sample series is possible using heterogeneous nucleation and the relative liquid phase compositions. The ESRO samples have the largest increase in large AlN-polytypoid particles because the compositional inhomogeneities are greatest around large AlN particles. Only a few of the largest particles act as nuclei because of the competing driving forces between dissolution into the melt and nucleation of AlN-polytypoids. Since nucleation is favored around these few particles, the crystals can grow to large sizes. The inhomogeneities in EY5 are not as significant. However, the small increase in the liquid phase content does distribute the inhomogeneities to more particles. Thus, more nucleation events occur, but mostly smaller AlN-polytypoid crystals grow

than in the ESRO samples. As the $Y_2O_3$ content increases further, the driving force for dissolution increases and the local inhomogeneities are saturated in $Y_2O_3$, resulting in a decrease in the AlN-polytypoid concentration. The significant decrease in AlN-polytypoid formation in the AD samples is not only due to the increased driving force for AlN dissolution, but the physical removal of the nuclei from the microstructure. In conclusion, AlN-polytypoid phases are not necessarily compatible with α'-SiAlON as suggested in the literature, but rather their presence is due to a lack of a finer particle size AlN powder.

### 3.3.2 Effects of Compositional Shifts and Grain Size on α'-SiAlON Optical Light Transmission

Due to variations in the AlN-polytypoid concentration of the ESRO, EY, and AD samples, the effect of AlN-polytypoids on the optical transmission in α'-SiAlON can be investigated. To establish a baseline of the optical properties, Figure 3.14 shows qualitatively the optical translucency of the preliminary stoichiometric sample when placed directly on top of a backlit background and 10 cm above the backlit background. As the sample is raised above the backlit background, the reduced visual quality (i.e. contrast) of the text indicates the presence of scattering in the sample. The increased scattering occurs due to the path length of light entering the sample increases as light enters from greater angles. At 10 cm, the text behind the stoichiometric sample is nearly unreadable. Figure 3.15 shows the optical properties of the ESRO samples under the same conditions as Figure 3.14. The ESRO samples show approximately the same optical properties when placed on the backlit background, but they show drastically different properties when placed above the backlit background. ESRO7.5 shows better textual contrast than the stoichiometric sample when placed 10 cm above the background, but the sample is also thinner. The text can barely be seen in the ESRO10 sample, indicating a

decrease in the light transmission. A direct comparison between the ESRO7.5 and ESRO10 samples cannot be made because they are at different thicknesses. If two materials have the same defect concentration, but a different thickness, light will transmit through different volumes and encounter a different number of total defects. However, the darker color in the ESRO10 sample is likely due to absorption processes because ideally transparent media show color via absorption processes.

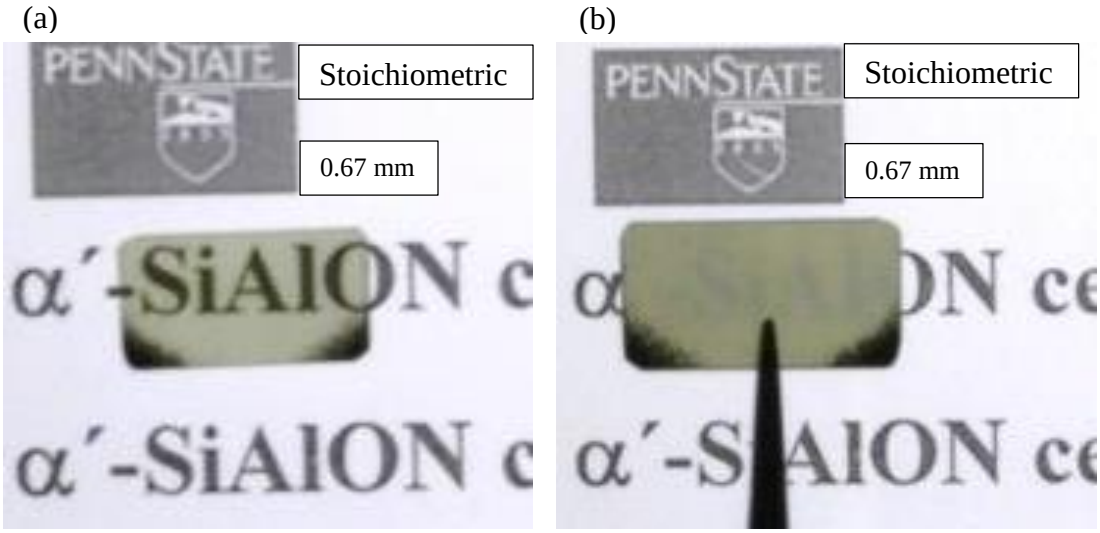


**Figure 3.14 – The light transmission of the preliminary stoichiometric sample. Relatively higher in-line transmission is seen in samples with clearer text when placed above the backlit light. (a) The sample is placed directly on a backlit background. (b) The sample is 10 cm above the backlit background. The camera is 64 cm above the background text.**

Figure 3.16 shows the optical quality of the EY samples. All EY samples have relatively the same optical quality when placed directly on the backlit background. The text can barely be seen in EY5 and EY20 when placed 10 cm above the background text. Also, the EY20 sample is darker and thinner than the EY5 sample which may indicate the presence of more absorption in the sample. The EY10 sample shows improved transmission when placed 10 cm above the backlit background with respect to the stoichiometric sample. The stoichiometric sample and EY10 sample are directly comparable because they have similar thicknesses which means light will transmit through the same volume of material. Thus, the EY10 sample may show a better

in-line transmission than the stoichiometric sample due to less scattering because the textual contrast is higher.

Figure 3.17 shows the optical quality of the AD samples. All AD samples show relatively the same optical quality when placed directly on the backlit background. The AD10 samples are shown at 2 different thicknesses to allow comparisons with other samples. Even at a 0.85 mm thickness, the AD10 sample shows better textual contrast than the stoichiometric sample. The AD20 sample shows somewhat better textual contrast than the stoichiometric sample, but less than the AD10 samples. Similar to the ESRO10 and EY20 samples, the darker color and spot formation is likely the result of absorption processes.

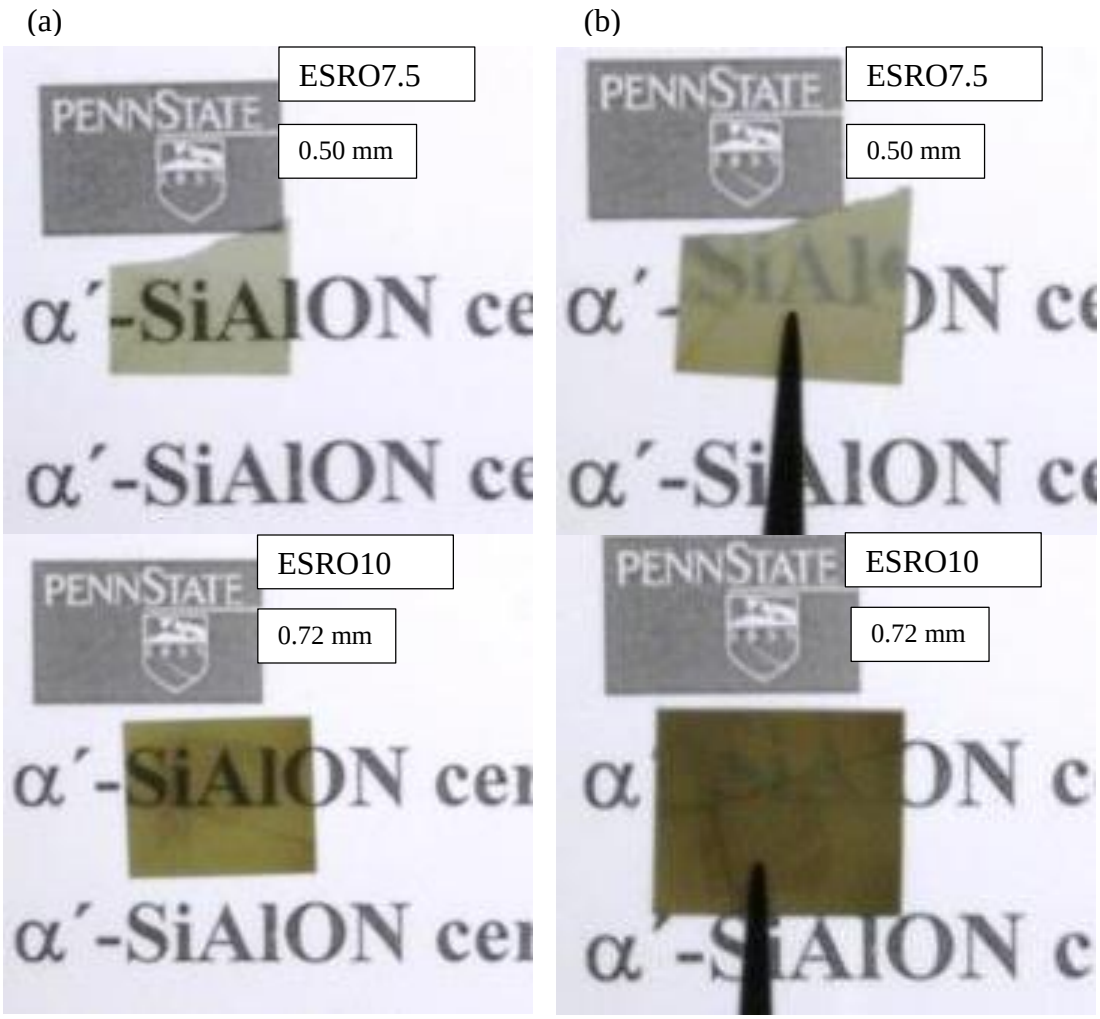


**Figure 3.15 – The light transmission of the ESRO samples. Relatively higher in-line transmission is seen in samples with clearer text when placed above the backlit light. (a) The sample is placed directly on a backlit background. (b) The sample is 10 cm above the backlit background. The camera is 64 cm above the background text.**

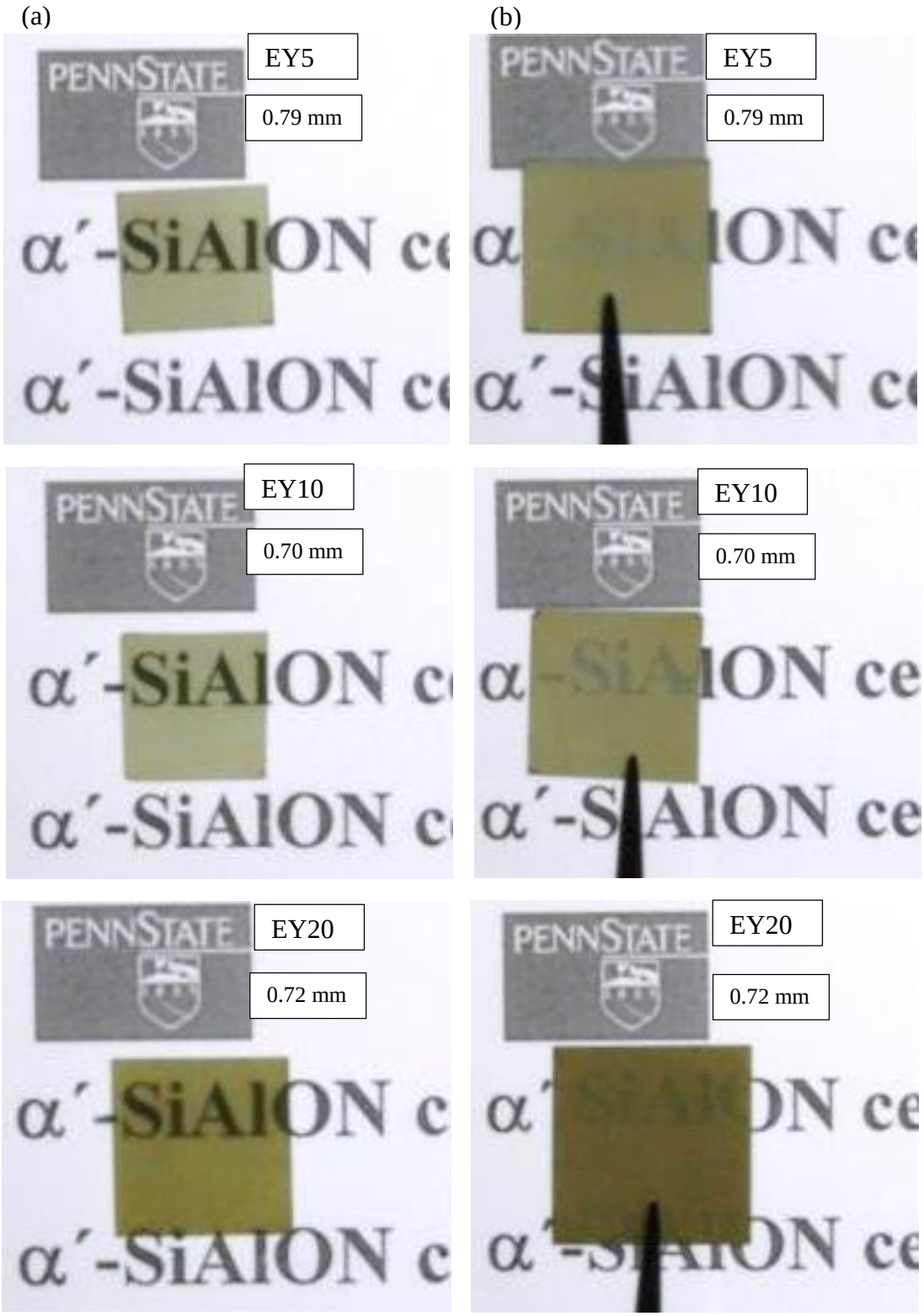


**Figure 3.16 – The light transmission of the EY samples. Relatively higher in-line transmission is seen in samples with clearer text when placed above the backlit light. (a) The sample is placed directly on a backlit background. (b) The sample is 10 cm above the backlit background. The camera is 64 cm above the background text.**

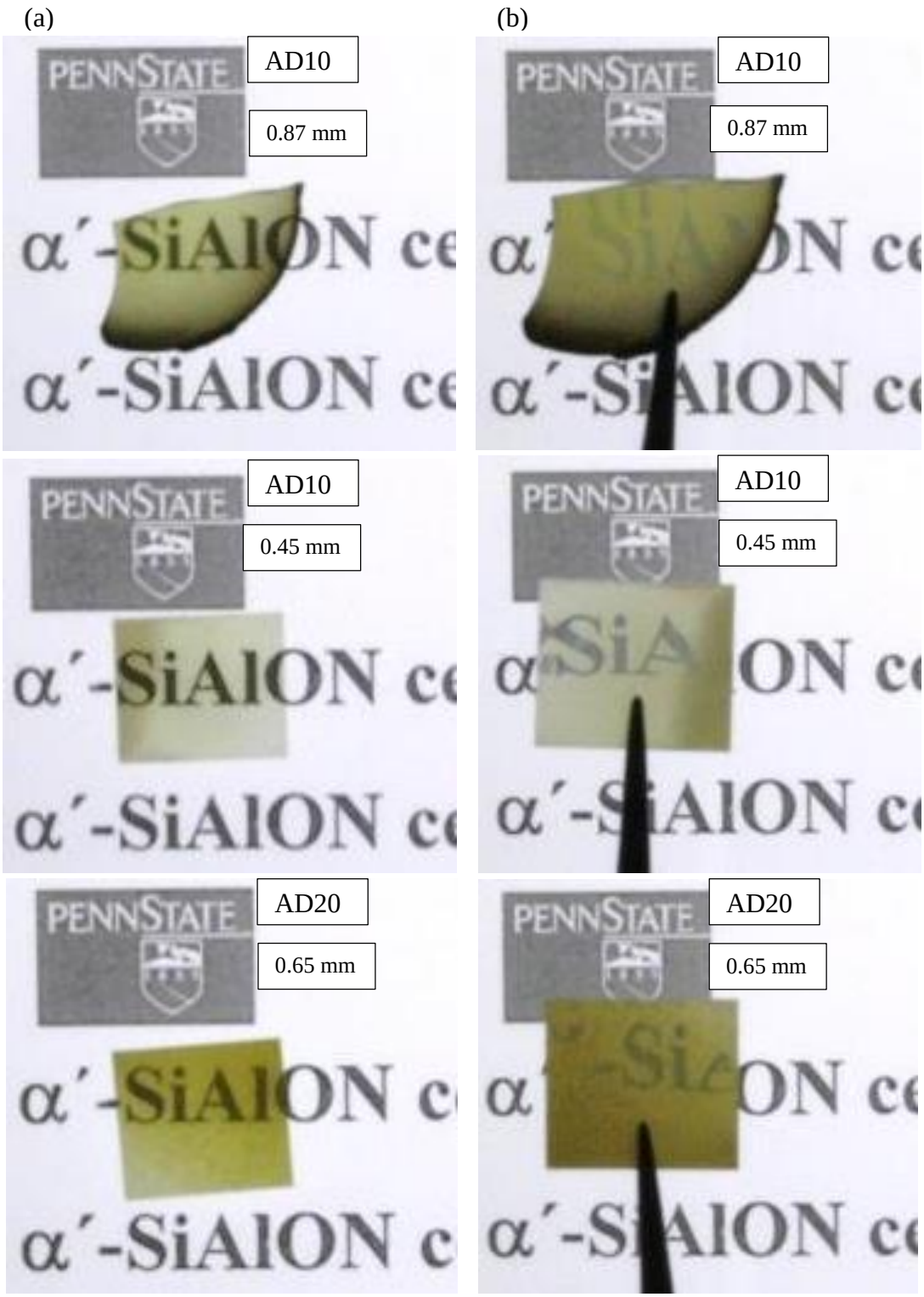


**Figure 3.17 - The light transmission of the AD samples. Relatively higher in-line transmission is seen in samples with clearer text when placed above the backlit light. (a) The sample is placed directly on a backlit background. (b) The sample is 10 cm above the backlit background. The AD10 samples have a slight curvature which is causing the text to warp. The camera is 64 cm above the background text.**

As the above images only provide a qualitative understanding, UV-visible spectroscopy was used to further understand the effects of each compositional change and the optical properties of the samples. Figure 3.18 shows the total forward transmission of each sample series with the baseline stoichiometric sample. The data in figure 3.18 is normalized to the sample thickness by rearranging eq. 3.3 to make eq. 3.4:

$$Total\ Transmission = T_{th}e^{(-\gamma d)} \quad \text{eq. 3.3}$$

$$P_{th} = \frac{Total\ Transmission^{\frac{1}{d}}}{T_{th}^{\frac{1}{d}}} = e^{-\gamma} \quad \text{eq. 3.4}$$

$$P_{th} * T_{th} = Normalized\ Transmission \quad \text{eq. 3.5}$$

where $T_{th}$ is the theoretical transmission, $\gamma$ is the total loss coefficient, d is the thickness of the material and $P_{th}$ is the percent of the theoretical transmission. $\gamma$ has units of 1/distance, thus it is thickness independent and can be used to directly compare the transmission and absorption of all samples. As seen in Figure 3.18(a) and Figure 3.18(b), all samples in the ESRO and EY sample series result in a decrease in the total transmission over all wavelengths in the visible region with respect to the stoichiometric sample. The AD sample series show an initial increase and then a decrease with respect to the stoichiometric sample. Comparing the end member samples in Figure 3.18(d), EY20 and ESRO10 show very similar transmission properties, but AD20 shows somewhat higher transmissions at higher wavelengths (>450 nm). The highest normalized transmission found at $\lambda$=800 nm was ≈60% in the AD10 sample.

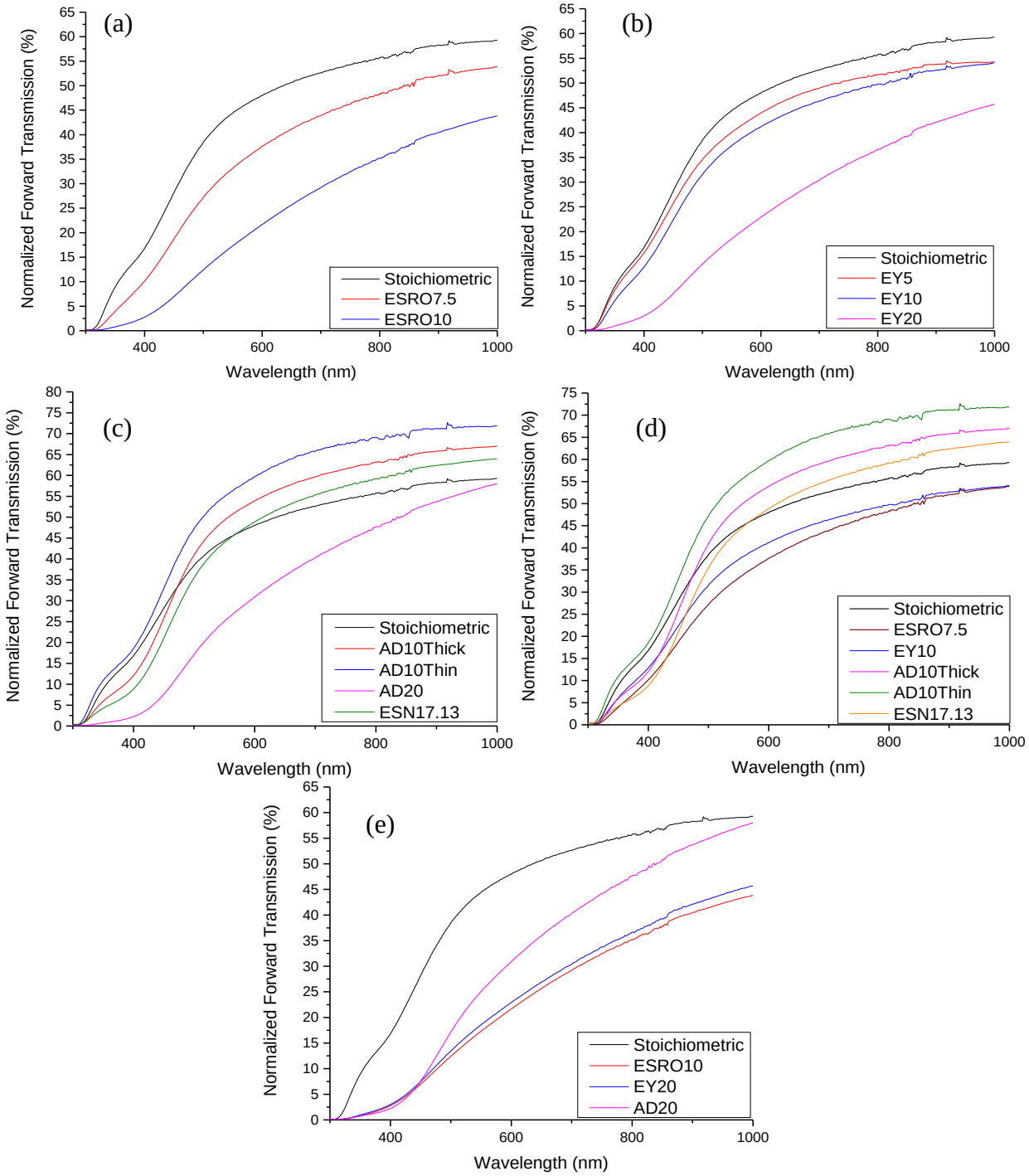


**Figure 3.18– UV-Visible Transmission data for each sample series compared to the stoichiometric sample. (a) ERSO7.5 and ESRO10 samples. (b) EY5, EY10, and EY20 samples. (c) AD10Thick, AD10Thin, AD20, and ESN17.13 samples. (d) Compares the compositions with the best transmission from each composition series. (e) Compares the end member samples. All data was normalized to the thickness of the samples using eq. 3.5.**

The UV-Visible analysis shows differences with the qualitative analysis performed above. Though the EY10 sample has a similar thickness as the stoichiometric sample and shows better textual contrast in the qualitative analysis, the transmission data in Figure 3.18(b) shows that the EY10 has a lower total transmission. A similar observation is seen with the AD20 sample. It is possible that the sample surfaces are not perfectly flat which results in distortion of what is seen qualitatively. The AD20 sample does have a small variation in thickness, but the text itself does not appear to be distorted significantly except at the edge. There does not appear to be a significant amount of distortion in the image text of the stoichiometric and EY10 sample as well. Another possibility is that the total transmission at all wavelengths is being reduced due to absorption events, but the amount of scattered light decreased. However, this could not be conclusively verified using the techniques utilized in this study. Finally, Figured 3.18 (c) shows the AD10 sample compositions have different transmissions even when the data is normalized to thickness. Considering the vacuum atmosphere the materials were sintered in and that significant decomposition occurred around the surface, it is likely that there is a change in the defect concentration as the thickness is decreased.

Comparing the ESRO, EY, and AD sample series to the table 3.2, a distinct correlation could not be determined between the light transmission and the AlN-polytypoid vol% using the quantitative data and qualitative image contrast. For instance, the ESRO7.5 and the AD10 samples are 0.5 mm and 0.45 mm thick, respectively, and qualitatively show similar optical transmission, but the ESRO7.5 and AD10 samples have 1.75 vol% and 0.11 vol% AlN-polytypoids in their microstructures, respectively. The quantitative data does show an increase in transmission in the AD10 sample, but not necessarily because there is a decrease in the AlN-polytypoid concentration. The EY composition series show an increase and then decrease in the

AlN-polytpoid concentration, but the quantitative analysis shows a continuous decrease in the light transmission. Additionally, the ESRO10 and EY20 samples have 2.3 vol% and 0.5 vol% AlN-polytypoids in their microstructure respectively, but the total forward transmission are very similar and much lower than the rest of sample compositions. These comparisons suggest that AlN-polytypoids are not acting as the dominant light scattering source in the α'-SiAlON ceramics. However, this study cannot conclusively say that the AlN-polytypoids do not scatter visible light, but it is concluded that another light scattering mechanism(s) may dominate.

The attempts to remove the AlN-polytypoids resulted in increasing the amount of residual glass as the composition diverges further from stoichiometry as seen by the increase in the white phase of Figures 3.7, 3.8, and 3.9. Coon *et. al.* showed that the refractive index of Y-SiAlON glasses varied from ≈1.74 to ≈1.85 depending on the yttrium and nitrogen concentration.[33] Though Liu *et al.*'s results for the refractive index of α'-SiAlON may be inaccurate, they are close enough to the real value to understand that the Y-SiAlON amorphous glass phase and α'-SiAlON have at least ≈0.2 refractive index difference. Thus, the residual Y-SiAlON amorphous glass phase likely results in more scattering as the concentration increases. The UV-visible data is in agreement with this logic as it shows that for almost all samples as the composition became less stoichiometric, there was a decrease in the overall light transmission. Using the same method as with the AlN-polytypoids, the concentration of residual glass in the ESRO10, EY20 and AD20 was determined to be 2.2 vol%, 2.5 vol% and 2.9 vol%, respectively. If the glass phase was the sole determining scattering source, then Figure 3.18(d) would show a continuous decrease for each sample. However, the AD20 sample has a higher transmission than the other extreme samples. Additionally, scattering does not explain why the extreme samples become "darker" and the AD20 and EY10 samples have better textual contrast than the stoichiometric

sample. Other potential absorption and scattering sites may be introduced into the microstructure due to free Si formation from the thermal decomposition of the $Si_3N_4$:[34]

$$Si_3N_4(s) \rightarrow 3Si(l) + 2N_2(g) \qquad \text{eq. 3.6}$$

$Si_3N_4$ or oxynitride decomposition is aided through SiO gas volatilization according the reactions below:[35]

$$Si_3N_4(s) + 3SiO_2(s) \rightarrow 6SiO(g) + 2N_2(g) \qquad \text{eq. 3.7}$$

$$3Si_2N_2O(s) \rightarrow Si_3N_4(s) + 3SiO(g) + N_2 \qquad \text{eq. 3.8}$$

$$Si_3N_4(s) + Y_2O_3(s) \rightarrow 2Y(l) + 3SiO(g) + 2N_2 \qquad \text{eq. 3.9}$$

$$(Y, Si, Al)_x(O, N)_y(l) \rightarrow SiO(g) + N_2 + (Y - containing\ compound) \qquad \text{eq. 3.10}$$

Eq. 3.5 accounts for the dark rims seen on the outside of all samples in this study. Herrmann and Goeb found that gray and black color in $Si_3N_4$ ceramics were caused by Si and silicide formation.[36] Considering the above reactions and that all samples were sintered under a vacuum, it is possible that the dark color or visible spots of low transmission seen in the ESRO10, EY20 and AD20 samples are caused by free Si and silicide (e.g. iron silicide due to Fe impurities) formation which are aided by Eq. 3.6, 3.7, 3.8 and 3.9. As $\gamma$ from eq. 3.3 represents the total light transmission losses in the material, independent of thickness, it will inherently contain information on any absorption processes. Figures 3.19 (a), 3.19 (b), and 3.19 (c) show plots of $\gamma$ vs wavelength that was calculated from eq. 3.3 for all sample compositions. The peak around 300 nm to 320 nm is consistent with the absorbance peaks reported for Si.[37; 38] The peak becomes more pronounced and red shifts as the residual glass phase increases, indicating an increase in Si grain size. Based on the above data, it is seen that the glass phase does scatter

light, particularly in the extreme samples, but absorption may contribute to a significant amount of loss as well. Though not conclusive, this may explain why the EY10 sample shows better visual contrast (due to less scattered light), but the overall transmission is lower. Considering that the AD20 sample has a higher residual glass content and better transmission compared to the ESRO10 and EY20 samples at $\lambda > 450$nm suggests that the residual amorphous may not be a dominant scattering source for these ceramics except at high concentrations (>2 to 3 vol%). If the AlN-polytypoid and the residual glass phase are not the dominant light scattering source, other scattering sources must be considered such as birefringence.

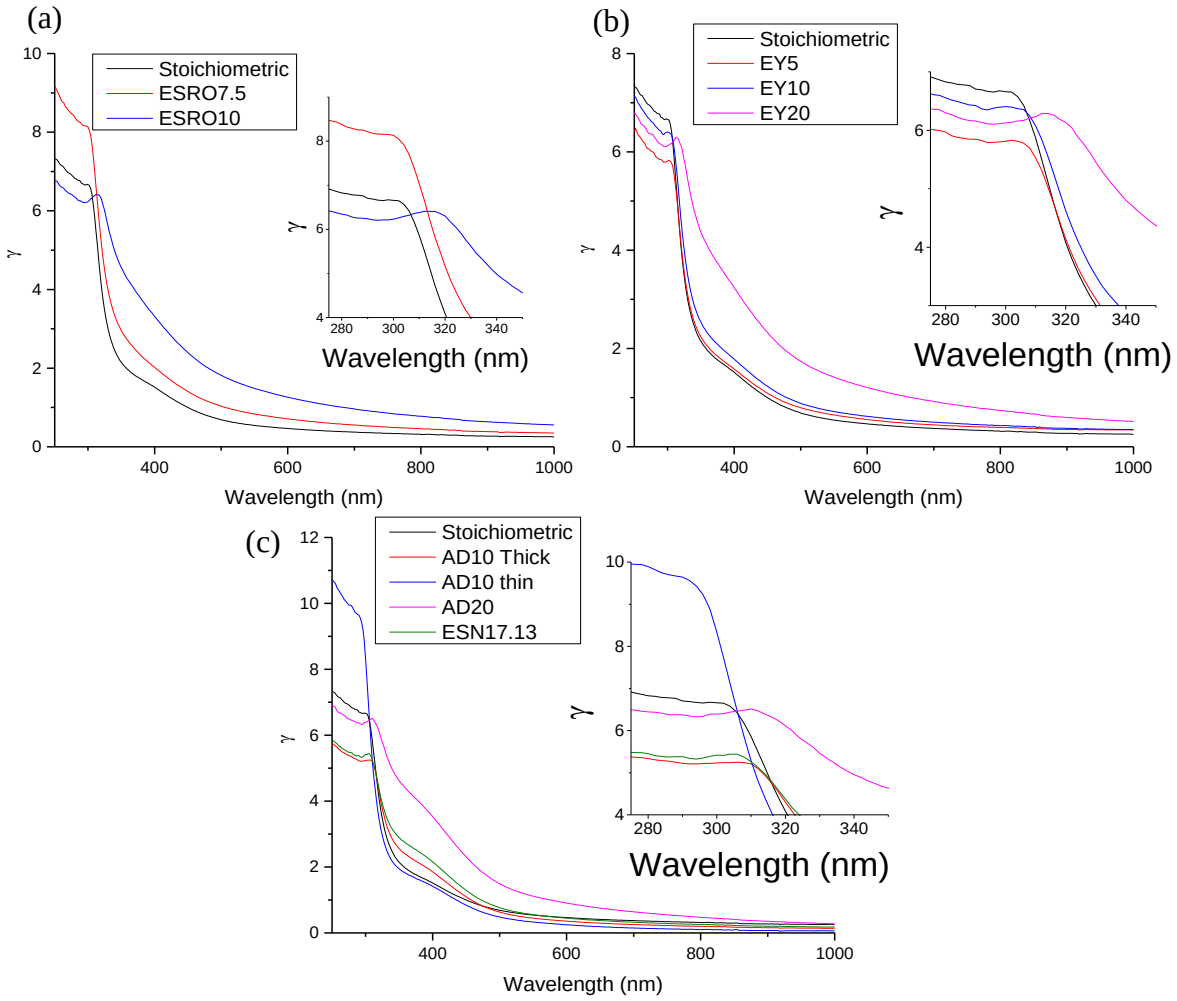


**Figure 3.19 – γ vs wavelength plots calculated from eq. 3.3 for (a) the ESRO, (b) EY (c) AD and ESN compositions. All samples contain a peak around 300 nm which is attributed to free Si. Inserts in each graph enlarge the area around the peaks.**

### 3.3.3 Effect of Birefringence on Visible Light Transmission in α'-SiAlON Ceramics

Apetz and van Bruggen developed a light scattering model which determines the real in-line transmission in a material based on the theoretical transmission ($T_{th}$), the grain size (2r), the thickness (d), the refractive index difference (Δn), and the wavelength of light in air ($\lambda_o$) as show below:

$$\text{RIT} = T_{th} \exp\left(-\frac{3\pi^2 \Delta n^2 r d}{n^2 \lambda_o^2}\right) \qquad \text{eq. 3.10}$$

Thus, to understand the relationship between birefringent scattering and the optical transmission, the grain size of the ESRO, EY, and AD samples was analyzed. Table 3.3 compares the ESRO, EY, AD, and ESN (discussed below) samples' grain sizes via the lineal intercept method. Most samples show a very small change in the grain size. The AD samples show the most significant change in the overall grain size. Because the ESRO and EY samples only have excess residual amorphous glass phase, it is believed that the change in the α'-SiAlON grain size is kinetically limited. The AD10 and AD20 samples contain 7.6 wt% and 15.6 wt% excess α-$Si_3N_4$ which can act as nucleation sites for α'-SiAlON. Thus, the AD samples' grain sizes are likely smaller because of an increase in nucleation frequency.

| Sample Series | Sample | Average Grain Size (μm) |
|---|---|---|
| Stoichiometric | | 1.23 |
| ESRO | | |
| | 7.5 | 1.01 |
| | 10 | 0.95 |
| EY | | |
| | 5 | 1.00 |
| | 10 | 0.93 |
| | 20 | 0.88 |
| AD | | |
| | 10 | 0.91 |
| | 20 | 0.83 |
| ESN | | |
| | 17.13 | 0.77 |

**Table 3.3 – Grain Size of all samples measured via the lineal intercept method.**

There may be a correlation between the sample grain size and the optical transmission of each sample series, but the introduction of different scattering sites or greater absorption may obscure this improvement in the transmission data. For the ESRO7.5, ESRO10, and EY5 samples, the grain size change is very small and well within error of the lineal intercept technique. Thus, a significant change or an increase in the light transmission is not expected.

The AD10 sample does have a small, but significant change in grain size (≈0.91 μm) with respect to the stoichiometric sample. Also, there is a marked improvement in the overall transmission with respect to all other samples. If birefringence is the dominant scattering source, then the EY10 and AD10 samples would have similar optical properties because their grain sizes are similar. However, the EY10 sample also contains more glass content based on the BSEM images and potentially more absorption. Thus, the EY10 sample can have a lower total transmission, but similar amounts of scattering still occur in the sample. Additionally, the AD20 sample has a marked change in the grain size to 0.83 μm and shows better visual contrast, but similar to the EY10 sample, more absorptions from free Si and other scattering sites may lower the total transmission. Based on these comparisons, birefringence may be a dominant scattering source. To test this hypothesis, AD samples were seeded to reduce the grain size.

#### 3.3.3.1 α'-SiAlON Grain Size Control by α-$Si_3N_4$ Seeding

Based on the observations seen in the AD10 and AD20 samples and the model proposed by Kumagai *et. al.* in eq. 3.1, if α-$Si_3N_4$ heterogeneously nucleates α'-SiAlON grains, then an increase in the α-$Si_3N_4$ particle concentration should result in a subsequent decrease in the grain size. In Rosenflanz *et. al*.'s study to reduce the grain boundary phase in α'-SiAlON ceramics, they demonstrated that the ceramics can tolerate >20 wt% excess $Si_3N_4$ and >10 wt% excess AlN without reducing the relative density of the ceramic.[32] Thus, the grain size may be tailored using the wide range of excess α-$Si_3N_4$. As discussed for the nucleation of AlN-polytypoids, larger particles in the α-$Si_3N_4$ particle size distribution act as the nucleation sites for α'-SiAlON formation. Thus, to predict the grain size possible with the commercial $Si_3N_4$ powder used in this study, the α-$Si_3N_4$ particle size distribution was measured as shown in Figure 3.20.

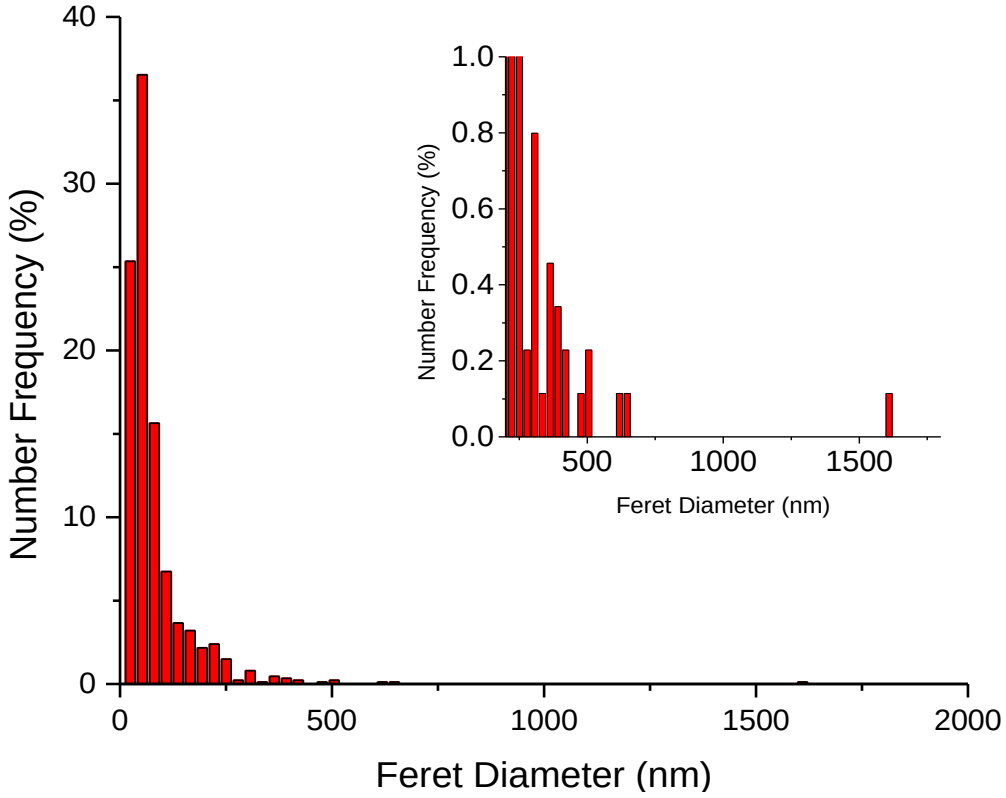


**Figure 3.20 – $Si_3N_4$ powder size distribution of 876 particles analyzed using SEM. The insert shows a magnified image so that particles above 450 nm can be easily seen.**

The distribution has a long tail with particles much larger than the mean size. Figure 3.21 shows images of some of the finer and larger particles in the $Si_3N_4$ powder. Though, the particle size distribution shows large particles in the distribution, it does not directly give an indication of the minimum α-$Si_3N_4$ nuclei size.

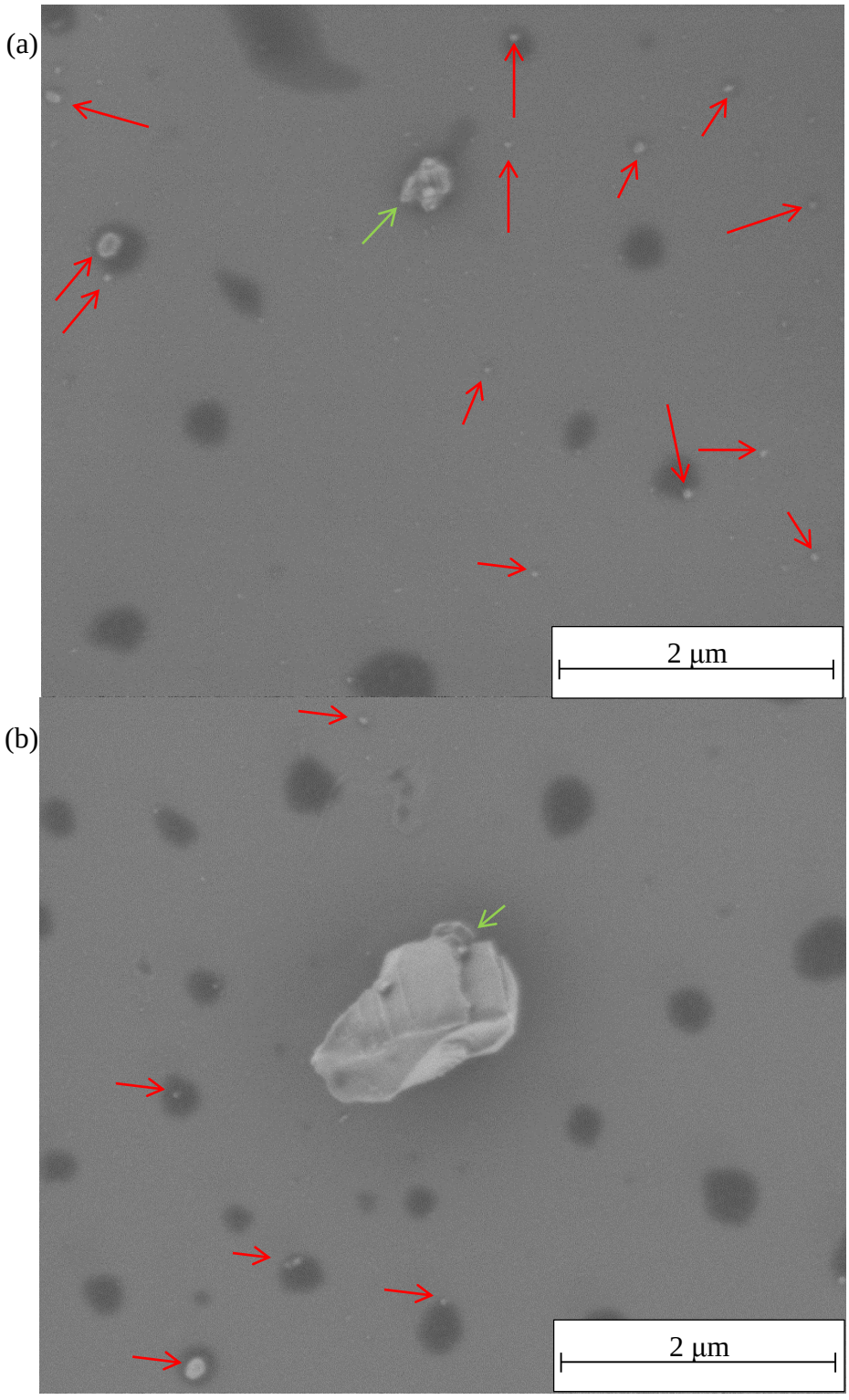


**Figure 3.21 – FESEM images of the $Si_3N_4$ particles. Light gray areas are the $Si_3N_4$ particles. (a) Showing finer particles. (b) Showing a particle >1 µm in size. Red arrows indicate finer particles while green arrows indicate large particles. The black areas are caused by MFO drying on the surface.**

Two approaches were used to determine the nuclei size. In the first approach, the size of $Si_3N_4$ grains at the core of the α'-SiAlON grains was determined using a modified lineal intercept method. The area of each core was used to calculate an equivalent spherical diameter. Figure 3.22 shows the obtained distribution of core sizes from the AD10 sample. A mean size of 265 nm was calculated from the distribution. Because the 265 nm size is based on random sectioning through the cores, the average core size was determined by multiplying the mean of the core distribution by 1.5, the same multiplication factor used for the lineal intercept method. Thus, the average core size was ≈400 nm.

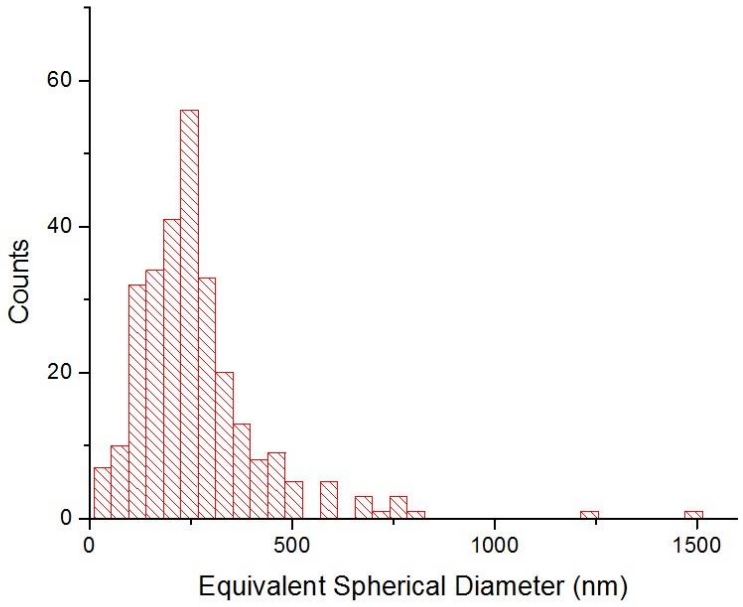


**Figure 3.22 – Distribution of core sizes as determined from polished surfaces on AD10. The areas were determined using BSEM images on imageJ software and the size is the equivalent spherical diameter. The sizes shown are not necessarily the true size of the core since a polished surface creates a random 2D slice through the core. The presence of cores up to 1500 nm further verifies that particles exist up to that size and seed the microstructure.**

The second method correlates the α'-SiAlON grain size and the α-$Si_3N_4$ particle size distribution. First, the method assumes that 1 α'-SiAlON grain is seeded by 1 α-$Si_3N_4$ particle

and that the number of α'-SiAlON grains per area is equal to the number of α'-SiAlON grains per volume. If the particle size distribution is normalized to a volume of 1 micron$^3$, then the minimum nuclei size can be found by summing the frequency of the largest particles in the α-$Si_3N_4$ particle size distribution so that the sum is equal to the number of α'-SiAlON grains per micron$^3$ in the sample. Table 3.4 shows the number of grains per micron$^3$ for the stoichiometric and AD10 sample with the resulting nuclei size. Both methods resulted in an α-$Si_3N_4$ nuclei size of approximately 400 nm to 500 nm.

| Sample | Grains per Micron$^3$ | Nuclei Size |
|---|---|---|
| Stoichiometric | ≈1.67 | ≈475 nm |
| AD10 | ≈2.52 | ≈400 nm |

**Table 3.4 – The number of grains counted in polished samples of the stoichiometric and AD10 samples. The number of grains was counted for an area of ≈200 μm$^2$. The seed size was determined by normalizing the $Si_3N_4$ powder distribution to 1 micron$^3$ and summing the frequency to an equivalent number of particles.**

Using eq. 3.10, the grain size at which birefringent scattering becomes negligible was obtained by assuming $\lambda$ = 400nm, $\Delta n$ = 0.006, d = 1 mm, n = 2.15, and $T_{th}$ = 76.5. The n, $\Delta n$, and $T_{th}$ were averaged from Liu *et. al.*'s calculated and measured values.[21] Assuming that the grains are randomly oriented, the refractive index difference between two grains is not always the maximum value. Statistically, the refractive index difference equals two thirds of the maximum difference in a randomly oriented microstructure.[39] Though the values measured by Liu *et. al.* may be inaccurate, they can still be used as an estimation for this calculation. A grain size of ≈100nm is needed to effectively make birefringent scattering negligible. Based on the α-$Si_3N_4$ nuclei size that was calculated above, it is impossible to obtain this grain size from the α-$Si_3N_4$ commercial powder. Instead, a more reasonable goal of 0.7 μm, the edge of the visible light spectrum, was used to demonstrate the principle of seeding α'-SiAlON with excess α-$Si_3N_4$.

Using eq. 3.1 and the grain size difference between the stoichiometric and AD10 sample, the amount of excess α-$Si_3N_4$ needed to obtain 0.7 μm was determined to be 17.13 wt% excess with respect to the sample weight. The calculation assumes that the nuclei size determined in the stoichiometric and AD10 samples is independent of the amount of excess $Si_3N_4$. The composition of ESN17.13 was determined using the above calculation. The sample uses the composition of AD10 as the starting point and adds only excess $Si_3N_4$ so that no more excess residual amorphous glass phase is added to the microstructure. AD10's composition was chosen for 2 reasons. First, AD10 had the minimum amount of AlN-polytypoids without adversely affecting the light transmission. Second, the sample has excess residual amorphous glass phase which is needed to densify a sample with excess $Si_3N_4$. Figure 3.23 shows the model of eq. 3.1 using a 400 nm nuclei size with the stoichiometric, AD10, and ESN17.13 (discussed below) samples' grain size and nuclei number plotted on the graph. The grain size in the samples is larger than the model prediction because of the presence of nuclei much greater than the average grain size. However, there is still reasonable agreement between the average grain size and the -1/3 slope of the model. The -1/3 slope is found when eq. 3.1 is represented as a log-log plot of the grain size vs the nucleation frequency.

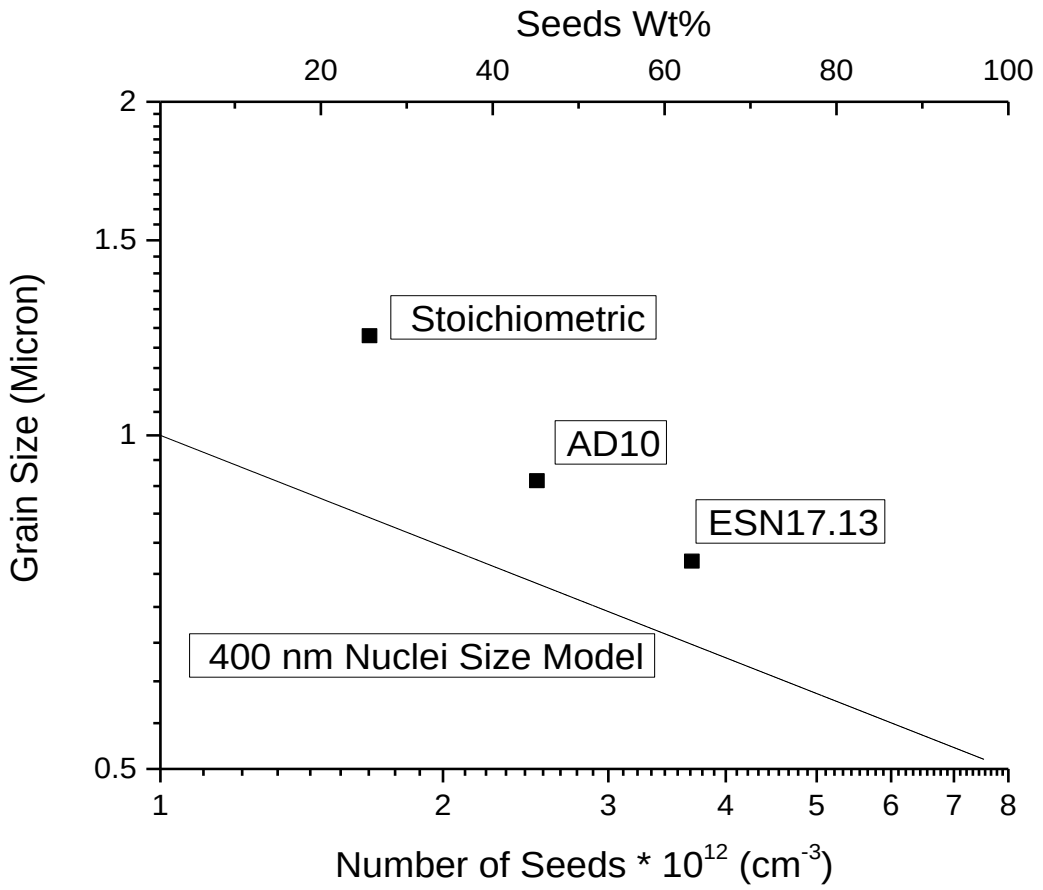


**Figure 3.23 – Grain size vs number of seeds showing the grain size of the stoichiometric, AD10 and ESN17.13 samples. The model from eq. 3.1 assuming a 400 nm nuclei size is also plotted to compare the slope with that of the grain size changes in the samples. The seed wt% is determined from the model calculation.**

Figure 3.24(a) and Figure 3.24 (b) show the microstructure of the ESN17.13 sample. The average grain size calculated by the lineal intercept method was 0.77 μm. AlN-polytypoids were not detected in the samples using BSEM and EDS. However, free particles of α-$Si_3N_4$, β-$Si_3N_4$, or β-SiAlON were found as secondary phases which did not appear to act as seeds. It was not possible to verify conclusively the phase the particles were using the techniques of this study. BSEM cannot distinguish due to the absence of a contrast mechanism between each. EDS may detect Al in the particles, but that could be due to α'-SiAlON grains below. It is likely that all three phases are present because the nominal composition of ESN17.13 lies nearly directly above the α'/β' –SiAlON boundary on the α'-SiAlON plane. Using the same method as used on the

AlN-polytypoid vol% measurement, the concentration of potentially non-seeding particles was ≈0.73 vol%. Figure 3.24(b) shows the XRD pattern of the sample. The absence of an AlN-polytypoid verifies the results of the BSEM and EDS analysis. The grain size is close to the prediction made using eq. 3.1 and the grain size change between the stoichiometric and AD10 samples. The sample demonstrates the importance of the larger particle nuclei in the $\alpha$-$Si_3N_4$ particle size distribution because these particles limit the obtainable grain size. Figure 3.25 shows the qualitative transmission of the ESN17.13 sample using the same method as the other samples in this study. Figure 3.18(c) shows the UV-Vis of the ESN17.13 sample. The sample shows better optical transmission than the stoichiometric sample, but inferior transmission relative to the AD10 samples. As the sample appears to have stronger color and has a more defined absorption peak in Figure 3.19 (c) than AD10, it is probable that excess free Si lowers the overall transmission in this sample with respect to AD10. Thus, even if the scattering is reduced by decreasing the grain size, other losses could not be avoided using this method. Based on the ESN17.13 sample and the previous results, it is believed that birefringence and absorption are the dominant sources of transmission loss. The amorphous phase likely becomes a dominant scattering source when the amorphous phase concentration becomes too large (> 2-3 vol%), but the relative contributions to the transmission loss of each source are unknown.

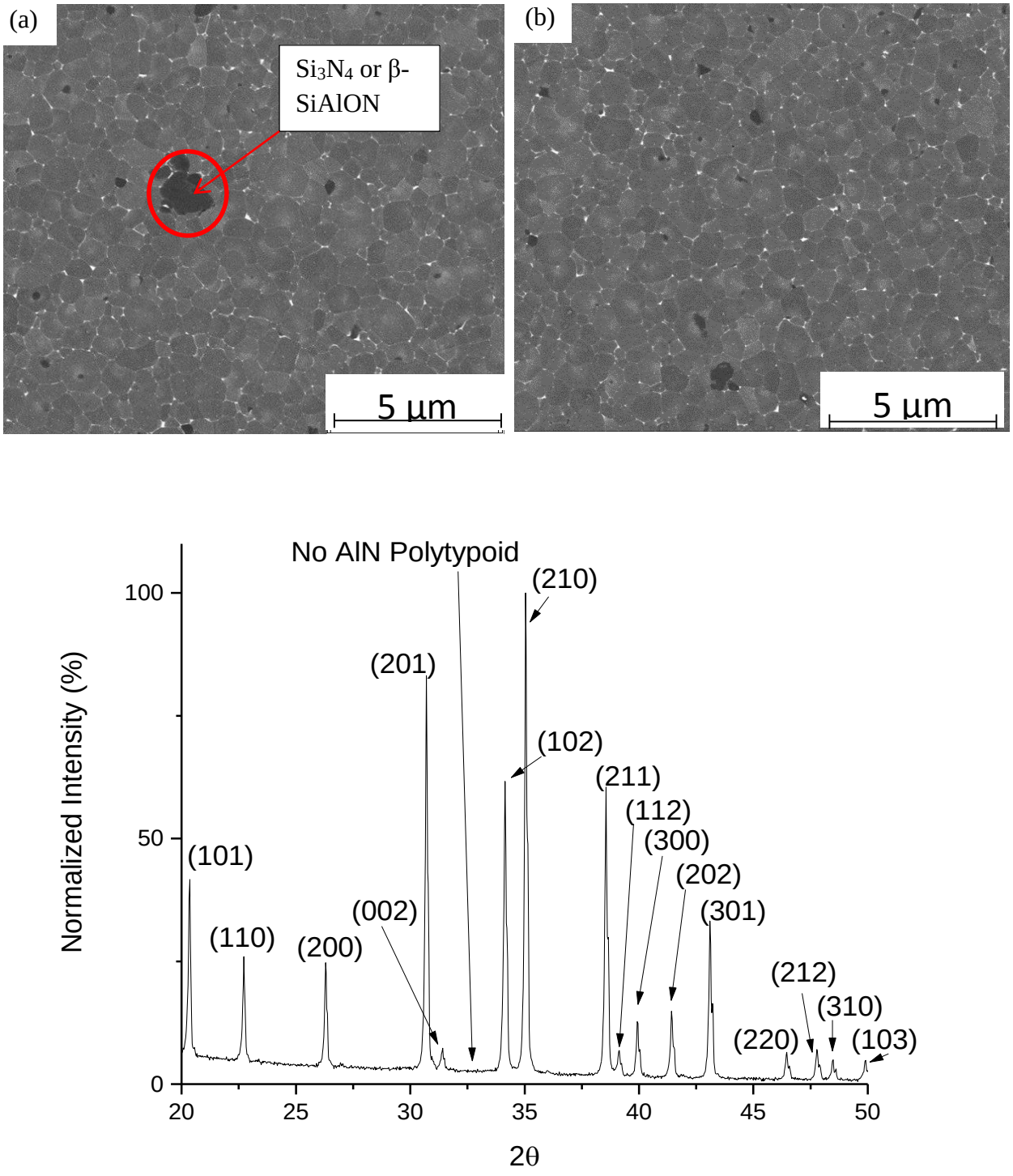


**Figure 3.24 – (a) and (b) BSEM image of the ESN17.13 sample. The microstructure only contains α'-SiAlON as the primary phase while α-$Si_3N_4$/β-$Si_3N_4$/β-SiAlON and amorphous glass were secondary phases. (b) XRD pattern of the ESN17.13 sample.**


**Figure 3.25 - The light transmission of the ESN17.13 sample. Relatively higher in-line transmission is seen in samples with clearer text when placed above the backlit light. (a) The sample is placed directly on a backlit background. (b) The sample is 10 cm above the backlit background. The camera is 64 cm above the background text.**

Another possibility exists for the limited grain size reduction. The efficiency at which $Si_3N_4$ particles become seeds is rather low considering that a single batch consists of ≥75 wt% $Si_3N_4$. Considering the distribution of particle sizes (though the number of 400 nm+ particles was well below a statistical value), only 40% of the potential nuclei actually nucleated α'-SiAlON. The number may not be accurate, but it does demonstrate the complexity of the seeding process. Many of the particles are expected to fully dissolve into the liquid phase because the largest particles also provide most of the mass for the system. The competition between nucleation and dissolution may explain the rather low nucleation density. However, consumption of the powder for the formation of α'-SiAlON is not the only reason. The reaction sequence for forming α'-SiAlON may also differ from the sequence discussed in chapter 2 due to an unaccounted reaction or impurity which affected the wetting characteristics of the nitride particles. Though Y-α'-SiAlON should preferentially wet and react with AlN, an interruption run at 1300 °C and 1450 °C shows J'-SiAlON formed during sintering. As J' is a solid solution between YAM and J phase ($Y_4Si_2ON_2$), a reaction between the liquid phase or $Y_2O_3$ and $Si_3N_4$

must occur. By forming the J'-phase, the number of potential $Si_3N_4$ particle nuclei is reduced because of the conservation of mass. Thus, the seed concentration is now a complex function controlled by the composition, $Si_3N_4$ particle size distribution, and J'-phase formation. Figure 3.26 shows an XRD scan of the interrupted ESN17.13 sample sintering at 1450 °C for 1 h and the Figure identifies the J' phase peaks.

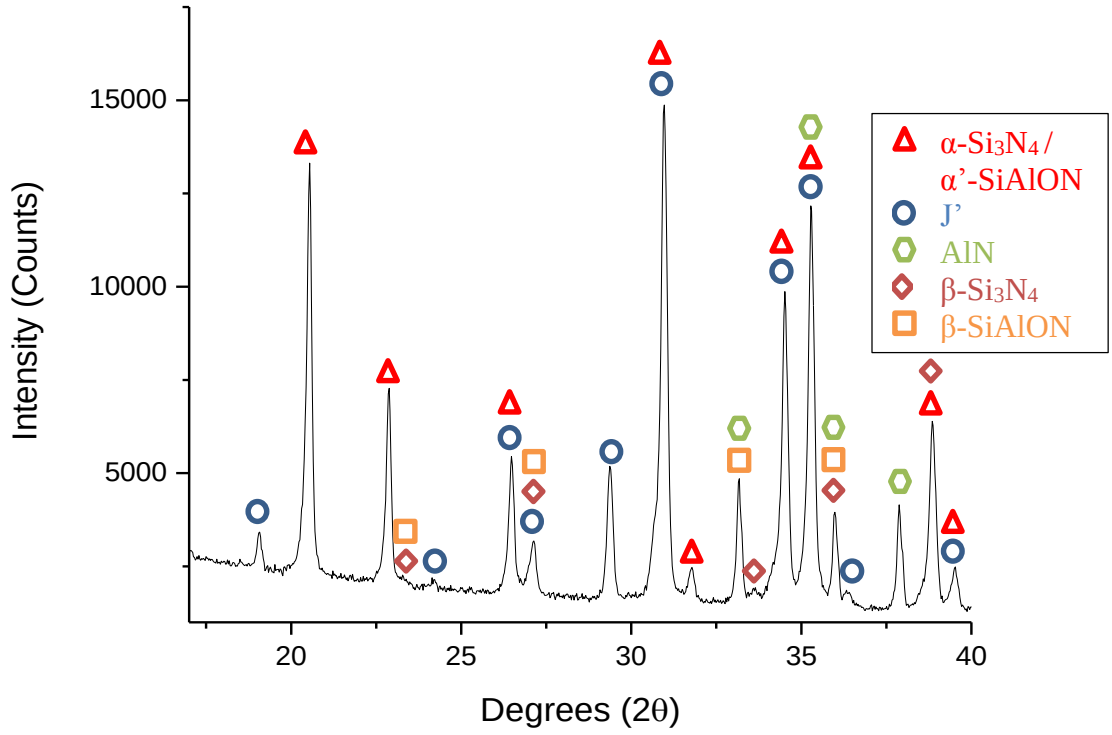


**Figure 3.26 – XRD pattern of ESN17.13 after sintering at 1450 °C for 1.**

## 3.4 Conclusion

A study of the contributing factors concerning phase purity and grain size control was performed. Compositional shifts from nominally stoichiometric α'-SiAlON were used to reduce the AlN-polytypoid concentration. The compositional shifts caused a decrease in grain size and an increase in the residual amorphous phase concentration. The following information was determined from the study:

- AlN-polytypoids were found to form due to heterogeneous nucleation and growth. AlN-deficient samples showed the largest decrease in AlN-polytypoid content due to the removal of nucleation sites from the system.
- No trend could be found between the AlN-polytypoid phase concentration and the light transmission. However, the study could not rule out the possibility of secondary phase scattering from the AlN-polytypoids or residual amorphous glass. Instead, these phases were only determined to not likely be the dominant light scattering source.
- An attempt to control and predict the nucleation frequency of α'-SiAlON using commercial α-$Si_3N_4$ powder was made. Adding excess α-$Si_3N_4$ resulted in a reduction of grain size, but was limited due to the large particle nuclei in the commercial powder. Though the prediction did not accurately predict the calculated grain size of 0.7 μm, there is very good agreement between the slope of the model and the change in grain size of the stoichiometric, AD10, and ESN17.13 samples. Based on the results, birefringent scattering and potential absorption from free Si are likely to be the dominant sources of transmission loss of the materials in this study. Finally, the nucleation density of α'-SiAlON is a complex function of the composition, α-$Si_3N_4$ particle size distribution, and secondary phase formation (if $Si_3N_4$ participates in its formation).

## 3.5 References


[1]B. S. B. Karunaratne, R. K. Lumby and M. H. Lewis, "Rare-Earth-Doped α'-Sialon Ceramics with Novel Optical Properties," *J. Mater. Res.*, **11,** [11] 2790-94 (1996).

[2]M. I. Jones, H. Hyuga and K. Hirao, "Optical and Mechanical Properties of α/β Composite SiAlONs," *J. Am. Ceram. Soc.*, **86,** [3] 520-22 (2003).

[3]R. Shuba and I.-W. Chen, "Refractory α-SiAlON Containing $La_2O_3$," *J. Am. Ceram. Soc.*, **89,** [9] 2860-68 (2006).

[4]A. B. Shinani, N. K. Dynkin, L. A. Lytvinov, P. V. Konesvky, and E. P. Andreev, "Sapphire Hardness in Different Crystallographic Directions," *Bull. Russ. Acad. Sci. Phys.*, **73,** [10] 1380-82 (2009).

[5]M. Iwasa, T. Ueno and R. C. Bradt, "Fracture Toughness of Quartz and Sapphire Single Crystals at Room Temperature," *J. Soc. Mater. Sci. Jpn.*, **30,** [337] 1001-04 (1980).

[6]J. W. McCauley, "Structure and Properties of AlN and AlON Ceramics," pp. 127-32. in Encyclopedia of Materials: Science and Technology**.** Elsevier Science, 2001.

[7]W.-W. Chen, X.-L. Su, P.-L. Wang, and D.-S. Yan, "Optical Properties of Gd-α-Sialon Ceramics: Effect of Carbon Contamination," *J. Am. Ceram. Soc.*, **88,** [8] 2304-06 (2005).

[8]M. I. Jones, H. Hyuga, K. Hirao, and Y. Yamauchi, "Highly Transparent Lu-α-SiAlON," *J. Am. Ceram. Soc.*, **87,** [4] 714-16 (2004).

[9]W. W. Chen, Y. B. cheng, P. I. Wang, and D. S. Yan, "Novel Optical Ceramics: α-Sialons," *Key Eng. Mater.*, **264-268,** 905-08 (2004).

[10]S. Kochawattana, A. Stevenson, S.-H. Lee, M. Ramirez, V. Gopalan, J. Dumm, V. K. Castillo, G. J. Quarles, and G. L. Messing, "Sintering and Grain Growth in $SiO_2$ doped Nd:YAG," *J. Euro. Ceram. Soc.*, **28,** 1527-34 (2008).

[11]W.-Y. Sun, T.-Y. Tien and T.-S. Yen, "Subsolidus Phase Relationships in Part of the System Si,Al,Y,/N,O: The System $Si_3N_4$-AlN-YN-$Al_2O_3$-$Y_2O_3$," *J. Am. Ceram. Soc.*, **74,** [11] 2753-58 (1991).

[12]K. H. Jack, "Review: Sialons and Related Nitrogen Ceramics," *J. Mater. sci.*, **11,** 1135-58 (1976).

[13]Y.-B. Cheng and D. P. Thompson, "Preparation and Grain Broundary Devitrification of Samarium α-SiAlON Ceramics," *J. Euro. Ceram. Soc.*, **14,** 13-21 (1994).

[14]X. Su, P. wang, W. Chen, Z. Shen, M. Nygren, Y. Cheng, and D. Yan, "Effects of Composition and Thermal Treatment on Infrared Transmission of Dy-α-SiAlON," *J. Euro. Ceram. Soc.*, **24,** 2869-77 (2004).

[15]A. L. Greer, "Confusion by Design," *Nature*, **336,** 303-04 (1993).

[16]S.-L. Hwang and I.-W. Chen, "Nucleation and Growth of β'-SiAION," *J. Am. Ceram. Soc.*, **77,** [7] 1719-29 (1994).

[17]S.-L. Hwang and I.-W. Chen, "Nucleation and Growth of α'-SiAlON on α-$Si_3N_4$," *J. Am. Ceram. Soc.*, **77,** [7] 1711-18 (1994).

[18]D. P. Thompson, "The Crystal Chemistry of Nitrogen Ceramics," *Mater. Sci. Forum*, **47,** 21-41 (1989).

[19]Y. Yan, m. terauchi and M. Yanaka, "Structures of Polytypoids in AlN Crystals Containing Oxygen," *Philosophical Magazine A*, **77,** [4] 1027-40 (1998).

[20]I.-L. Tangen, Y. Yu, T. Grande, R. Hoier, and M.-A. Einarsrud, "Phase Relations and Microstructural Development of Aluminum Nitride- Aluminum Nitride Polytypoid

Composites in the Aluminum Nitride-Alumina-Yttria System," *J. Am. Ceram. Soc.*, **87,** [9] 1734-40 (2004).
[21]L. Liu, F. Ye, S. Zhang, B. Peng, W. Luo, Z. Zhang, and Y. Zhou, "Light Transmittance in α-SiAlON Ceramics: Effects of Composition, Microstructure, and Refractive Index Anisotropy," *J. Euro. Ceram. Soc.*, **32,** 2487-94 (2012).
[22]X. Zhu, T. S. Suzuki, T. Uchikoshi, and Y. Sakka, "Texturing Ca-α-Sialon Via StrongMagnetic Field Alignment," *J. Cerm. Soc. Jpn.*, **115,** [11] 701-05 (2007).
[23]A. Caman, E. Pereloma and Y.-B. cheng, "Hot Forging of a Textured α-Sialon Ceramic," *J. Am. Ceram. Soc.*, **89,** [2] 478-83 (2006).
[24]C. J. Hwang, D. W. Susnitzky and D. R. Beaman, "Preparation of Multication α-SiAlON Containing Strontium," *J. Am. Ceram. Soc.*, **78,** [3] 588-92 (1995).
[25]Z. K. Huang, Y. Z. Jiang and T. Y. Tien, "Formation of α-SiAlON with Dual Modifying Cations (Li+Y and Ca+Y)," *J. Mater. Sci. Lett.*, **16,** 741-51 (1997).
[26]Z. J. Shen, L.-O. Nordberg, M. Nygren, and T. Ekstrom, "α-SiALON Grains with High Aspect Ratio − Utopia or Reality?," pp. 169-78. Engineering Ceramics '96: High reliability through Processing**.** Edited by G. N. Babini, M. Haviar and P. Sajgalik. Kluwer Academic Press, Netherland, 1997.
[27]M. Zenotchkine, R. Shuba, J.-S. Kim, and I.-W. Chen, "Effect of Seeding on the Microstructure and Mechanical Properties of α-SiAlON: I, Y-SiAlON," *J. Am. Ceram. Soc.*, **85,** [5] 1254-59 (2002).
[28]R. A. Shelleman, G. L. Messing and M. Kumagai, "Alpha Alumina Transformation in Seeded Boehmite Gels," *J. Non.-Cryst. Solids*, **82,** 277-85 (1986).
[29]Z. Shen and M. Nygren, "On the Extension of the α-SiAlON Phase Area in Yttrium and Rare-Earth Doped Systems," *J. Euro. Ceram. Soc.*, **17,** 1639-45 (1997).
[30]R. Shuba and I.-W. Chen, "Elimination of Grain Boundary Glass in α-SiAlON by Adding Aluminium Nitride," *J. Am. Ceram. Soc.*, **89,** [3] 1065-71 (2006).
[31]S.-L. Hwang and I.-W. Chen, "Reaction Hot Pressing of α'- and β'-SiAlON Ceramics," *J. Am. Ceram. Soc.*, **77,** [1] 165-71 (1994).
[32]A. Rosenflanz, "Glass-Reduced SiAlONs with Improved Creep and Oxidation Resistance," *J. Am. Ceram. Soc.*, **85,** [9] 2379-81 (2002).
[33]D. N. Coon and T. E. Doyle, "Refractive Indices of Glasses in the Y-Al-Si-O-N System," *J. Non.-Cryst. Solids*, **108,** [180-186] (1989).
[34]A. H. Heuer and V. L. K. Lou, "Volatility Diagrams for Silica, Silicon Nitride, and Silicon Carbide and Their Application to High-Temperature Decomposition and Oxidation," *J. Am. Ceram. Soc.*, **73,** [10] 2789-3128 (1990).
[35]T. Hayashi, H. Munakata, H. Suzuki, and H. Saito, "Pressureless Sintering of $Si_3N_4$ with $Y_2O_3$ and $Al_2O_3$," *J. Mater. Sci.*, **21,** 3501-08 (1986).
[36]M. Herrmann and O. Goeb, "Colour of Gas-Pressure-Sintered Silicon Nitride Ceramics Part I. Experimental Data," *J. Euro. Ceram. Soc.*, **21,** 303-14 (2001).
[37]M. A. Green and M. J. Keevers, "Short Communication: Optical Properties of Intrinsic Silicon at 300 K," *Progress in Photovoltaics: Research and Applications*, **3,** 189-92 (1995).
[38]J. P. Wilcoxon, G. A. Samara and P. N. Provencio, "Optical and Electronic Properties of Si Nanoclusters Synthesized in Inverse Micelles," *Phys. Rev. B*, **60,** [4] 2704-14 (1999).
[39]R. Apetz and M. P. B. v. Bruggen, "Transparent Alumina: A Light-Scattering Model," *J. Am. Ceram. Soc.*, **86,** [3480-486] (2003).

# Chapter 4

## Future Work

The goal of this thesis was to improve the optical transmission performance of α'-SiAlON ceramics and demonstrate a means for achieving theoretical transmission by studying the effects of the AlN-polytypoid concentration, amorphous glass concentration and birefringent scattering on visible light transmission. To achieve this goal, there are still many unexplored avenues which can help improve the understanding of α'-SiAlON ceramic processing and obtain optically transparent SiAlON.

As discussed in chapter 2, the refractive indices of the various SiAlON phases are not known. Determination of the refractive indices of the various phases would greatly enhance the knowledge of the effects of secondary phases in α'-SiAlON and all other SiAlON ceramics. This knowledge could lead to transparent composite microstructures or a better understanding of what phases will strongly scatter light in α'-SiAlON ceramics. Additionally, this study only provides a general understanding of the optical properties of α'-SiAlON. Further work is needed to verify the presence of free Si or silicides and to quantify the relative contribution of each source to the transmission loss.

In chapter 3, it was discussed that the formation of AlN-polytypoids and large α'-SiAlON grains occurred due to the broad and coarse particle size distributions of the respective nitride powders. Thus, using narrower and finer silicon nitride particle size distribution than that of the commercial powders in this study should result in a finer grain size and higher phase purity without utilizing compositional shifts. However, the commercial powders used in this study are currently the best available high purity powders. Thus, studies are needed for scaling the

processing required to obtain large batches of high purity α-$Si_3N_4$ and AlN powder with a smaller particle size and a narrower particle size distribution. Such a study would benefit not only the processing of α'-SiAlON ceramics, but all $Si_3N_4$ based ceramics.

In discussed in chapter 2, Hwang and Chen and Menon and Chen presented the reaction sequence for α'-SiAlON formation based on the wetting characteristics of the $Si_3N_4$ and AlN powders.[1-3] However, their work is not consistent with the reported phase evolutions for α'-SiAlON formation including the J' phase formation seen in this study. It is not well understood what causes the shift between different intermediate phases seen in different studies. If the wetting characteristics control the formation of the secondary phase and α'-SiAlON, then the factors controlling the wetting characteristics require investigation. However, based on the AlN-polytypoid formation in this study, heterogeneous nucleation may also affect the formation of the intermediate phase. Understanding what controls the intermediate phase formation may lead to the development of better processing routes for obtaining phase pure α'-SiAlON at lower sintering temperatures.

In chapter 2, it was discussed that Y-α'-SiAlON does not contain any characteristic absorption peaks. Li *et. al.* determined that the optical band gap for Ca-α'-SiAlON is 5.44 eV using diffuse reflectance spectroscopy which is well above the limit for visible light transmission.[4] However, except in very thin samples, all α'-SiAlON samples in this study contain some color. The band gap of translucent Y-α'-SiAlON should be measured to confirm whether the color is intrinsic or extrinsic. If the color is extrinsic, stronger absorption and color formation may occur due to the presence of free Si, silicides, or impurities.[5] Additionally, electronic defects such as vacancies created for charge balance for missing $O^{2-}$ ions and $N^{3-}$ ions

may cause the coloring in Y-α'-SiAlON. Determining the color formation mechanism will dictate the possible processing route needed to obtain clear α'-SiAlON ceramics.

## 4.1 References


[1]S.-L. Hwang and I.-W. Chen, "Reaction Hot Pressing of α'- and β'-SiAlON Ceramics," *J. Am. Ceram. Soc.*, **77,** [1] 165-71 (1994).

[2]M. Menon and I.-W. Chen, "Reaction Densification of α'-SiAlON: I, Wetting Behavior and Acid-Base Reactions," *J. Am. Ceram. Soc.*, **78,** [3] 545-52 (1995).

[3]M. Menon and I.-W. Chen, "Reaction Densification of α'-SiAlON: II, Densification Behavior," *J. Am. Ceram. Soc.*, **78,** [3] 553-59 (1995).

[4]Y.-Q. Li, N. Hirosaki, R.-J. Xie, J. Li, T. Takeda, Y. Yamamoto, and M. Mitomo, "Structural and Photoluminescence Properties of $Ce^{3+}$ - and $Tb^{3+}$ - Activated Lu-α-SiAlON," *J. Am. Ceram. Soc.*, **92,** [11] 2738-44 (2009).

[5]M. Herrmann and O. Goeb, "Colour of Gas-Pressure-Sintered Silicon Nitride Ceramics Part I. Experimental Data," *J. Euro. Ceram. Soc.*, **21,** 303-14 (2001).

# APPENDIX

## Commercial Powder Purity

The commercial high purity powders utilized in this study are among the most commonly used in the $Si_3N_4$, SiAlON, and transparent ceramic literature. Tables A-1, A-2, A-3, A-4, A-5, and A-6 show the typical chemical purities of the $Si_3N_4$, AlN, $Y_2O_3$, $Al_2O_3$, $SiO_2$, and BN powders, respectively, utilized in this study as provided by the companies. .

| UBE SN – E10 - $Si_3N_4$ Powder | |
|---|---|
| Impurity | Concentration |
| Oxygen | < 2.0 wt% |
| Carbon | < 0.2 wt% |
| Chlorine | < 100 ppm |
| Iron | < 100 ppm |
| Aluminum | < 50 ppm |
| Calcium | < 50 ppm |

**Table A – 1 – Impurity concentrations in the silicon nitride powder**

| Tokuyama E-Grade – AlN Powder | |
|---|---|
| Impurity | Concentration |
| Oxygen | 0.79~0.88 wt% |
| Carbon | 220~320 ppm |
| Calcium | 10~22 ppm |
| Silicon | 9~13 ppm |
| Iron | 2~9 ppm |

**Table A – 2 – Impurity concentrations in the aluminum nitride powder**

| Shin-Etsu – BB- Yttria Powder | |
|---|---|
| Impurity | Concentration |
| Calcia | < 10 ppm |
| Ceria | < 7 ppm |
| Erbia | < 5 ppm |
| Dysprosium Oxide | < 5 ppm |
| Neodymium Oxide | < 5 ppm |
| Iron Oxide | < 5 ppm |
| Ytterbium Oxide | < 5 ppm |

**Table A – 3 – Impurity concentrations in the yttria powder**

| Sumitomo AKP-50 – Alumina Powder | |
|---|---|
| Impurity | Concentration |
| Silicon | ≤ 50 ppm |
| Iron | ≤ 30 ppm |
| Sodium | ≤ 10 ppm |
| Magnesium | ≤ 10 ppm |
| Copper | ≤ 10 ppm |

**Table A – 4 – Impurity concentrations in the alumina powder**

| Evonik Industries – Aerosil 200 – Fumed Silica Powder | |
|---|---|
| Impurity | Concentration |
| Antimony | < 1 ppm |
| Arsenic | < 1 ppm |
| Barium | < 1 ppm |
| Cadmium | < 1 ppm |
| Lead | < 1 ppm |
| Mercury | < 1 ppm |
| Nickel | < 1 ppm |
| Selenium | < 1 ppm |
| Zinc | < 1 ppm |

**Table A – 5 – Impurity concentrations in the fumed silica powder**

| Lower Friction MK-hBN-N70 | |
|---|---|
| Soluble Boron Oxide | < 0.15 wt% |
| Free Carbon | 0 wt% |
| Oxygen | 0.11 wt% |
| Calcia | 0.036 wt% |
| Alumina | 0.04 wt% |
| Iron Oxide | 0.24 wt% |
| Titania | 0.008 wt% |
| Magnesia | 0.04 wt% |
| Sodium Oxide | 0.005 wt% |

**Table A – 6 – Impurity concentrations in the boron nitride powder**